UNIVERSITY OF LATVIA

Līga Grīnberga

RESEARCH OF NEW COMPOSITE MATERIALS FOR HYDROGEN STORAGE

Doctoral thesis

Department of Physics
Subsection of Material Science

RIGA 2007

1. Literature overview

1.1 Introduction

In 1870 Jules Verne proposed in his novel “L’île mystérieuse”: “I believe that water will one day be employed as fuel, that hydrogen and oxygen which constitute it, used singly or together, will furnish an inexhaustible source of heat and light, of an intensity of which coal is not capable. I believe then that when the deposits of coal are exhausted, we shall heat and warm ourselves with water. Water will be the coal of the future” [1].

According to the Olduvai theory [2] the life expectancy of an Industrial Civilization is about one hundred years, measured by the world average energy production on the person per year: ê = E/(Pop). The Industrial Civilization defined in this theory began in 1930 and is predicted to end on or before the year 2030. Following the estimations and explorations in 5 continents and 30 countries, there is no doubt that the peak and decline of the Industrial Civilization should occur. Many factors could its decline, namely: overpopulation, depletion of non-renewable resources, and damage to the environmental, pollution, soil erosion, global warming, newly emerging viruses, and conflicts for scarce resources. Figure 1.1.1 depicts the Olduvai theory.

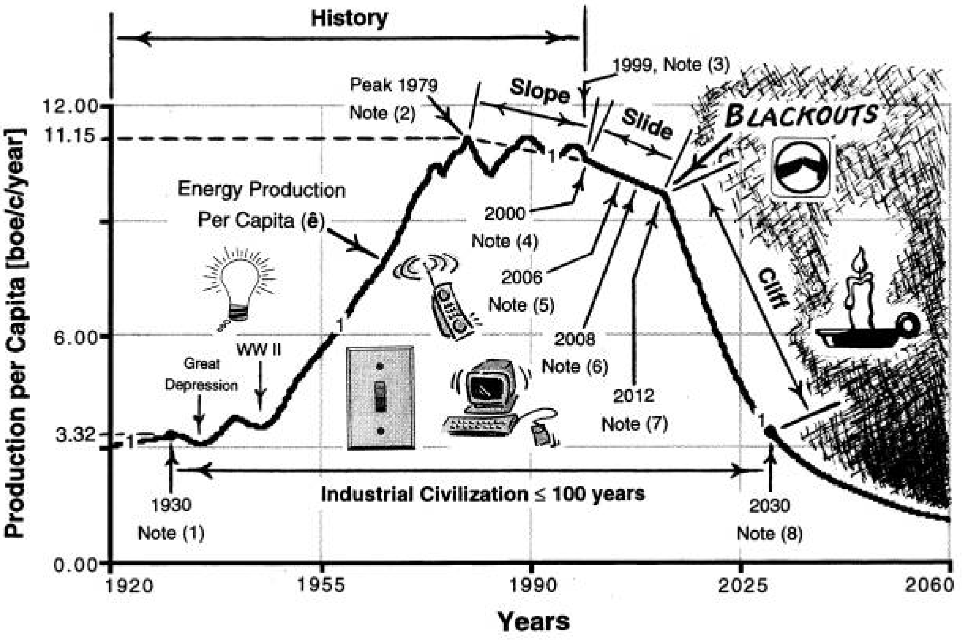

Figure 1.1.1: The Olduvai Theory: 1930-2030

Notes: (1) 1930 => The Industrial Civilization began when (ê) reached 30% of its peak value. (2) 1979 => ê reached its peak value of 11.15 boe/c. (barrels of oil equivalent per capita). (3) 1999 => Oil is no longer an inexpensive resource. (4) 2000 => Beginning of the "Jerusalem Jihad": violence erupts in the Middle East. (5) 2006 => Predicted peak of world oil production. (6) 2008 => OPEC will reach a crossover event. (7) 2012 => The world will plunge in a permanent blackout. (8) 2030 => The Industrial Civilization ends when ê falls to its 1930 value. (9) We can observe three distinct intervals of decline in the Olduvai schema (slope, slide and cliff): each one is steeper than the previous. (10) The small cartoon stresses that electricity is the essential *end-use* energy for the Industrial Civilization.

The British Petroleum statistical review of World energy 2005 pointed that prices for crude oil, natural gas and coal have reached record (nominal) levels in 2005. World primary energy consumption increased by 2.7% in 2005, below the previous year’s strong growth of 4.4% but is still above the 10-year average. The strongest increase was in the Asia Pacific region, which rose by 5.8%, while North America continues to register a slow growth, at 0.3%. Consumption in the USA felt slightly, while China accounted for more than half of global energy consumption growth. The Brent dated oil price averaged $54.52 per barrel in 2005, more than 40% above the 2004 average. Prices reached a daily peak of more than $67 in mid-August. Global oil consumption grew by 1.3% in 2005, below the 10-year average and a marked slowdown from the strong growth (+3.6%) seen in 2004. Global consumption rose by 1 million barrels per day (mb/d), reaching 82.5 mb/d. Chinese consumption, which grew by nearly 1 million b/d in 2004, rose by only 200’000 b/d. US consumption declined by 75’000 b/d.

Producers from the OPEC consortium increased their market share; they accounted for nearly all the net increase in global production, as their output rose by 900’000 b/d. Saudi Arabia utilized both existing and newly installed production capacity to increase output to 11 million b/d. Kuwait and Qatar each increased output by at least 100’000 b/d. Iraqi production declined by nearly 200’000 b/d. Oil production outside OPEC remain stable, the weakest performance since 1993. Output from the OECD decreased by 950’000 b/d, the largest contraction ever recorded. Output in the USA dropped by 400’000 b/d, with much of the decline owing to damage sustained by oil refineries from hurricanes. Output from both the UK and Norway felt by more than 200’000 b/d. These declines were offset by rising non-OECD production. Russian production increased again, but at a reduced rate. Output grew by 260’000 b/d, one-third of the growth seen in 2004. New deepwater production pushed Angolan output up by more than 250’000 b/d. Azerbaijan, Brazil and China each increased production by at least 100’000 b/d[3].

World natural gas consumption grew by 2.3% in 2005, more slowly than in 2004 but close to the 10-year average. North America was the only region to see consumption decline. In the USA, the world’s largest consumer, gas use declined by 1.5%, also gas use in the UK declined by 2.2%. Elsewhere, gas consumption rose by 3.8%, with the largest gains in China, southern Europe and India. China’s production increase was the largest in the world.

Coal was again the world’s fastest-growing fuel, with global consumption rising by 5% or twice the 10-year average. Consumption in China, the world’s largest consumer, rose by 11%. China accounted for 80% of global growth. Consumption growth in the USA was also above average, while growth in the rest of the world was close to the 10-year average. Nuclear power consumption stagnated in 2005, rising by 0.6%, below the 10-year average of 1.8%. Global hydroelectric generation rose by 4.2%, the second consecutive above-average year. Growth was boosted by new capacity in China, where output rose by 13.7%. Elsewhere, growth in northern Europe, Brazil and Canada offset declines owing to low rainfall across southern Europe and parts of the USA.

Figure 1.1.2 shows the World consumption of primary energy measured in the tonnes of oil equivalent. Consumption growth slowed but still exceeds the 10-year average. Asia accounted for nearly ¾ of global growth, where China takes more than half. In the past decade, natural gas and coal have increased their shares of the total at the expense of oil, nuclear energy and hydroelectricity. Further, in figure 1.1.3, is displayed the fossil fuel world's reserves to production ratio for oil, gas and coal. The world's R/P ratio for coal in 2005 was nearly four times that for oil and 2.5 times that for gas. Regionally, coal was even more dominant from the OECD and Former Soviet Union countries, while gas reserves were more abundant relative to production elsewhere.

Figure 1.1.4 shows the consumption of tonnes of oil equivalent per capita. We observe that the USA, Canada, Iceland, Norway and Saudi Arabia are the largest consumers of energy. In contrast, the largest reserves are situated in the Middle East and Russia.

Analyzing these data and tracing tendencies, it is clear that the primary energy consumption is increasing but reserves are running out very rapidly. Meanwhile, global utilization of fossils is causing environmental problems throughout the world. Concerns about climate change and energy security are included in the policies and agreements between the developed countries. One of the first international greenhouse gas emission reductions is the Kyoto Protocol[4]. Considering this information, it is clear that the world requires new energy sources and carrier of energy that could satisfy the requirements of the world's energy demand. At the same time, these new sources and carriers should be environmentally friendly, economically feasible and accessible for every nation.

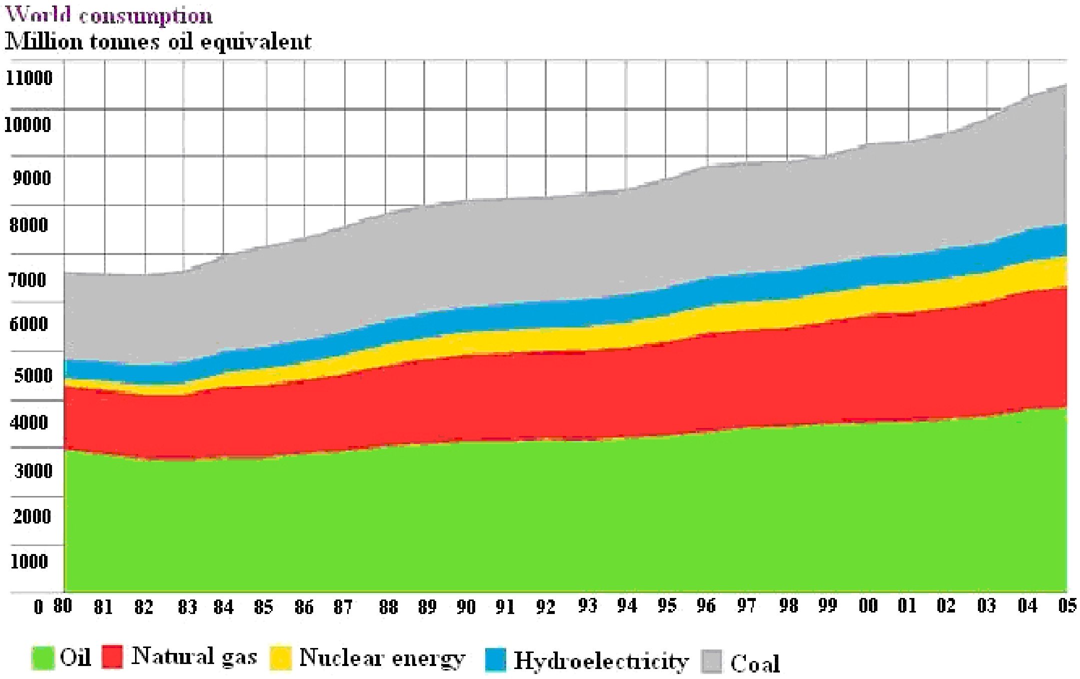

Figure 1.1.2: World consumption of global primary energy

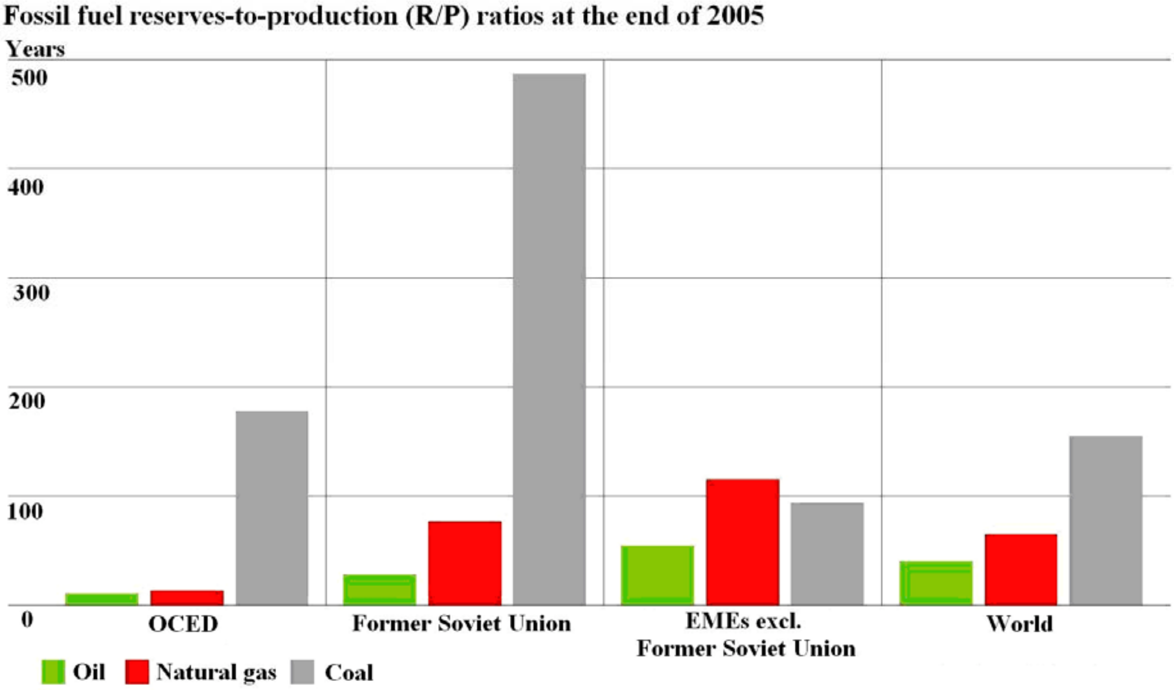

Figure 1.1.3: The world's reserves to production ratio of fossil fuels

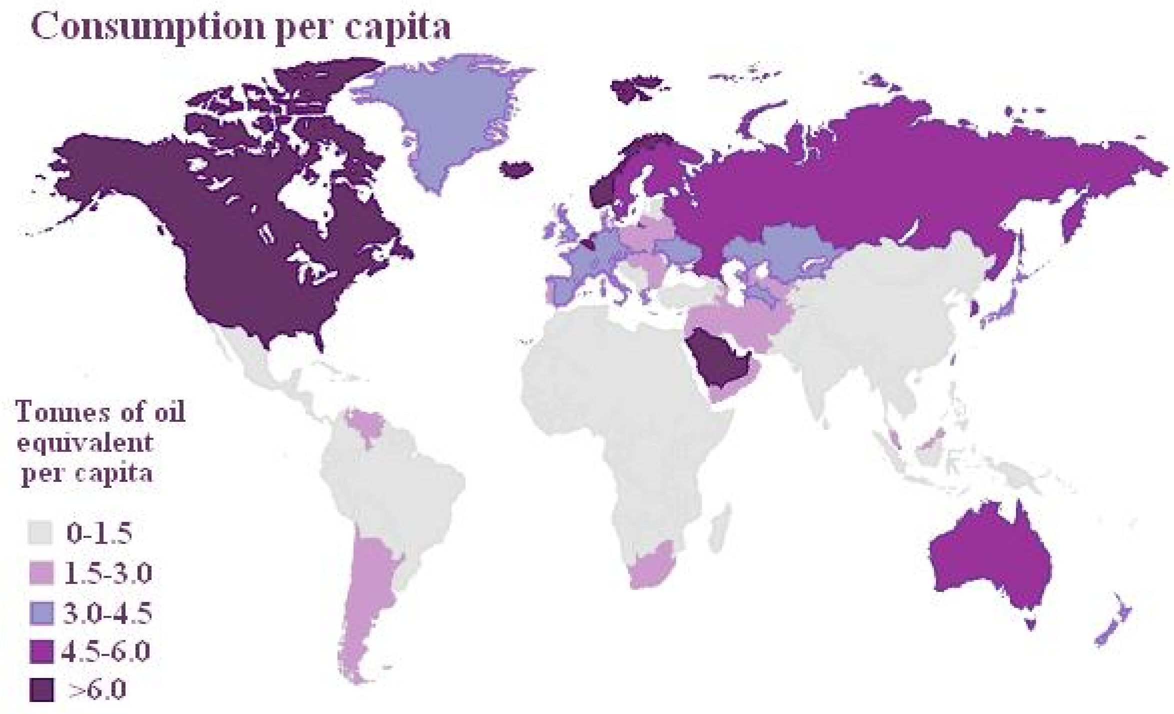

Figure 1.1.4: Consumption per capita of primary energy.

As a consequence, investigations of alternative energy strategies have recently become important, particularly for future world stability. The most important property of alternative energy sources is their environmental compatibility.

One such new energy carrier currently being investigated is hydrogen. Many hold the hopes that it could maintain mankind's growing need for energy. However, the hydrogen alternative holds both positive and negative aspects. The main advantage of hydrogen as a fuel is sustainable development. Generation of CO_2 and other pollutants is low if low temperature fuel cells are employed: however, it is a problem for high temperature fuel cells. Low temperature fuel cells are needed, however, if they are to be of use by the transport sector. It is a non-toxic energy carrier and holds a higher energy content: 9.5 kg of hydrogen is equivalent to that of 25 kg of gasoline [5]. Hydrogen can be produced in many ways, for example: electrolysis of water, direct and indirect thermochemical decomposition, and processes driven directly by sunlight. Compared to electricity, hydrogen can be stored over a relatively long time. Properly utilized, hydrogen can be employed in all parts of the economy such as a direct electricity supplier via a fuel cell, fuel for the automobile industry, and as fuel for heating systems, to name a few.

The drawbacks of hydrogen are: safety, pollution and storage. Hydrogen can burn in lower concentrations when mixed with air. It may produce pollutant gases if hydrogen is employed with a high temperature fuel cell. Storage is an important subject of research because it is not very efficient at this moment. Liquid storage requires very low temperatures and gaseous storage does not satisfy volumetric requirements. For solid hydrogen storage, the volume percents of absorbed hydrogen are too low compared with its total mass, the absorption/desorption rates are too slow and cycle life is too short. In addition, it is ironic to observe that hydrogen is still being extracted from fossil fuels, such as steam reforming of natural gas (or other light hydrocarbons), gasification of coal and other heavy hydrocarbons. It is still currently cheaper and more efficient to do so! However, despite these drawbacks, hydrogen still holds the best solution for sustainable carrier of energy able to meet the world's growing hunger for energy. The attributes and properties of hydrogen, and a comparison of hydrogen with other fuels, are presented in Tables 1.1.1 and 1.1.2.

The above features of hydrogen suggest that it will be particularly advantageous as a transportation fuel because of its versatility, utilization efficiency factor and relative safety. The only direct waste from hydrogen is its oxidation, thus producing water. It means that the only pollutants produced in an engine powered by hydrogen are the lubricants necessary to maintain the machine in proper order.

Table 1.1.1: Properties of hydrogen as a fuel

Property	Unit	Value
Density[a]	kg/m3	0.0838
HHV and LHV	MJ/kg (liquid)	141.9–119.90
HHV and LHV	MJ/m3 volumetric)	11.89–10.05
Boiling point	K	20.41
Freezing point	K	13.97
Density (liquid)	kg/m3	70.8
Diffusion coefficient in air[a]	cm 2/s	0.61
Specific heat at constant pressure	kJ/kg K	14.89
Ignition limits in air	% (volume)	4–75
Ignition energy in air	millijoule	0.02
Ignition temperature	K	585
Flame temperature in air	K	2318
Explosion energy	kJ/g TNT	58.823
Flame emissivity	%	17–25
Stoichiometric mixture in air	%	29.53
Stoichiometric air/fuel	kg/kg	34.3/1
Flame velocity	cm/s	2.75
Motivity factor	–	1.00

It is envision that a slow transition from an economy relying on fossil fuel to one on hydrogen should prevail. Many decades should be necessary in order to implement all the changes required for such a radial transition. A reasonable way to expand the role of hydrogen in the near term is to start it step by step [6, 7]. For example, transport sectors could use hydrogen mixed with natural gas as a fuel for internal combustion engines. Another approach involves producing hydrogen at central locations and distributing it to refuelling stations. During this conversion phase, hydrogen is still mainly produced by steam reforming of natural gas. In many ways, hydrogen extracted from natural gas, using currently available technologies, release a higher energy per mass compared to simply burning natural gas. Moreover, greenhouse gas emission to the atmosphere can also be reduced either: by employing established ways of collecting of the high-purity carbon dioxide or by sequestration of it.

Table 1.1.2: Comparison of key properties for hydrogen and other fuels

Fuel type	Energy per unit mass (J/kg)	Energy per unit volume (J/m3)	Motivity factor	Specific carbon emission (kg C/kg fuel)
Liquid hydrogen	141.90	10.10	1.00	0.00
Gaseous hydrogen	141.90	0.013	1.00	0.00
Fuel oil	45.50	38.65	0.78	0.84
Gasoline	47.40	34.85	0.76	0.86
Jet fuel	46.50	35.30	0.75	–
LPG	48.80	24.40	0.62	–
LNG	50.00	23.00	0.61	–
Methanol	22.30	18.10	0.23	0.50
Ethanol	29.90	23.60	0.37	0.50
Bio diesel	37.00	33.00	–	0.50
Natural gas	50.00	0.04	0.75	0.46
Charcoal	30.00	–	–	0.50

Activities in the intermediate term should focus on restructuring the electric utility industry. Hydrogen-powered fuel cells would provide on-site generation of electricity. Additionally these fuel cells might also produce thermal energy for hot water, space heating, and other industrial processes. Hydrogen would be mainly produced by coal. Pyrolysis or gasification of biomass from dedicated crops, agricultural residues and municipal solid wastes, would also provide the necessary hydrogen. During this phase an hydrogen infrastructure, built along dedicated transportation routes, would be implemented as a result of an increase number of hydrogen-fuelled zero-emission vehicles.

In the longer term, hydrogen markets will have reached maturity and the hydrogen production and distribution infrastructures will be firmly in place. This in turn will create opportunities to implement new form of hydrogen generation from renewable systems such as wind turbines or photovoltaic energy. The fuel cells will use the hydrogen to provide electricity during higher demand periods or to supplement the intermittent energy sources. In this time an advanced technologies that produce hydrogen from water and sunlight and that store hydrogen in high-energy-density systems will be necessary. Market penetration of advanced technologies to produce, store and use hydrogen will mark the establishment of the hydrogen energy economy.

The first steps must be done immediately if we are to proceed to the successful transfer to a hydrogen energy systems and economy. The developed countries are working on the researches, investigations and calculations about the possible ways and opportunities to make a more smooth way to the new energy, to use the most appropriate materials, renewable energy sources for certain regions and nations.

The European Commission has developed several strategies, policies and new proposals to combat climate change and to increase the share of renewable in the energy and transport sectors [8-11]. It has also sponsored the project “HySociety - the European hydrogen-based Society”. The main aim of the project is to support the introduction of a safe and dependable hydrogen-based society in Europe by providing an action plan that integrates political, technological, economic, social and environmental issues. The programme is meant for the public to introduce and to explain opportunities and progress towards establishing a clean, safe and efficient hydrogen-based society in Europe. It speaks about barriers such as standards for infrastructure implementation and public safety concerns, the social and economic impacts, changing trends in industrial structures and in the European economy [12].

In the United States, the “Strategic Plan for Hydrogen Program” already started in 1979, aims at promoting hydrogen as a cost-effective energy carrier for utilities, buildings and transportation. The US Department of Energy presented in 2002 two documents, the Hydrogen Vision and Roadmap, in which it is described where and how the transition from traditional fossil energy to hydrogen will be realized by the year of 2030 [13, 14].

Overall, the USA and Japan have taken a leading role in fuel cell research with large investments. For example, in the USA the FreedomCAR project is to advance high-technology research needed to produce practical, affordable hydrogen fuel cell vehicles. It is bonded with the new FreedomFUEL initiative that stands for the development of the technologies and infrastructure needed to produce, store and distribute hydrogen for use in fuel cell vehicles and electricity generation. The combined cost of the two programmes is $1.7 billion over the 5 years [15].

In Japan, the WE-NET project has allocated about $11 billion for a 28-year period running in three stages up to the year 2020. The main objective of the program is to develop basic technologies for achieving a hydrogen-based energy economy [16].

The international program of Euro-Quebec Hydro-Hydrogen Pilot Project is a very successful program for hydrogen energy development in the world, and many countries carry out similar projects to improve the capacities of hydrogen application [17].

A survey of European projects on hydrogen reveals that there were about 336 individual research, development and demonstration activities in hydrogen between 1988 and 1999 [18]. Nonetheless, research on hydrogen in the European Union is still fragmented and is far behind the programs of the US and Japan. Overall funding for hydrogen fuel cell research in the EU is showed in the Figure 1.1.5.

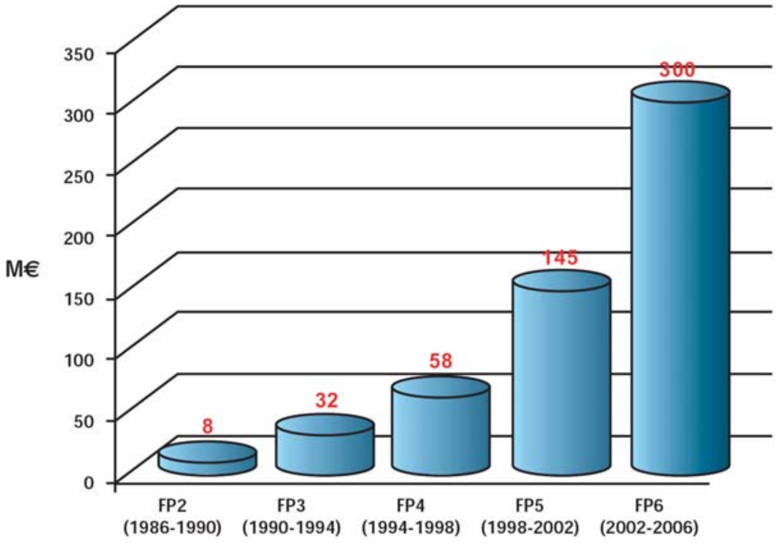

Figure 1.1.5: European Union funding for Hydrogen and Fuel Cell projects [19].

Despite unequal funding or opportunities, countries have to work together to prevent an upcoming ecological energy crisis.

1.2 Hydrogen production

Hydrogen production is the first step toward the transition to a hydrogen economy. Fossil fuel systems for hydrogen production are the oldest technologies and tend to be the cheapest. Because fossil fuels are carbon-based, carbon dioxide is produced as a by-product when they are decomposed to release energy. Biomass pyrolysis and gasification processes are very similar to fossil fuel reforming and gasification processes.

The water splitting methods can use nuclear heat or alternative energy sources do not produce harmful emissions but they are more expensive than fossil fuel processes. Photocatalytic and photobiological processes use solar energy, and the sulphur iodine process uses nuclear heat. In the case of electrolysis, electricity supplies the energy required and there could be used alternative energy sources like wind, solar, or water power. These processes are attractive because the water feedstock contains only hydrogen and oxygen, so no carbon dioxide is released in its decomposition [20].

1.2.1 Hydrogen from fossil fuels and alternative sources

1.2.1.1 Steam Methane Reforming

Steam reforming converts methane into hydrogen and carbon monoxide. The goal of the reformer is to remove as much of the hydrogen as possible from this molecule, while minimizing the emission of pollutants such as carbon monoxide.

Steam methane reforming is a three steps process to produce hydrogen (fig. 1.2.1.1.1). Methane is first catalytically reformed by reaction with steam over a nickel catalyst to produce a synthesis gas mixture of H_2, CO, CO_2, and other impurities at temperatures between 500°C and 950°C and a pressure around 30 atmospheres.

In the second step, known as a water gas shift reaction, the carbon monoxide produced in the first reaction is reacted with steam over a catalyst to form hydrogen and carbon dioxide.

The third step includes product purification that is typically achieved by pressure swing adsorption to remove water, methane, CO_2, N_2, and CO, producing very pure hydrogen product. Alternatively, chemical absorption of H2 may be achieved using an amine contactor, followed by methanation to eliminate CO and CO_2 impurities.

The steam reforming reactions are [21]:

$$CH_4 + H_2O \rightarrow 3\,H_2 + CO;\ \ -206\ kJ/mol$$
$$CH_4 + 2H_2O \rightarrow 4\,H_2 + CO_2;\ \ -165\ kJ/mol,$$

or in general:

$$C_nH_m + nH_2O \rightarrow (1/2m+n)H_2 + nCO.$$

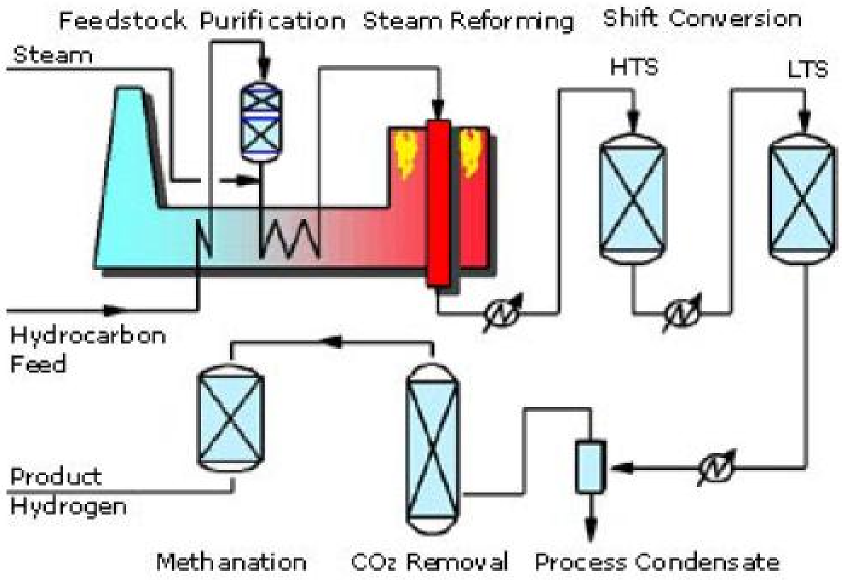

Figure 1.2.1.1.1: Steam methane reformation process[22].

1.2.1.2 Partial oxidation and autothermal reforming

Partial oxidation converts methane and other liquid hydrocarbons by direct oxidizing in a one-step reaction where steam reforming is not applicable and produces a synthesis gas mixture of CO and H_2:

$CH_4 + 1/2O_2 \rightarrow 2H_2 + CO$; -36 kJ/mol,

or for hydrocarbons in general:

$C_nH_m + 1/2nO_2 \rightarrow 1/2mH_2 + nCO$;

The partial oxidation works at temperatures between 1100 and 1500 °C in the pressure range 2-6 MPa [23].

In order to achieve an effective reforming reaction, it is essential that the required heat is available throughout the reaction. The best way to achieve this result is to generate the heat in the same location as it is needed. The bi-functional monolith auto-thermal reforming catalyst is able to generate the heat required to complete the reforming reaction in the same reactor space where that reforming reaction takes place (fig. 1.2.1.2.1). This allows for operation with lower peak process temperatures and avoids equipment designed for complex heat transfer.

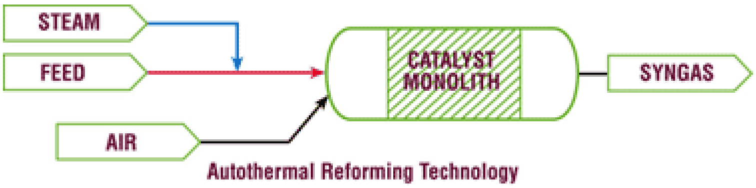

Figure 1.2.1.2.1: The scheme of auto-thermal steam reforming [24]

1.2.1.3 Coal gasification

Like steam methane reforming, coal gasification involves three steps: treatment of coal feedstock with high temperature steam (1330°C) to produce synthesis gas, a catalytic shift conversion, and purification of the hydrogen product (fig.1.2.1.3.1). The reaction in the first step could be written as follows:

Coal (carbon source) + $H_2O \rightarrow H_2 + CO$ + impurities

In the second step, the synthesis gas passes through a shift reactor converting a portion of the carbon monoxide to carbon dioxide, as shown in the reaction below:

$$CO + H_2O \rightarrow CO_2 + H_2$$

The synthesis gas entering this reactor is pre-treated by passing through a quench cooler where it is saturated with water. The shift reactor is adiabatic, operates at a temperature of ~450 °C, and contains a sulphur tolerant cobalt molybdate shift catalyst. The shifted synthesis gas contains 60 volume % hydrogen mixed with primarily CO_2 and some residual carbon monoxide. The mixture is cooled and enters a lower temperature shift reactor, after which it is cooled again.

In the third step, the hydrogen product is purified where physical absorption removes 99% of H_2S impurities. The 85% of H_2 in the shifted synthesis gas is then removed as 99.999% pure H_2 in a pressure swing adsorption unit.

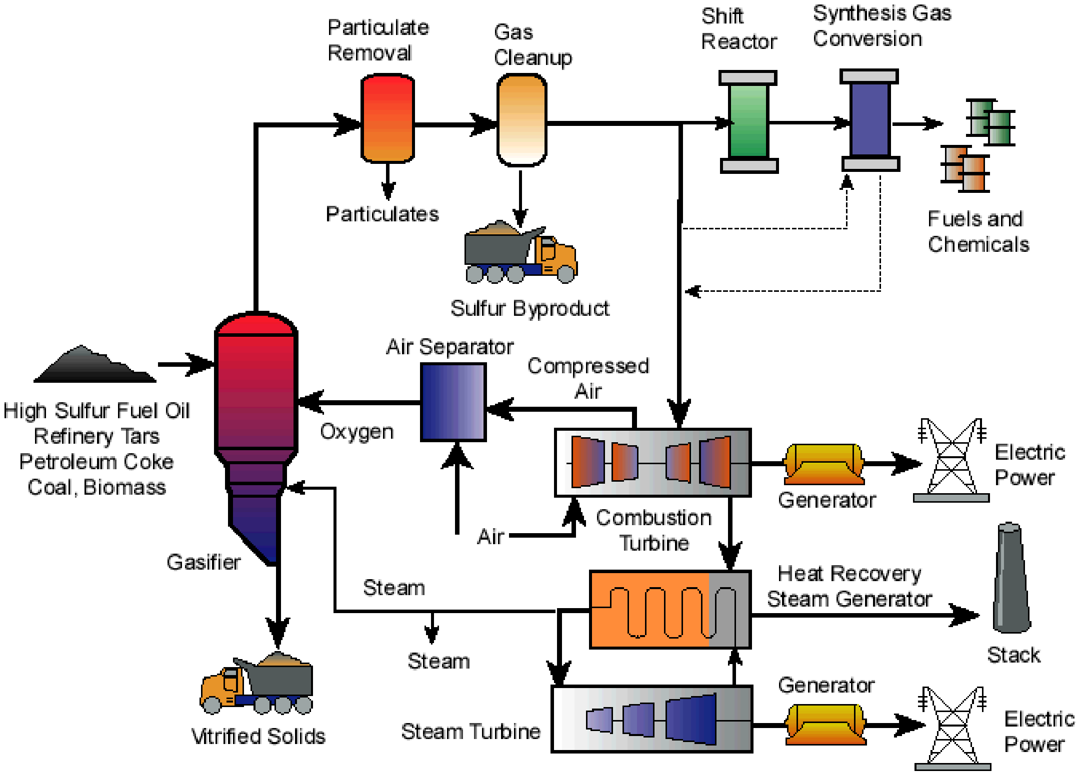

Figure 1.2.1.3.1: Coal (also – petroleum, waste, biomass) gasification system [25].

1.2.1.4 Biomass pyrolysis / gasification

Biomass may used to produce hydrogen in two ways: by a direct gasification process, or by pyrolysis to produce liquid bio-oil for reforming. Biomass refers to crops or other agricultural products, including hardwood, softwood, and other plant species. It may also include municipal solid waste or sewage, a fraction of which is burned to produce steam for the process.

The direct biomass gasification process is similar to the coal gasification process. First, the biomass is treated with high temperature steam in an oxygen-blown or air-blown gasifier to produce a synthesis gas mixture composed of hydrocarbon gases, hydrogen, CO, CO_2, tar, and water vapour. Carbon residue and ash are left behind. Then a portion of the carbon residue is gasified by reaction with oxygen, steam, and hydrogen, while another portion is combusted to provide heat.

As in the coal gasification process, the gasification step is followed by a shift reaction and purification.

The other way of treatment of the biomass is reforming to a liquid bio-oil in a pyrolysis process. Pyrolysis is an endothermic process for thermal decomposition of biomass carried out at 450-550°C. The produced bio-oil is a liquid composed of oxygenated organics and water. The bio-oil is steam reformed at 750 – 850 °C, followed by a shift reaction to convert CO to CO_2. The reactions could be written as[26]:

Biomass + Energy $\rightarrow$ Bio-oil + Carbon residue + Gas Impurities (pyrolysis)

Bio-oil + H2O$\rightarrow$ CO + H_2 (reforming)

CO + $H_2O \rightarrow CO_2 + H_2$ (shift reaction)

1.2.1.5 Photosynthetic and photo-biological production

A number of technologies for biological H_2 production are available, but they are not established for significant amount of hydrogen production yet. Methods for engineering and manufacturing these systems have not been fully evaluated.

In photosynthetic hydrogen production, hydrogen is produced by the reduction of H^+ ions in an aqueous solution to H_2. Photo-biological production of hydrogen consists on two steps: photosynthesis and hydrogen production catalysed by hydrogenases. The hydrogenase enzymes are found in certain types of green algae and catalyze the reduction of H^+ to H_2.

Photosynthesis: $2H_2O \rightarrow 4H^+ + 4e^- + O_2$
Hydrogen Production: $4H^+ + 4e^- \rightarrow 2H_2$

Figure 1.2.1.5.1 describes a coordinated photosynthetic electron transport and coupled phosphorylation during H_2 production. Photosynthetic electron transport delivers electrons upon photo-oxidation of water to the hydrogenase, leading to photophosphorylation and H_2 production. The oxygen generated by this process serves to drive the coordinate oxidative phosphorylation during mitochondrial respiration. Electrons for the latter are derived upon endogenous substrate catabolism, which yields reductant and CO_2. Release of molecular H_2 by the chloroplast enables the sustained operation of this coordinated photosynthesis-respiration function in green algae and permits the continuous generation of adenosine triphosphate by the two bioenergetic organelles in the cell.

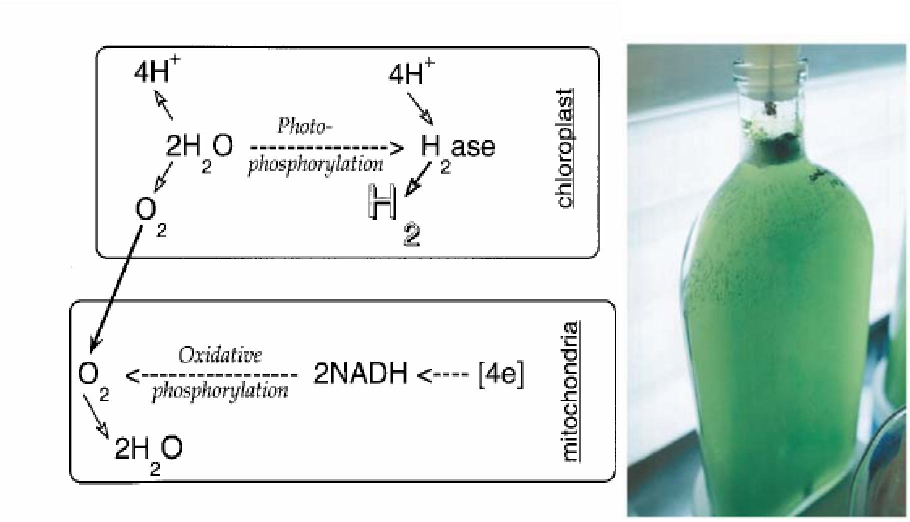

Figure 1.2.1.5.1: Photosynthetic electron transport and coupled phosphorylation during H_2 production and a hydrogen-producing *C. reinhardtii* culture in the bottle. Hydrogen bubbles emanate toward the surface of the liquid medium (28)

Growth of the algae under controlled conditions can stimulate the production of the hydrogenase enzyme for use in hydrogen production in, for example, green algae and cyanobacteria.

Anyhow, the processes still are not fully clear and it is crucial importance to understand the natural processes and the genetic regulations of H_2 production. The basic and applied research is needed but in case of success, a long-term solution for renewable hydrogen production will be reached. [27, 28]

1.2.2 Electrolysis

Hydrogen can be harshness by splitting a molecule of water: various approaches are feasible in that respect. Further are discussed several ways of hydrogen production by electrolysis: water, alkaline, PEM, high temperature electrolysis, photo-electrolysis and high-temperature water decomposition.

1.2.2.1 Water electrolysis

Water electrolysis is the process able to separate a water molecule into hydrogen and oxygen by supplying an electrical energy. An electrolysis cell consists of two electrodes, usually an inert metal, submerged in an electrolyte and connected to opposite electrical poles of a source of direct current. The electric current disassociates water molecule into hydroxide OH^- and hydrogen H^+ ions. In the electrolytic cell, at the cathode, hydrogen ions accept electrons in a reduction reaction that forms hydrogen gas:

Cathode: $2H_2O\ (l) + 2e^- \rightarrow H_2\ (g) + 2OH^-\ (aq)$

At the anode, hydroxide ions oxidize and give electrons to the anode to complete the circuit and form water and oxygen gas:

Anode: $2H_2O\ (l) \rightarrow O_2(g) + 4H^+\ (aq) + 4e^-$

The complete reaction is written as:

$2H_2O\ (l) \rightarrow 2H_2\ (g) + O_2\ (g)$ (1.2.2.1.1)

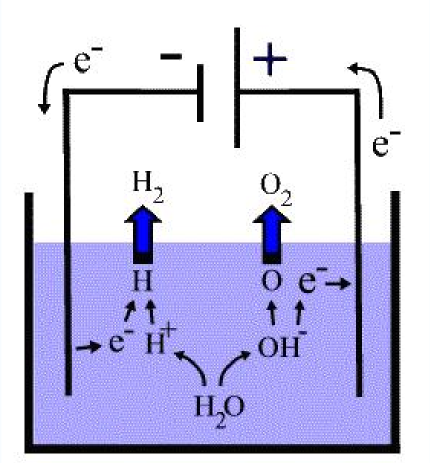

Figure 1.2.2.1.1: Electrochemical water splitting reactions.

From the thermodynamic data, the reversible decomposition potential (E_{rev}), measured at standard conditions, is equal to 1.228 V using the following relationship:

$$\Delta G = n \cdot F \cdot E_{rev}$$

Where the Gibb's free energy ΔG is lower than the change of enthalpy ΔH by certain amount of heat T·ΔS. Heat (Q = T·ΔS) must also be taken into account during electrolysis. If heat is supplied in the system in form of electrical energy, a thermal potential of 0.252 V (at standard conditions) must be added to the E_{rev} value:

$$E_q = \frac{T\Delta S}{n \cdot F}$$

The maximum decomposition potential that water molecule can yield is 1,480 V, at standard conditions. However, irreversible processes, occurring on the anode and cathode, and electrical resistance, within the cell, cause the actual decomposition potential of water, E_{act}, to be higher than 1.480 V (at standard conditions). Irreversible processes on the electrodes require the application of overpotentials. Reduction of these overpotentials can be achieved by placing suitable catalysts on the surfaces of electrodes. The electrical resistance value of the cell depends on numerous factors: the conductivity of the electrolyte, the ionic permeability of the diaphragm which separates anodic and cathodic regions, the distance of the anode from the cathode, and the current density used. Diaphragms are made from polymer, of polysulphone type, or ceramic material, such as barium titanate. In some applications, the electrodes are directly placed on the surface of the diaphragm. In this configuration, the distance between the electrodes can be reduced; also, it minimizes voltage drop and heat loss. The cathode material is usually made from steel. The over-voltage due to hydrogen evolution is lowered by coating the cathode material with a catalyst such as platinum black. The anode material is made from nickel and it is sometime coated with steel. The oxygen evolution over-voltage at the anode can be lowered by using lanthanum containing perowskites or nickel - cobalt oxides.

Kinetic inhibition, of the anodic and the cathodic processes and voltage drop, due to the electrical resistance of the cell itself, decrease the electrolysis efficiency. The efficiency of the electrolysis, η, is defined as:

$$\eta = \frac{E_{rev} + E_q}{E_{act}}$$

Typical cell voltages in conventional electrolysis plants vary between 1,85 to 2,05 V. This means that the efficiencies vary between 72 to 80 per cent. The current densities under typical operating condition are between 2 to 3 A/m^2. A typical water electrolysis unit consumes about 4 to 5 kWh of power to produce 1 m^3 of hydrogen.

Electrical energy required for water electrolysis decreases with an increase of temperature, although the total energy consumption is increasing [29, 30].

1.2.2.2 Alkaline electrolysis

Since water is a poor conductor, electrolyte made of aqueous KOH (NaOH) solution is preferred and usually circulates through the electrolytic cells. The following reactions take place inside the alkaline electrolysis cell:

Electrolyte: $4H_2O \rightarrow 4H^+ + 4OH^-$
Cathode: $4H^+ + 4e^- \rightarrow 2H_2$
Anode: $4OH^- \rightarrow O_2 + 2H_2O + 4e^-$
Total: $2H_2O \rightarrow O_2 + 2H_2$

Commercial electrolysers usually consist of a number of electrolytic cells arranged in a cell stack. Alkaline electrolysers typically contain the main components shown in Figure 1.2.2.2.1.

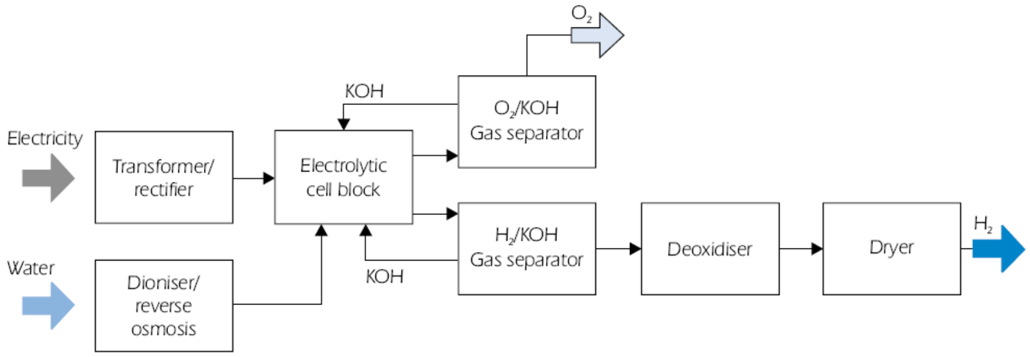

Figure 1.2.2.2.1: Process diagram of alkaline electrolysis

1.2.2.3 Polymer electrolyte membrane (PEM) electrolysis

PEM electrolysers require no liquid electrolyte; hence, the electrolyte is a thin film (with a thickness around 0.25 mm), consisting of a proton conducting ion exchange material such as Nafion. Electrical charge is transported by a hydrated hydrogen cation, of the sulphonic acid group of this polymer. The cathode is made from graphite and the anode is composed of sintered Ni or Ti. The catalysts are made of Pt metal and RuO_2, for the cathode and anode, respectively. The volume of the electrolysis unit is greatly reduced due to the absence of KOH electrolyte system. High current density values (up to 20 000 A/m^2) can be achieved in this configuration. The principle of the PEM electrolysis unit is exemplified in Figure 1.2.2.3.1 and in the following equations:

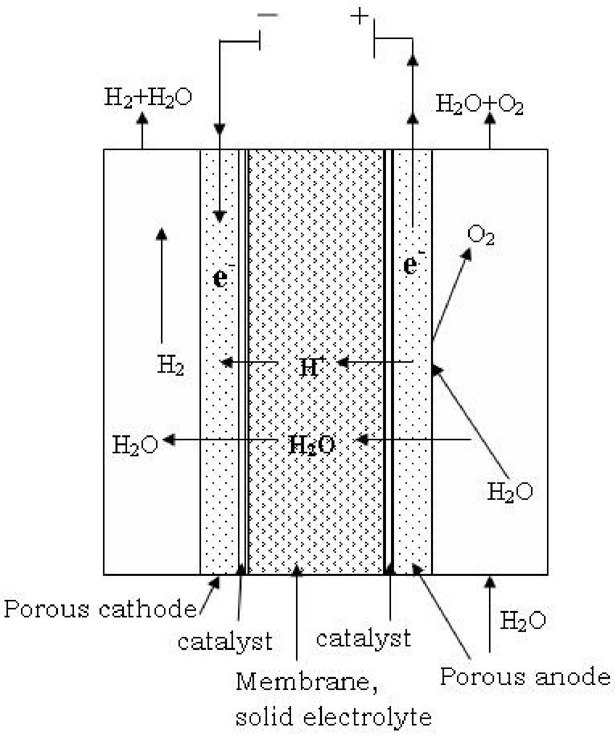

Figure 1.2.2.3.1: Electrolysis unit using proton exchange membrane [31]

anode: $2H_2O \rightarrow O_2 + 4\,H^+ + 4e^-$ (3.6)

cathode: $2H^+ + 2e^- \rightarrow H_2$ (3.7)

The limited lifetime of the polymer membrane is the main disadvantage of this technique [31, 32].

1.2.2.4 Photo-electrolysis

Photo-electrolysis of water is the process where light is used to split a water molecule into hydrogen and oxygen. Such systems offer great potential to reduce the cost of electrolytic hydrogen, compared with conventional two-step technologies.

The photo-electrochemical process is based on the band - gap absorption of photons by a semiconductor. Here, following absorption of a photon, exited electrons are elevated from the valence band to the conducting band, thus creating electron - hole pair in the semiconductor. Following this charge separation, oxidation of water molecules at the surface of the n -type semiconducting anode can take place:

$H_20(l) \rightarrow 1/2\ O_2\ (g) + 2H+(aq) + 2e^-$

The cathode of the photo-electrochemical cell is made of a metal onto which hydrated protons are transported. Transfer of electrons from the Fermi level of the metal causes the reduction of hydrated protons producing molecular hydrogen:

$2H+(aq) + 2e^- \rightarrow H_2(g)$

Achieving the splitting of a water molecule require a band gap energy from the semiconductor to be greater than the decomposition potential of water. In addition, the edge of the conduction band must be above the redox potential for the oxidation of water to occur.

Photovoltaic systems coupled to electrolyser offer some advantages, as the output can be in the form of: electricity from a photovoltaic cell or hydrogen from the electrolyser.

In figure 1.2.2.4.1 is showed two types of photo-electrochemical cells. A regenerative cell can convert light to electric power, leaving no net chemical change behind (Figure 1.2.2.4.1a). Negative charge carriers move through the bulk of the semiconductor toward the current collector and the external circuit. Positive holes are driven to the surface where they are taken away by the reduced form of the redox molecules. Conversion efficiencies up to 19.6% have been reported for multijunction regenerative cells[27].

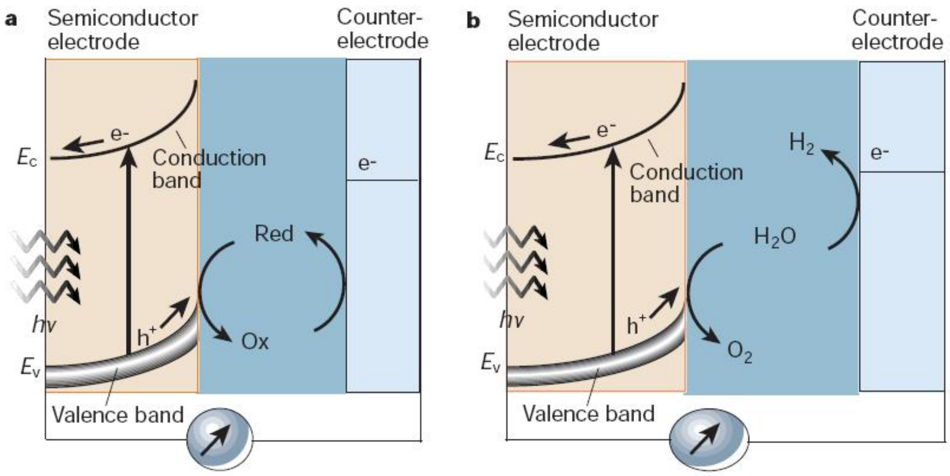

Figure 1.2.2.4.1: Principle of operation of photo-electrochemical cells based on n-type semiconductors. a, Regenerative-type cell producing electric current from sunlight; b, a cell that generates a chemical fuel, hydrogen, through the photo-cleavage of water [33]

The second type (fig 1.2.2.4.1b), is a photosynthetic cell. It operates on a similar principle except that there are two redox systems: one system reacts with the holes at the surface of the semiconductor electrode; the second reacts with the electrons entering the counter-electrode. In the example shown, a water molecule is oxidized to oxygen at the semiconductor photo-anode and reduced to hydrogen at the cathode. The overall reaction is the cleavage of water by sunlight.

Other concepts employ thin-film-on-glass devices immersed in water. They are based on the application of photosensitive powder catalysts suspended in water. However, these have lower light to hydrogen conversion efficiencies, amounting up to 16% [27].

1.2.2.5 High-temperature electrolysis and decomposition

In the case of high-temperature electrolysis, the electrical energy needed to split water at 1000 °C is considerably less than electrolysis at 25 °C. In turn, this translates into higher efficiencies, compared to low-temperature electrolysers.

Typical technology makes use of a solid oxide electrolyser cell (SOEC). This electrolyser is based on the solid oxide fuel cell (SOFC) that normally operates from 700 to 1000 °C. At these temperatures, the electrode reactions are more reversible, and the fuel cell reaction can more easily be reversed to an electrolysis reaction. Employing heat from geothermal, solar, natural gas, or even from wasted heat from other reactions, to drive the reaction would make this option economically more attractive.

The total energy requirement of water decomposition is almost temperature independent. The value of E_q increases with increasing temperature and E_{rev} that is supplied by electrical energy decreases with increasing temperature. Operating the cell at high temperatures has the additional advantage of decreasing the overvoltages on the electrodes. This results from the kinetic inhibition of hydrogen and oxygen evolution.

Lattice defect conductors, such as doped ZrO_2, are used as electrolyte in high temperature electrolysis cells. These materials become oxygen ion conductor at temperatures above 800°C. Thin membrane (~ 0,5 mm) made from these materials are used in a cell to reduce the electrical resistance. Porous electrodes are placed on the surface of this membrane. The cathode is made from ZrO_2. Ni is placed on the cathode as hydrogen evolution catalyst. Water vapour is fed to the cathode. The cell reactions are[30]:

$H_2O\ (g) + 2e^- \rightarrow O^{2-} + H_2(g)$	Cathode reaction
$O^{2-} \rightarrow 1/2\ O_2\ (g) + 2\ e^-$	Anode reaction
$H_20(g) \rightarrow H_2(g) + 1/2\ 0_2\ (g)$	Cell reaction

A voltage of about 1,3 V is applied between the electrodes and current densities of $4\ A\ /\ m^2$ are obtained in a typical water vapour electrolysers operating at 900°C. Operating principles of a high temperature electrolysis cell is illustrated in Figure 1.2.2.5.1.

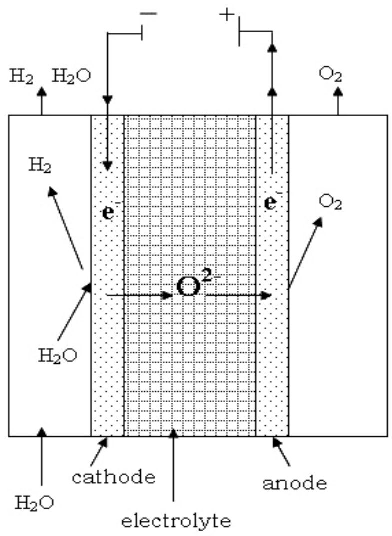

Figure 1.2.2.5.1: High temperature electrolysis cell using ZrO_2 solid electrolyte

A schematic of a nuclear hydrogen plant using high temperature electrolysis is shown in figure 1.2.2.5.2. The reactor (High Temperature Gas-cooled Reactor) supplies thermal energy to drive the power cycle and to heat steam for the electrolysis process. The high-temperature heat exchanger supplies superheated steam to the cells at a temperature of ~850°C, and a pressure of 5 MPa. The input gas contains both steam and hydrogen in order to maintain reducing conditions at the electrolytic cathode[34].

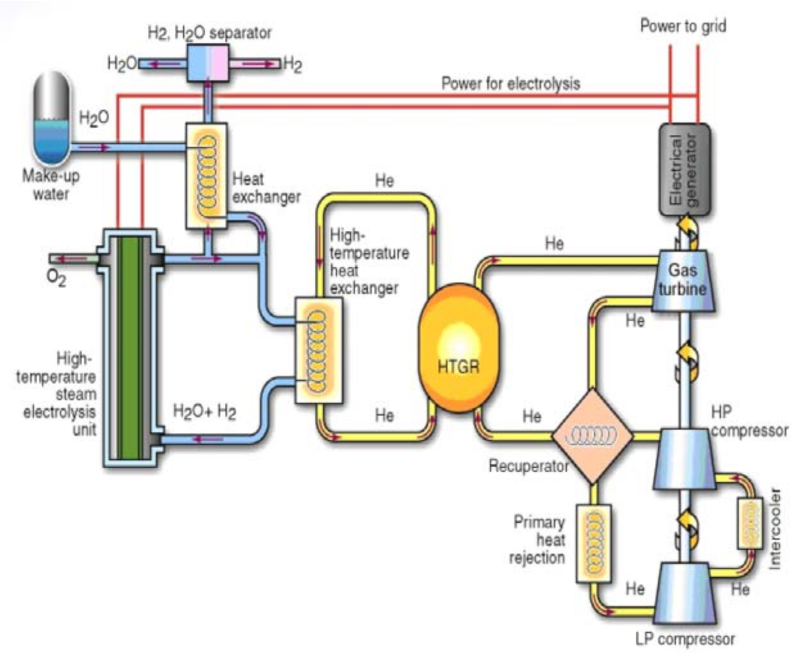

Figure 1.2.2.5.2: High Temperature Electrolysis system coupled with Gas-cooled Reactor[34]

High-temperature decomposition of a water molecule occurs at about 3000 °C. At this temperature, 10% of the water is decomposed and the remaining 90% can be recycled. For reduction of temperature other processes can be used, as thermo-chemical cycles, hybrid systems coupling thermal decomposition and electrolytic decomposition, direct catalytic decomposition of water with separation via a ceramic membrane and plasma-chemical decomposition of water in a double-stage CO_2 cycle. The efficiency is expected to be greater than 50% and evolving technologies and processes could lead to reduction of the cost of producing hydrogen.

The main development areas are: material development for corrosion resistance at high temperatures, high-temperature membrane and separation processes, heat exchangers, and heat storage media[32].

1.2.2.6 Thermo-chemical water splitting

Thermo-chemical water splitting is the conversion of a molecule of water into hydrogen and oxygen by a series of thermally driven chemical reactions. An example of a thermo-chemical process is the iodine/sulphur cycle Figure 1.2.2.6.1.

$2H_2SO_4 \rightarrow 2SO_2 + 2H_2O + O_2$

$I_2 + SO_2 + 2H_2O \rightarrow H_2SO_4 + 2HI$

$2HI \rightarrow I_2 + H_2$ at 459 °C

In total: $2H_2O \rightarrow 2H_2 + O_2$

The overall effect is to produce H_2 and O_2 with the addition of only water and heat to the cycle, without producing any harmful emissions or by-products. The I_2, SO_2, and H_2O react with an excess of molten iodine. The excess iodine results in a two phases product with a heavier HI and I_2 phase and lighter H_2SO_4 phase that can be separated by gravity. The sulphuric acid decomposition is achieved by concentration and vaporization of the acid followed by catalytic decomposition. The decomposition of HI is achieved using reactive distillation.

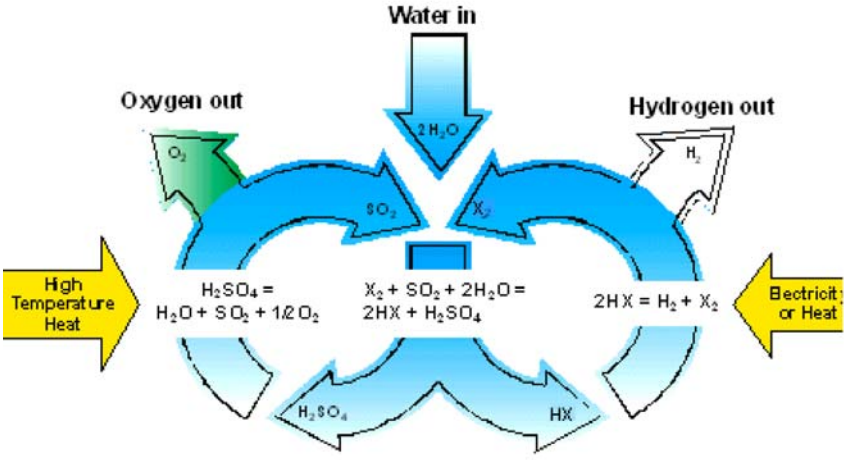

Figure 1.2.2.6.1: Schematic Diagram of Sulfur-Halogen Cycle (X= iodine or bromine)[35]

Nuclear reactors that may feasibly provide the temperatures necessary for this process are: heavy metal, molten salt, and prismatic or pebble-bed He-cooled reactors. Research is most developed for He-cooled reactors. As such, it is likely that this type of reactor will be the first to be coupled with the Sulphur-Iodine cycle.

Some problems will need to be addressed before going further with this approach. These are: corrosion and thermally split H_2 caption or sorption due to very active side reactions.

In table 1.2.2.6.1 the hydrogen production methods are summarized and the challenges and approaches of hydrogen production is showed in table 1.2.2.6.2 [32]

Table 1.2.2.6.1: Hydrogen production methods

Production Technique	**Energy Efficiency**	**Major Advantages**	**Major Disadvantages**
Steam Methane Reforming (SMR)	83%	- Proven technology - High efficiency - Economically viable - Large process, ideal for centralized production - Methane pipelines already in place	- Emission of CO_2 - Limited long-term methane supply - Vulnerable to methane feed price fluctuations - May not be easily scaled down for distributed production
Partial Oxidation of Methane	70-80 %	- Proven technology - Economically viable - May be scaled down for distributed production - Methane pipelines already in place	- Emission of CO_2 - Limited long-term methane supply - Vulnerable to methane feed price fluctuations - Lower efficiency than SMR - A catalysts for methane has not been developed
Autothermal Reforming of Methane	71-74%	- Proven technology - Lower reactor costs and simplified reactor design compared to SMR - Methane pipelines already in place	- Emission of CO_2 - Limited long-term methane supply - Vulnerable to methane feed price fluctuations - Lower efficiency than SMR
Coal Gasification	63%	- Proven technology - Economically viable - Large process, ideal for centralized production - Abundance of coal resources	- Emission of CO_2 - Vulnerable to coal feed price fluctuations - Less hydrogen-rich than methane – Lower efficiency in H_2 production
Direct Biomass Gasification	40-50% (Not proven in large scale process) 56% (for Fast Internal Circulation Fluidized Bed process)	- Renewable supply of raw material - Dose not dependent on fossil fuels - Emission of CO_2 considered environmentally neutral	- Varies in price range and yield due to varying hydrogen content of biomass source - Limited by rate at which biomass is available / renewable - Difficulties in transport of biomass may limit location / size of processes - Large scale process not proven

Table 1.2.2.6.1: Hydrogen production methods (cont.)

Production Technique	**Energy Efficiency**	**Major Advantages**	**Major Disadvantages**
Biomass Pyrolysis	56% (estimated for steam reforming of bio-oil after pyrolysis)	- Renewable supply of raw material - Dose not dependent on fossil fuels - Emission of CO2 considered environmentally neutral - Liquid bio-oil more easily transportable than bulk biomass for distributed production	- Varies in price range and yield due to varying hydrogen content of biomass source - Limited by rate at which biomass is available / renewable - Large scale process not proven
Electrolysis	25% 45-55% coupled with nuclear heat (Includes efficiency of electricity)	- Proven technology - Emissions free when paired with a renewable energy source - Small-scale ideal for distributed production	- Low overall efficiency - May indirectly contribute to CO2 emissions by electricity use - Highly dependent on electricity costs - PV and Wind based may not be reasonable for the required scale - Current capacities not large enough for a centralized production facility
SI Cycle	850 °C, 42% 950 °C, 52%	- Does not emit CO2 - Dose not dependent on fossil fuels - Large-scale processes ideal for centralized production; could be developed	- Difficult separations with lack of sufficient phase data - Highly corrosive conditions require qualification of new materials - High capital costs - Safety concerns – Heat input has to be provided by a nuclear reactor
Biosynthetic / Photo-biological	24% (speculative theoretical maximum)	- Renewable supply of raw material - CO2 by-product can be reused by bacteria in the system - Dose not dependent on fossil fuels	- Low efficiency - Capacity limited by depth of light penetration - High capital cost of bio-reactor
Photocatalytic Water Splitting	10-14% (24% theoretical maximum)	- Renewable supply of raw material - Does not emit CO2 - Dose not dependent on fossil fuels	- Difficult, costly catalyst synthesis - Low efficiency - Low production rates

Table 1.2.2.6.2: Challenges of hydrogen production and required approaches[32, 36]

Challenge	**Approach**
Cost reduction of distributed hydrogen production from natural gas and bio-derived liquids	• Improve reforming and separation efficiencies • Identify more durable reforming catalysts • Incorporate breakthrough separations technology • Reduce space taken by the raw supply • Optimize system operation • Intensify and consolidate the number of process steps, unit operations
Hydrogen production from water via electrolysis	• Reduce electricity costs of hydrogen production could be achieved by developing new materials • Reduce electricity costs of hydrogen production could be achieved by developing new systems to improve efficiency • Reduce capital costs of electrolysis system through new designs with lower cost materials
Hydrogen production from water via electrolysis	• Develop low-cost hydrogen production from electrolysis using wind or other renewable energy sources
Biomass Gasification	• Develop lower-cost reforming technologies
High-temperature, solar-driven thermochemical cycles for splitting water to produce hydrogen	• Utilize the high-temperature energy from concentrated solar power
Photoelectrochemical hydrogen production from water (direct water splitting)	• Develop high-efficiency PEC materials • Increase material's durability • Identify functional requirements and develop auxiliary device and systems materials • Develop photoelectrochemical devices and systems
Biological production of hydrogen	• Increase production efficiency of green algae, cyanobacteria, photosynthetic bacteria, and dark fermentative microorganisms • Develop biochemical and process methods to facilitate efficient production of hydrogen
Separation and purification systems (cross-cutting research)	• Develop separation technology for distributed and central hydrogen production

1.3 Hydrogen storage

Hydrogen storage is clearly one of the key challenges in developing hydrogen economy and hydrogen storage for vehicle applications is one of the most important challenges.

Hydrogen interaction with other elements depends from material, it occurs as anion (H-) or cation (H+) in ionic compounds, it participates with its electron to form covalent bonds, and it can even behave like a metal and form alloys at ambient temperature. The hydrogen molecule H_2 can be found in various forms depending on the temperature and the pressure which are shown in the phase diagram (fig. 1.3.1).

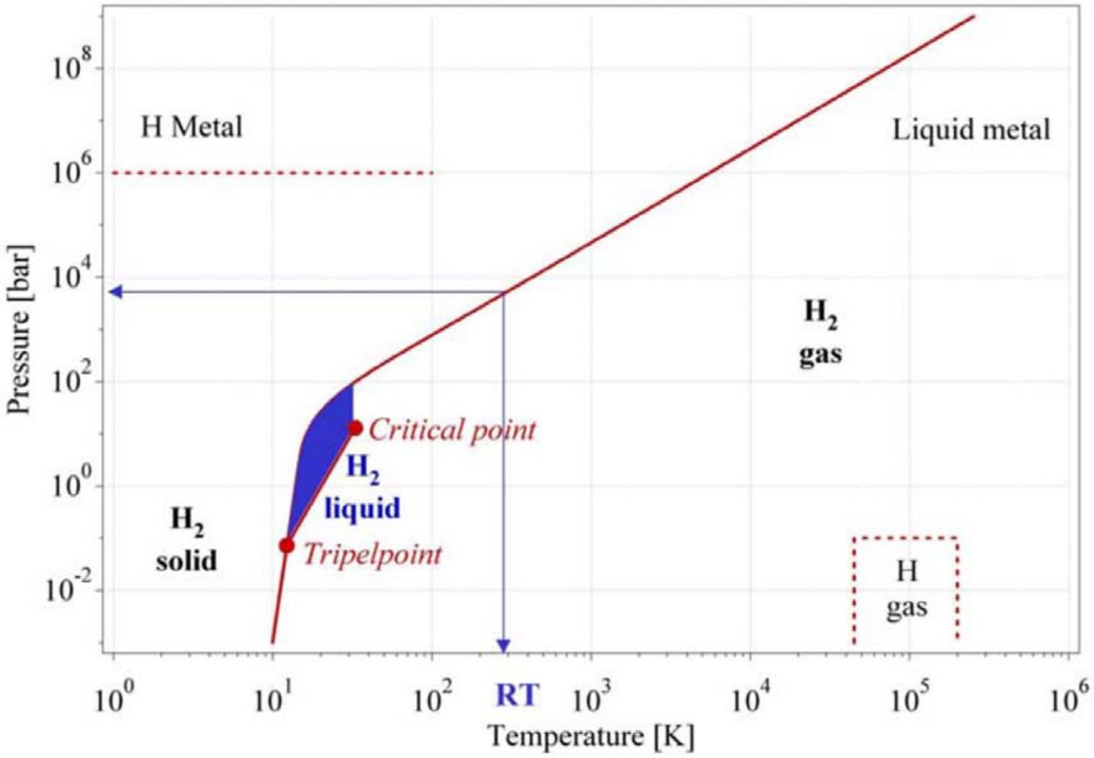

Figure 1.3.1: Primitive phase diagram for hydrogen (29)

The phase diagram shows that the liquid hydrogen with a density of 70.8 kg·m-3 at -253°C only exists between the solid line and the line from the triple point at 21.2K and the critical point at 32K. At low temperature hydrogen is a solid with a density of 70.6 kg·m-3 at -262°C and is a gas at higher temperatures with a density of 0.089886 kg·m^{-3} at 0°C and a pressure of 1 bar [37]

Hydrogen has very high gravimetric energy content, almost three times larger than petrol (fig. 1.3.2). However, the volumetric energy content is relatively low, due to the low density of the gaseous state (fig. 1.3.3). This means that, although the weight of the hydrogen necessary for a given process will be low relative to current energy storage systems, the volume required is larger.

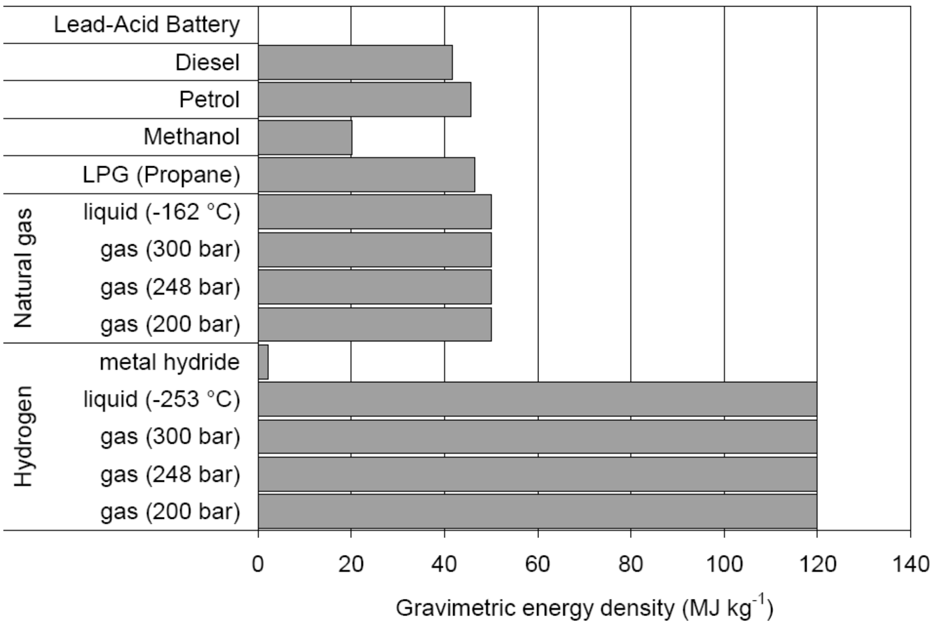

Figure 1.3.2: Gravimetric energy densities of hydrogen in comparison with other energy carriers [38]

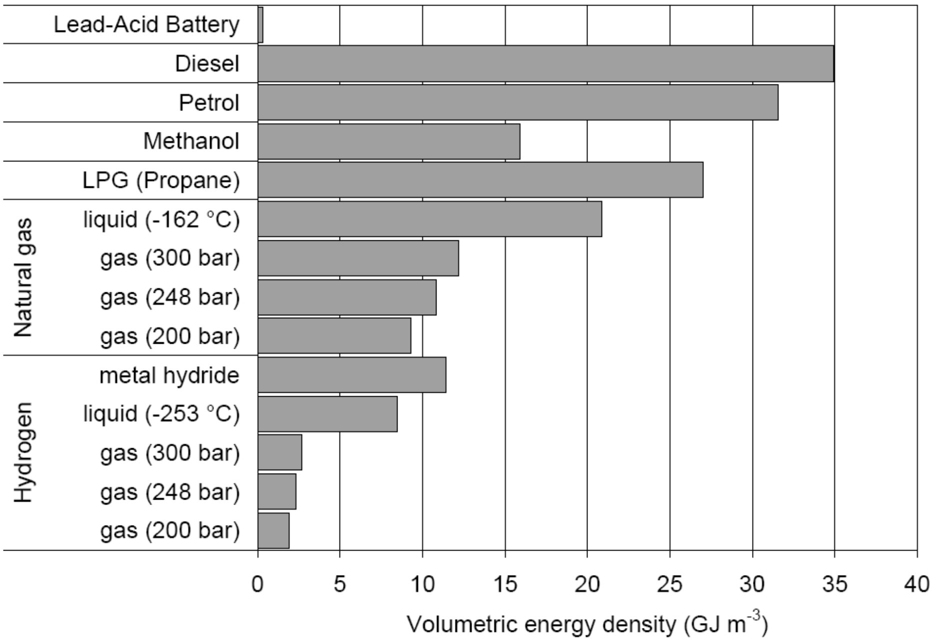

Figure 1.3.3: Volumetric energy densities of hydrogen in comparison with other energy carriers [38]

Hydrogen storage basically implies the reduction of the huge volume of the hydrogen gas because a 1kg of hydrogen at ambient temperature and atmospheric pressure takes a volume of 11 m^3. To increase a hydrogen density the compressing of hydrogen or decreasing of temperature below critical must be performed. In order to increase the hydrogen density in a storage system work must either be applied to compress hydrogen, or the temperature has to be decreased below the critical temperature or hydrogen have to be interacted with other material [38].

A very important factor for hydrogen storage system is the reversibility of the hydrogen uptake and release. This criterion excludes all covalent hydrogen carbon compounds as hydrogen storage materials due to the high temperatures for hydrogen releasing.

Available technologies permit directly to store hydrogen by modifying its physical state in gaseous or liquid form in pressurized or in cryogenic tanks. Storage by absorption as chemical compounds or by adsorption on carbon materials have definite advantages from the safety perspective such that some form of conversion or energy input is required to release the hydrogen for use. A great deal of effort has been made on new hydrogen-storage systems, including metal, chemical or complex hydrides and carbon nanostructures.

The US Department of Energy (DOE) published a long term vision for hydrogen-storage applications considering economic and environmental parameters. The predicted minimum hydrogen-storage capacity should be 6.5 wt% and 65 g/L hydrogen available, at the decomposition temperature between 60 and 120 ◦C for commercial viability. The 2015 targets represent what is required based on achieving similar performance to today’s gasoline vehicles (greater than 300 mile driving range) and complete market penetration across all light-duty vehicle platforms. These targets include a 20% penalty for the assumption that hydrogen storage systems (unlike conventional gasoline tanks) are not conformable and have limitations on how they may be packaged within a vehicle. The targets also assume a factor of 2.5–3 in terms of efficiency improvement in using a fuel cell power plant as compared to a conventional gasoline internal combustion engine. If efficiency improvements are not as high as projected, this would clearly dictate even more challenging requirements for on-board hydrogen storage to achieve comparable driving range (table 1.3.1) [32].

It is clear that there are advantages and disadvantages for the different options and no one of available hydrogen storage methods meets all the requirements.

The following chapters focus on the five common methods that can reversibly store hydrogen with a high volumetric and gravimetric density. There will be given a short description on these methods and illustrated their advantages and disadvantages.

Table 1.3.1: U.S. DOE technical targets for on-board hydrogen storage systems (32)

Storage parameter	Units	2007	2010	2015
System gravimetric capacity: usable, specific-energy from H2 (net useful energy/max system mass)	kWh/kg (kg H2/kg system)	1.5 (0.045)	2 (0.06)	3 (0.09)
System volumetric capacity: usable energy density from H2 (net useful energy/max system volume)	kWh/L (kg H2/L system)	1.2 (0.036))	1.5 (0.045	2.7 (0.081)
Storage system cost (and fuel cost)	$/kWh net ($/kg H2)	6 (200)	4 (133)	2 (67)
	$/gge at pump	–	2–3	2–3
Durability/operability				
Operating ambient temperature	°C	-20/50 (sun)	-30/50 (sun)	_40/60 (sun)
Minimum/maximum delivery temperature	°C	-30/85	-40/85	-40/85
Cycle life variation	% of mean (min) at % confidence	N/A	90/90	99/90
Cycle life (1/4 tank to full)	Cycles	500	1000	1500
Minimum delivery pressure from tank: FC = fuel cell, I = ICE	atm (abs)	8 FC/10 I	4 FC/ 35 I	3 FC/35 I
Maximum delivery pressure	atm (abs)	100	100	100
Charging/discharging rates				
System fill time (for 5 kg)	min	10	3	2.5
Minimum full flow rate	(g/s)/kW	0.02	0.02	0.02
Start time to full flow (20 °C)	s	15	5	5
Start time to full flow (-20 °C)	s	30	15	15
Transient response 10 – 90% and 90–0%	s	1.75	0.75	0.75
Fuel purity (H_2 from storage)	% H2	99.99 (dry basis)		
Environmental health and safety				
Permeation and leakage	scc/h	Meets or exceeds applicable standards		
Toxicity	–			
Safety	–			
Loss of useable H2	(g/h)/kg H2 stored	1	0.1	0.05

1.3.1 Compressed hydrogen gas

For more than 100 years hydrogen has been traditionally stored and transported in the gaseous phase in high-pressure vessels. In 1898, hydrogen was shipped for the first time in a steel cylinder with a capacity of 43 litres, holding the gas at a pressure of 140 bar.

The most common material used in hydrogen vessels is steel. Steel is quite cheap and hard-wearing but is also very heavy and thus diminishes the gravimetric energy density of the storage. Some vessels are made of aluminium that is lighter than steel but still hard-wearing. Steel cylinders can achieve a gravimetric density of approximately 1.1 wt% of hydrogen stored [39].

To run a compact car for 400 km, approximately 4 kg of hydrogen is required for a current fuel cell electric vehicle. To store 4 kg of hydrogen in the gaseous form at 200 bar, a traditional cylinder would have to have an internal volume of 220 litres, which is suitable for buses and lorries but impractical for a modern compact car.

General Motors HydroGen3 fuel cell vehicle (Opel Zafira minivan with a target curb weight of 1590 kg) is specified for a 270 km (168 mile) driving range with 3.1 kg of hydrogen at 700 bar. By increasing the amount of compressed hydrogen gas beyond 3 kg, a longer driving range can be achieved, but at more cost, weight and reduced passenger and cargo space on the vehicle [40].

Today, modern storage tanks can be made with carbon fibre composite materials, which are ultra light with a permeation resistant seamless liner and tough impact resistant reinforced shell. This makes them up to ten times stronger than steel, allowing them to store hydrogen at pressures in excess of 350 bar, which can be safely used for over 100,000 refill cycles and withstand surface temperatures over 800 °C. However, even at these pressures, to store a commercially acceptable amount of hydrogen the fuel tank required would still be too large in volume for a compact fuel cell car.

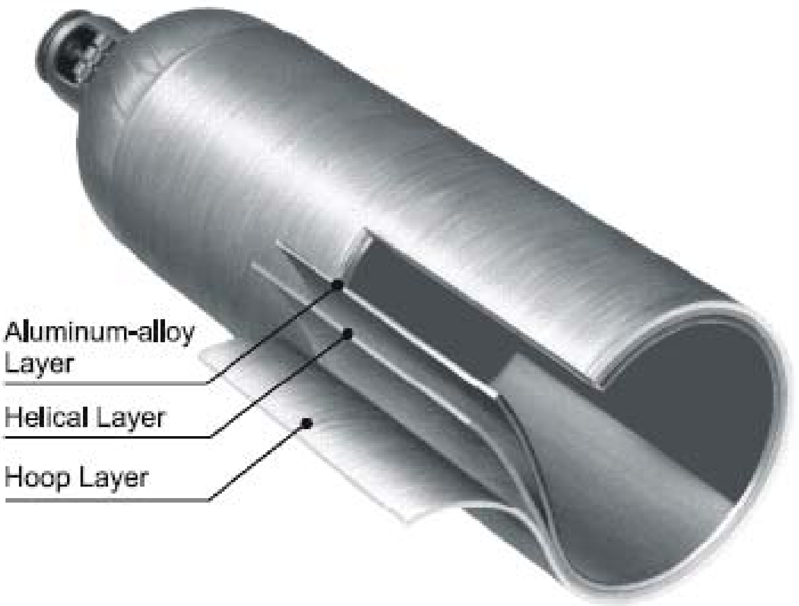

Figure 1.3.1.1: A cylinder with a thin metal liner of steel or aluminium and a fully wound composite over wrap [41]

The safety of pressurized cylinders is an issue of concern especially in highly populated regions. Future pressure vessels are envisaged to consist of three layers: an inner polymer liner over wrapped with a carbon-fiber composite and an outer layer of an aramid-material capable of withstanding mechanical and corrosion damage (fig. 1.3.1.1). Presently, the most advanced prototype tanks can store hydrogen at pressures up to 700 bar for mobile with a mass of 110 kg resulting in a gravimetric storage density of 6mass% and a volumetric storage density of 30 $kg \cdot m^{-3}$, and 825 bar for stationary, applications and have been safety tested to 2130 bar [42].

However, the potential risks associated with very high-pressure systems, and the even more risky procedure of compressing hydrogen, raises important practical problems, as there is currently no practical solution to refilling cylinders in a domestic situation to such high pressures rapidly and safely. This, coupled with the fact that the compression of hydrogen to 70 bar requires almost as much energy as liquefaction of an equivalent amount of hydrogen, leaves a lot of problems to be solved before high pressure hydrogen can become viable on a commercial scale.

3.2 Liquid hydrogen

Liquid hydrogen has been developed by Kalli and used as the fuel energy storage system for space travel since the 1960s. It is light, relative to other liquids, but the volumetric density of liquid hydrogen is 70.8 kg·m^{-3} and slightly higher than that of solid hydrogen (70,6 kg·m^{-3}), and does not need the high pressure that is required for compressed gas storage (32).

Quantum mechanical investigations of hydrogen show that there are two different kinds of hydrogen molecules: ortho-hydrogen with parallel nuclear spins and para-hydrogen with anti-parallel nuclear spins. This is responsible for the unusual behaviour of the specific heat of hydrogen at low temperatures. Normal hydrogen at room temperature contains 25% of the para form and 75% of the ortho form hydrogen. The ortho form cannot be prepared in the pure state. Since the two forms differ in energy, the physical properties also differ.

The melting and boiling points of para-hydrogen are about 0.1 K lower than those of normal hydrogen. When hydrogen is cooled from room temperature (RT) to the normal boiling point (nbp = 21.2K) the ortho-hydrogen converts from an equilibrium concentration of 75% at RT to 50% at 77K and 0.2% at nbp. The self conversion rate is an activated process and very slow, the half-life time of the conversion is greater than one year at 77K. The conversion reaction from ortho- to para-hydrogen is exothermic and the heat of conversion is also temperature dependent. The enthalpy of conversion is greater than the latent heat of vaporization (HV = 451.9 kJ·kg-1) of normal and para hydrogen at the nbp. If the unconverted normal hydrogen is placed in a storage vessel, the enthalpy of conversion will be released in the vessel, which leads to the evaporation of the liquid hydrogen. The transformation from ortho- to para-hydrogen can be catalyzed by a number of surface active and paramagnetic species. The conversion may take only a few minutes if a highly active form of charcoal is used. Other suitable ortho-para catalysts are metal such as tungsten, nickel, or any paramagnetic oxides like chromium or gadolinium oxides [43].

The simplest liquifaction cycle is the Joule-Thompson cycle (fig. 3.2.1). The gas is first compressed, and then cooled in a heat exchanger, before it passes through a throttle valve where it undergoes an isenthalpic Joule-Thomson expansion, producing some liquid. The cooled gas is separated from the liquid and returned to the compressor via the heat exchanger. The Joule-Thompson cycle works for gases, such as nitrogen, with an inversion temperature above room temperature. Hydrogen, however, warms upon expansion at room temperature. In order for hydrogen to cool upon expansion, its temperature must be below its inversion temperature of 202K. Therefore, hydrogen is usually pre-cooled using liquid nitrogen (78K) before the first expansion step occurs [37].

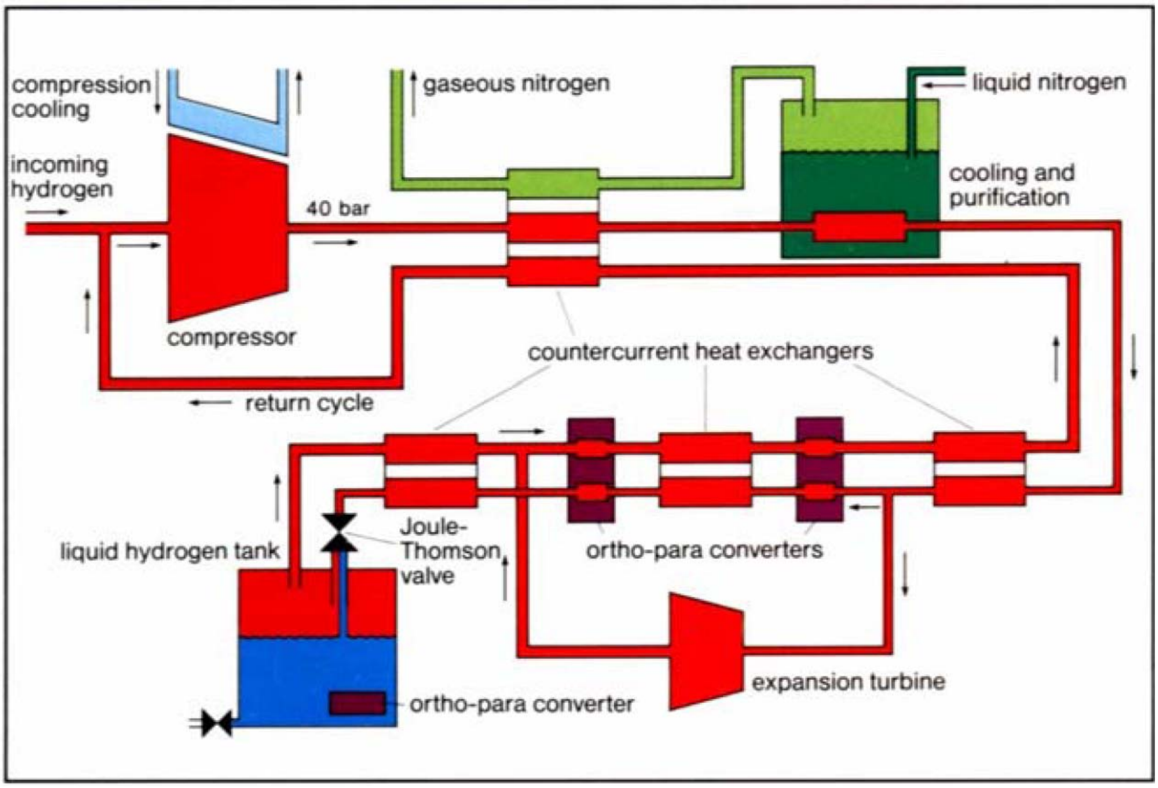

Figure 3.2.1: The Joule-Thompson cycle [37]

The energy required to liquefy hydrogen is approximately 40 mJkg^{-1}, which is about 28 % of the energy content of hydrogen. This energy requirement is one of the major problems with storing hydrogen as a liquid but expenditure is compensated for by the high volumetric density of 25,9 wt% achieved by liquid hydrogen.

One more disadvantage is that hydrogen has a liquefaction temperature around 20 K at 0,1 bar. Thus the storage system requires very efficient insulation techniques in order to minimise the unavoidable heat transfer leading to hydrogen loss via boil-off [41].

Another problem with this method of storage is caused by the massive thermal gradient between the interior and exterior of the storage vessel requiring advanced insulation techniques in order to maintain the temperature of the liquid. Even so, the high thermal gradient results in hydrogen being lost due to boil-off which varies from 0.06 % per day from large static containers to 3 % per day from tanks sized for use in cars [44].

Research is currently trying to find improved insulation and cooling methods. However, liquid hydrogen has very high volumetric energy density and, by using larger tanks, much better surface to volume ratios are possible reducing boil off. This makes liquid hydrogen better suited for refuelling stations and larger transport tanks, such as in ships and road tankers, which utilise much larger reservoirs of hydrogen. There are also pilot cars produced by General Motors. The HydroGen3 Opel Zafira minivan is specified with a driving range of 400 km with 4,6 kg liquid hydrogen versus 270 km for the 700 bar gaseous hydrogen tank described above (33).

1.3.3 Solid state materials

1.3.3.1 Metal hydrides

Hydrogen is a highly reactive element and forms hydrides and solid solutions with thousands of metals and alloys that will release hydrogen at elevated temperatures. Metal hydrides are arranged of metal atoms that form a host lattice, and hydrogen atoms that are installed in the interstitial sites. A hydride ‘family tree’ of the elements, alloys and complexes is shown in figure 1.3.3.1.1.

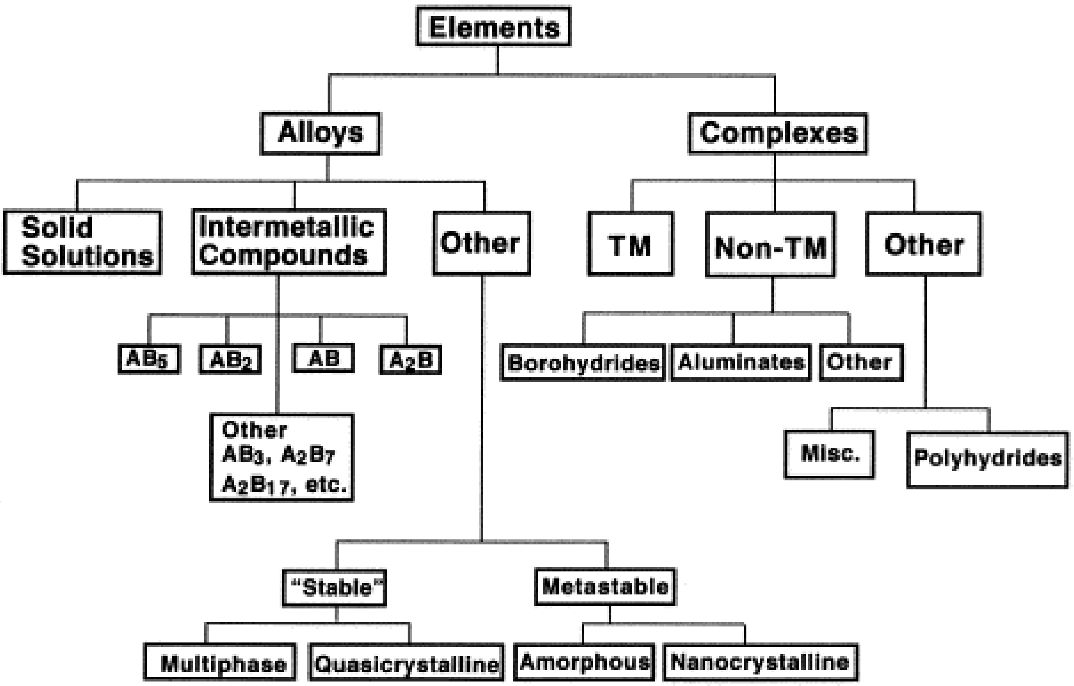

Figure 1.3.3.1.1: Family tree of hydriding alloys and complexes. TM=transition metal [45]

The absorption process of hydrogen in the metal can be described using one-dimensional Lennard-Jones potential scheme for hydrogen molecule and 2 hydrogen atoms (fig. 1.3.3.1.2) [37] The potential of molecule and both atoms are separated by the heat of dissociation energy E_D=435.99 kJ/mol in some distance from the metal surface. Approximately one hydrogen molecule radius from the metal surface the hydrogen molecule interacts with metal surface and due to the Van der Waals forces physisorption happens that is illustrated as the flat minimum in the H_2+M curve. Closer to the surface the hydrogen has to overcome an activation barrier for dissociation and formation of the hydrogen metal bond and hydrogen becomes chemisorbed that is showed as deep minimum of the 2H+M curve. If the both curves cross above zero energy level for the chemisorption activation energy is needed and the kinetics of adsorption is getting more slowly.

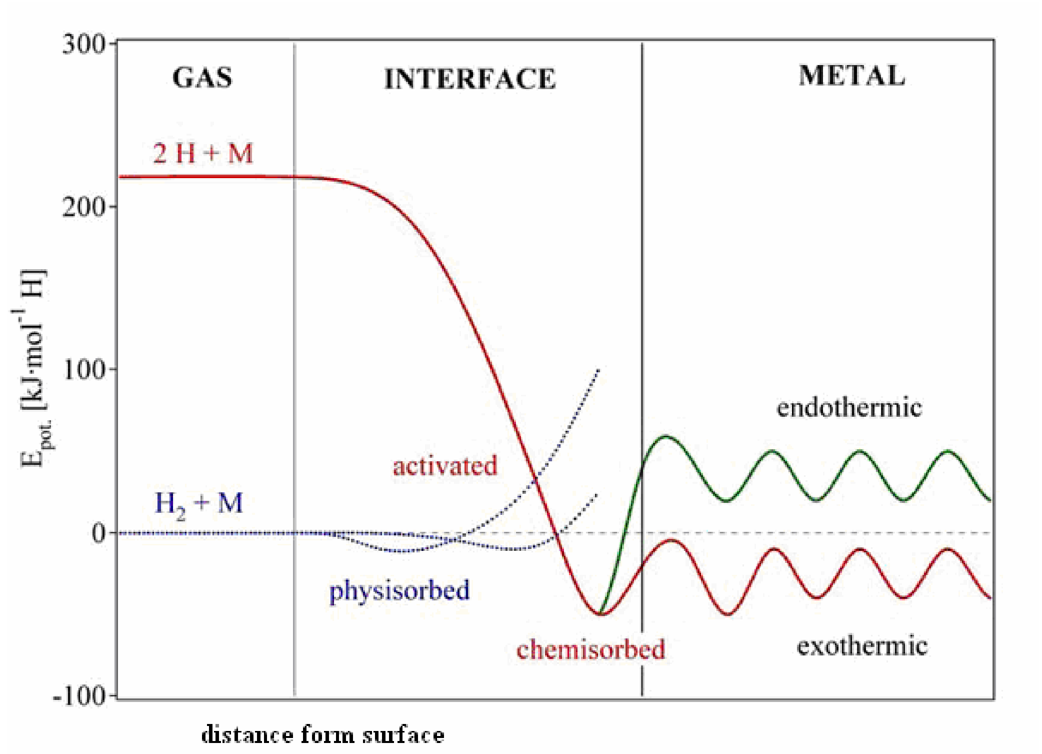

Figure 1.3.3.1.2: Potential energy curves for activated and non-activated chemisorption of hydrogen on metal surface [46].

Depending on the surface elements the activation barrier height can be changed and chemisorbed hydrogen atoms may have a high surface mobility, interact with each other and form surface phases. Furthermore the chemisorbed hydrogen atom can jump in the subsurface layer and finally diffuse on the interstitial sites through the host metal lattice (fig. 1.3.3.1.3) [47].

Hydride formation from gaseous phase can be described by pressure-composition isotherms (Fig. 4). The host metal dissolves some hydrogen and solid solution phase or α-phase is formed. The metal lattice expands proportionally to the hydrogen concentration by approximately 2 – 3Å^3 per hydrogen atom. If the hydrogen pressure and concentration Hydrogen/Metal exceeds ratio 0,1 a H–H interaction becomes significant and the β-phase nucleates and grows. While the α-phase and β-phase coexists, the isotherms show a flat plateau, the length of which determines how much H_2 can be reversibly stored.

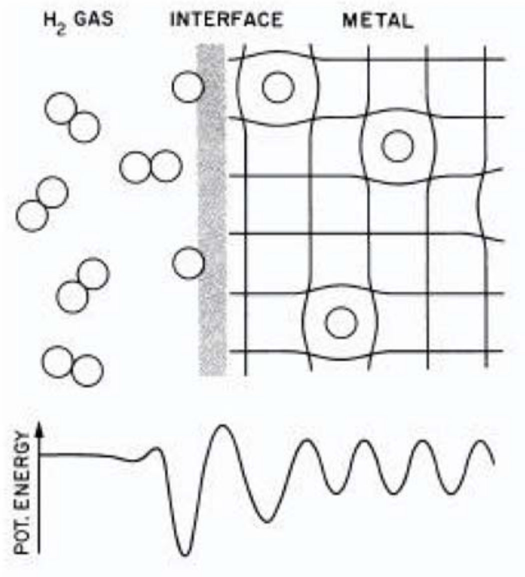

Figure 1.3.3.1.3: Simplified model of the dissociation of molecular hydrogen and migration in the bulk[48].

When the α-phase completely transfers to the β-phase, the H_2 pressure rises steeply with the concentration. Further enlargements of hydrogen pressure can cause formation of other plateaux and hydride phases. The two-phase region ends in a critical point T_C, above which the transition from α- to β-phase, is continuous (fig. 1.3.3.1.4).

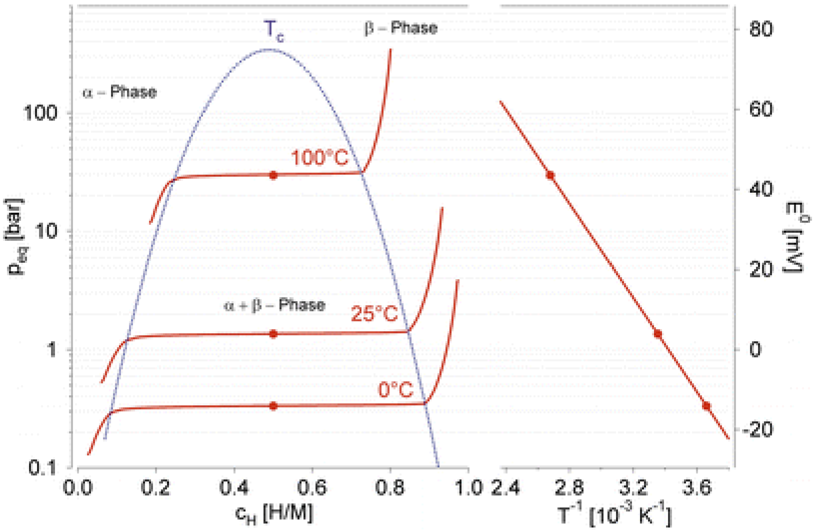

Figure 1.3.3.1.4 Pressure composition isotherms for typical intermetallic compound is shown on the left side. The construction of the Van't Hoff plot is shown on the right hand side[37].

The hydrogen concentration in the hydride phase is often found to be H/M=1. The volume expansion between the coexisting α- and the β-phase corresponds in many cases to 10–20% of the metal lattice. Therefore, at the phase boundary a large amount of stress is built up and often leads to a decrepitation of brittle host metals such as intermetallic compounds. The final hydride is a powder with a typical particle size of 10–100 μm [37, 48, 49].

The plateau pressure strongly depends on temperature that is related to the changes of enthalpy and entropy. Solving the Van 't Hoff equation and from the gained slope where the pressure is a function of temperature, the heat of hydride formation can be evaluated.

$$\ln\left(\frac{p_{eq}}{p_{eq}^{0}}\right)=\frac{\Delta H}{R}\cdot\frac{1}{T}\cdot\frac{\Delta S}{R},$$

where p_{eq} is plateau pressure at equilibrium state, p^0_{eq} stands for the plateau pressure at standard conditions, R is the universal gas constant, T is the temperature at p_{eq} and ΔH is the enthalpy change.

The enthalpy term characterizes the stability of the metal hydrogen bond. Figure 1.3.3.1.5 shows Van’t Hoff plots for some selected hydrides. There also is showed a stabilization impact of $LaNi_5$ hydrides by the partial substitution of nickel with aluminium and the substitution of lanthanum with mischmetal(Mm) e.g. 51% La, 33% Ce, 12% Nd, 4% Pr. A hydride forming entropy changes leads to great heat generation during the hydrogen absorption. The same heat has to be provided to the metal hydride to desorb the hydrogen.

Hydrogen absorption is very much involved with a phase transition. Pressure does not increase with the amount of absorbed hydrogen as long as the phase transition takes place therefore a, metal hydrides can absorb large amounts of hydrogen at a constant pressure. Hydrogen sorption characteristics can be changed by partial substitution of the hydride forming elements, thereby it is possible to form some metal hydrides that works at ambient temperature and close to atmospheric pressure[49].

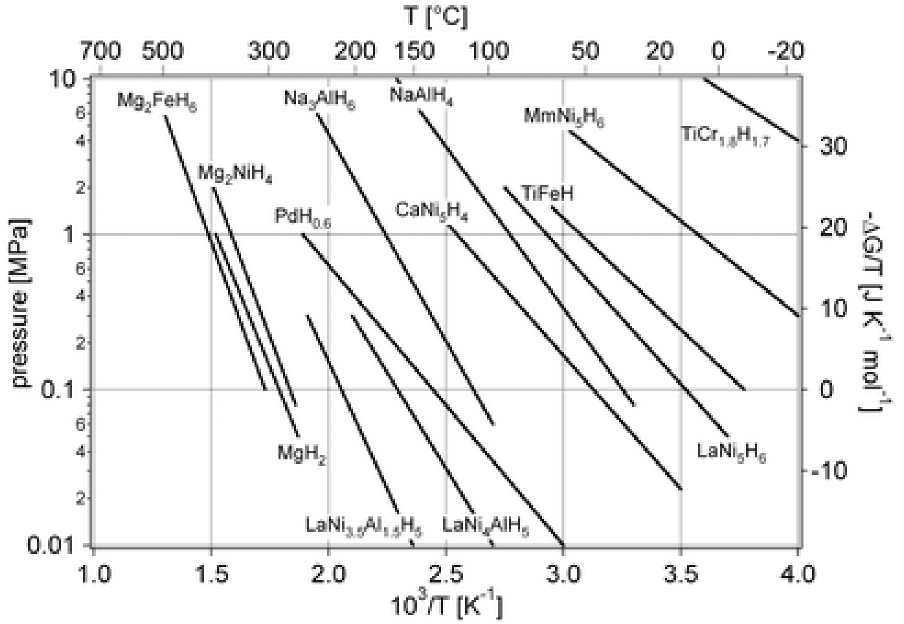

Figure 1.3.3.1.5. Van't Hoff plots of some selected hydrides[37]

A particular interest is about intermetallic hydrides because the variations of the elements allow modification of the properties of the hydrides (tab. 1.3.3.1.1). The element A usually is a rare earth or an alkaline earth metal and tends to form a stable hydride or has a high affinity to hydrogen. The B element is often a transition metal and forms unstable hydrides or has a low affinity to hydrogen. The combination of the both elements A and B gives as alloys suitable for practical applications.

Table 1.3.3.1.1: The most important hydride forming intermetallic compounds [37].

Intermetallic compound	Prototype	Hydrides	Structure
AB_5	$LaNi_5$	$LaNi_5H_6$	Hexagonal
AB_2	ZrV_2, $ZrMn_2$, $TiMn_2$	$ZrV_2H_{5,5}$	Hexagonal or cubic
AB_3	$CeNi_3$, YFe_3	$CeNi_3H_4$	Hexagonal
A_2B_7	Y_2Ni_7, Th_2Fe_7	$Y_2Ni_7H_3$	Hexagonal
A_6B_{23}	Y_6F_{23}, Ho_6Fe_{23}	$Ho_6Fe_{23}H_{12}$	Cubic
AB	TiFe, ZrNi	$TiFeH_2$	Cubic
A_2B	Mg_2Ni, Ti_2Ni	Mg_2NiH_4	Cubic

AB_5 intermetallic compounds

The on of the classical alloys is a combination of the La and Ni, where La individually forms LaH_2 at 25°C, $p=3\cdot10^{-29}$ atm, ΔH_f=-208 kJ/mol H_2, with Ni that alone forms NiH at 25°C, p=3400atm, ΔH_f=-8,8 kJ/mol H_2. Although the alloy $LaNi_5$ forms a hydride at 25°C, p=1,6 atm, ΔH_f=-30,8 kJ/mol H_2, that can be considered as a interpolation between boundaries of elemental hydride forming activities [45].

$LaNi_5$ has a CaCu5-type, structure containing three octahedral and three tetragonal sites per elemental cell unit[50]. The alloy forms at least two hydrides: α phase - $LaNi_5H_{0.3}$ - with low hydrogen content and β phase - $LaNi_5H_{5.5}$ - with high hydrogen-content. Both hydrides differ significantly in the specific lattice volume; β phase has a 25% larger lattice expansion as α phase that causes a crumbling of the alloy particles on hydriding - dehydriding cycles.

The alloy of rare earth elements in composition with nickel was used for the first time by Lindholm[51] as the electrode in the fuel cells in 1966 and then by Dilworth and Wunderlin[52, 53] in 1968. The term $MmNi_5$ was used where Mm (mischmetal)-represents a natural mixture of rare earth elements, mostly consisting of Ce (30-52 wt%), La (13 to 25 wt%), Nd, Pr and Sm (13-57 wt%) where an amount and elements of additives depends on the place of origin[54].

Though, the element substitutions in the AB_5-type alloys have been made also artificially to get better alloys for practical use. La can be replaced with Mm, Ce, Pr, Nd, Zr, Hf and Ni can be exchanged with Al, Mn, Si, Zn, Cr, Fe, Cu, Co; thereby altering the hydrogen storage capacity, the stability of the hydride phase or the corrosion resistance. For example, a partial replacement of the A and B components significantly changes macrostructure of an alloy and other properties (see tab. 1.3.3.1.2).

The stoichiometry of an alloy influences its durability in the long-term hydriding - dehydriding cycles, and typical commercial AB_5-type alloys consists of at least 5-6 different metals, for example $La_{0.64}Ce_{0.36}Nd_{0.46}Ni_{0.95}Cr_{0.19}Mn_{0.41}Co_{0.15}$ (Hydralloy F from Nürnberg, Germany) [55].

Table 1.3.3.1.2: Effect on composition on properties of AB_5-type alloys [50]

Composition	***Elements and their role***
Substitutions of A in AB_5 $La_{1-y}M_yB_5$	Zr, Ce, Pr, Nd decrease the unit cell volume, improve activation, high-rate discharge and cycle life, but increase the self-discharge due to a higher dissociation pressure of the metal hydride. The use of Mm instead of La reduces the alloy costs.
Substitutions of B in AB_5 $A(Ni_{1-z}M_z)_5$	A= La, Mm; M= Co, Cu, Fe, Mn, Al; 0<z<0.24 **Ni (**1-z)>2.2 is indispensable to prevent the decrease of the amount of absorbed hydrogen and the electrode capacity **Co** decreases the volume expansion upon hydriding, retards an increase of the internal cell pressure, decreases the corrosion rate and improves the cycle life of the electrode, especially at elevated temperature (40 C), but increases the alloy costs **Substitution of Co by Fe** allows cost reduction without affecting cell performance, decreases decrepitation of alloy during hydriding. **Al.** increases hydride formation energy, prolongs cyclic life. **Mn** decreases equilibrium pressure without decreasing the amount of stored hydrogen. **V** increases the lattice volume and enhances the hydrogen diffusion. **Cu** increases high rate discharge performance.
Special additions to B in AB_5 $A(Ni,M)_{5-x}B_x$	A= La, Mm; M = Co, Cu, Fe, Mn, Al; B= Al, Si, Sn, Ge, In, Tl, **Al, Si, Sn and Ge** – minimise corrosion of the hydride electrode. **Ge-**substituted alloys exhibit facilitated kinetics of hydrogen absorption/desorption in comparison with Sn-containing alloys. **In, Tl, Ga** increase overvoltage of hydrogen evolution (prevent generation of gaseous hydrogen).
Nonstoichiometric alloys $AB_{5\pm x}$	A= La, Mm; B=(Ni,Mn,Al,Co,V,Cu) Additional **Ni** forms separate finely dispersed phase. In **$MmB_{5.12}$** the **Ni_3Al**-type second phase with high electrocatalytic activity is formed. **Alloys poor in Mm** are destabilised and the attractive interaction between the dissolved hydrogen atoms increases. Second phase **(Ce_2Ni_7)**, which forms very stable hydride is present in $MmB_{4.88}$,. When (5-x)<4.8, the hydrogen gas evolution during overcharge decreases.
Addition of alloys with increased catalytic activity $AB_5 + DE_3$	D= Mo, W, Ir; E= Ni, Co **DE_3** is a catalyst for hydrogen sorption-desorptionreactions.
Mixture of two alloys $A^1B^1{}_5 + A^2B^2{}_5$	Mixing of two alloys characterised by various hydrogen equilibrium absorption pressures increases the electrode performance.

AB, AB_2 intermetallic compounds

Different groups of materials release hydrogen at near ambient temperature and pressure are defined as low temperature hydrides. Their reversible hydrogen storage density is usually between 1,5 to 1,8 wt%. This group of hydride alloys is made from elements belonging to the IIIB and IVB group of the periodic table (making a very stable hydrides-element A) and the transition metals from the VB, VIB, VIIB and VIII groups (element B): AB, A_2B, AB/AB_2 and AB_2-type alloys [56]. These alloys can roughly be arranged in two classes:

(1) Type A_2B, AB and AB/A_2B based on Ti_2Ni and TiNi;

(2) Type AB_2 or Laves-phase system which crystallize in a cubic C15 and hexagonal C14 or C36 structure - $ZrNi_2$, ZrV_2 and ZrMn [56, 57]

AB and A_2B alloys have been used mostly for scientific investigations due to the decomposition in hydriding-dehydriding cycles that gives a low specific capacity. The hydriding-dehydriding behavior of AB/AB_2-type alloys is strongly influenced by their composition and stoichiometry as well as by the microstructure of the material particles, and the presence of additives and impurities [50]. For example, formation of a compact ZrO_2 layer is a serious problem in zirconium alloys because the transport of hydrogen into an oxide layer is very slow and catalytic activity of oxidized surfaces is low. A partial replacement of Zr by Ti and or Mn by Cr is reduces a problem but the hydrogen storage capacity of an alloy decreases with increasing the content of additives (tab. 1.3.3.1.3).

Table 1.3.3.1.3: Effect of composition on properties of AB and AB$_2$-type alloys[50].

Composition	***Elements and their role***
ZrM_2 - type alloy M= V, Cr, Mn, Ni $Zr(V_xNi_{1-x})_2$	An increase of the V content increases the maximum amount of absorbed hydrogen. Ni substitution decreases the electrochemical activity of an alloy. Composite alloy - mixture of $ZrNi_2$ with RNi_5 (R= rare earth element) shows improved characteristics in comparison with yhe parent compounds.
ZrB_2 - type alloy $ZrNi_{1.2}Mn_{0.6}V_{0.2}Cr_{0.1}X_x$ Over-stoichiometric alloy : $ZrV_{1.5}Ni_{1.5}$	X= La or Ce; x=0.05 La and Ce do not dissolve in the Laves phase but precipitate in the matrix, improve the activation behaviour of alloy during chemical pretreatment and increases discharge capacity. In stoichiometric AB$_2$–type alloy the distribution of A and B elements on the A and B sites is crucial for high hydrogen storage capacity; the over-stoichiometric alloy, in which some of the V atoms move from B to A sites shows very high capacity.
TiFe -type alloy $TiFe_{1-x}Pd_x$	Pd substitution increases both the lattice constant and the catalytic activity, decreases the plateau pressure.
Vanadium-based alloys $V_3Ti(Ni_{1-x}M_x)$ $V_3TiNi_xM_y$	M= Al, Si, Mn, Fe, Co, Cu, Ge, Zr, Nb, Mo, Pd, Hf, Ta Phase structure is composed of the V-based solid solution as the main phase and the TiNi-based secondary phase; the addition of Co, Nb and Ta improves cycling durability. Alloys with Hf (or Nb), Ta and Pd show higher discharge capacity. M=Hf improves the high rate capability. TiNi phase exhibits high electrocatalytic activity.
Substitution of A in the AB$_2$ A = Zr + Ti $Ti_xZr_{1-x}Ni_{1.1}V_{0.5}Mn_{0.2}Fe_{0.2}$	Zr contributes to an increase of the amount of stored hydrogen and induces formation of the C15-type desired phase structure. Ti increases the equilibrium pressure of hydrogen and decreases the electrochemical capacity. Electrodes without Ti, or a very low Ti content, exhibit excellent cycling and electrochemical stability. Electrodes withTi:Zr atomic ratio 2:1 displays higher storage capacity than that with Ti:Zr =1:1 and higher electrochemical activity. Amount of C15 phase decreases with increasing x, at x= 0.5 it is pure C14 phase, at x= 0.75 it is 13% cubic bcc phase + 87% C14 phase; bcc phase absorbs more hydrogen than the C14 hexagonak phase.
Substitution of B in the AB$_2$ $Zr_{0.8}Ti_{0.2}(V_{0.3}Ni_{0.6}M_{0.1})_2$ $Ti_{0.35}Zr_{0.65}Ni_{1.2}V_{0.6}Mn_{0.2}Cr_{0.2}$	The Si, Mn-substituted alloys has C14 Laves phase structure. The Co, Mo-substituted alloys form C15 Laves phase structure. Mn enhances the activation of an alloy during chemical pretreatment and increases discharge capacity. Co addition leads to the longest cyclic life-time. Cr addition reduces the discharge capacity but extends cyclic life-time; Cr controls the dissolution of V and Zr.

Nonstoichiometric alloys $AB_{2\pm x}$ $Zr_{0.495}Ti_{0.505}V_{0.771}Ni_{1.546}$ $Ti_{0.8}Zr_{0.2}Ni_{0.6}V_{0.64}Mn_{0.4}$ $ZrV_{0.8}Ni_{1.2}Mn_{0.4}$	Increasing the Ni content decreases V-rich dendrite formations; C14-type Laves phase preserves an over-stoichiometric alloy and discharge capacity increases on increasing the amount of Ni.
MgNi- based alloys for electrodes Optimum ternary alloy $Mg_{50}Ni_{45}M_5$ (M= Mn, Cu, Fe)	Ni substitution with Zn increases the deterioration rate. Substitution of Fe, W, Cu, Mn, Cr, Al or C instead of Ni decreases both the deterioration rate and discharge capacity. Ni substitution by Se, Cu, Co or Si decreases both the discharge capacity and cycling life.

The Ovonic alloy $Zr_{0.55}Ti_{0.45}V_{0.55}Ni_{0.88}Cr_{0.15}Mn_{0.24}Co_{0.18}Fe_{0.03}$ is a multiphase structure, which involves a specific grain phase for the reversible storage of hydrogen and a primary inter-granular phase capable of catalyzing oxidation of hydrogen. Many important manufacturers of Ni-MH batteries operate at present under agreements with Ovonic Battery Company. Ovonic Ni-MH electric vehicle battery packs have been installed on a number of prototype electric vehicles, like Solectria and the Chrysler's Tevan. Nevertheless, there is a problem with the activation of Ovonic alloy during the first cycles of operation [58, 59]. Table 1.3.3.1.4 gives sorption properties for some of the intermetallic compounds.

Table 1.3.3.1.4: Hydrogen absorption/desorption properties of intermetallic compounds [60]

Material	**Temperature (°C)**	**Pressure (bar)**	**Max wt% of H_2**
$La_{0.90}Ce_{0.05}Nd_{0.04}Pr_{0.01}Ni_{4.63}Sn_{0.32}$	T_{abs} and T_{des}: 100, 25	P_{abs}: 5–10;P_{des}: 0.24	0.95
$Zr(Cr_{0.8}Mo_{0.2})_2$	T_{abs}: 120	P_{abs}: 30	0.99
$LaNi_{4.8}Sn_{0.2}$	T_{des} and T_{abs}: 80	P_{des}: 3–4	1.16
$La_{0.55}Y_{0.45}Ni_5$	T_{des}: −20	P_{des}: 3.5	1.30
$Ti_{0.9}Zr_{0.15}Mn_{1.6}Cr_{0.2}V_{0.2}$	T_{des}: 25	P_{des}: 10	1.30
$MmNi_{4.6}Al_{0.4}$	T_{abs} and T_{des}: 25	P_{des}: 25	1.30
$MmNi_{4.6}Fe_{0.4}$	T_{abs} and T_{des}: 25	P_{abs}: 35	1.44
80 wt% $TiCr_{1.1}V_{0.9}$–20 wt%	T_{abs} and T_{des}: 30	P_{abs}: 17	1.50
$Ti_{0.97}Zr_{0.03}Cr_{1.6}Mn_{0.4}$	T_{abs}: 20	P_{abs}: 100;P_{des}: 81	1.55
$La_{0.7}Mg_{0.3}Ni_{2.65}Mn_{0.1}Co_{0.90}$	T_{abs} and T_{des}: 30	P_{abs}: 5; P_{des}: 0.33	1.56
$Zr_{0.75}Ti_{0.25}Cr_{1.5}Ni_{0.5}$	T_{abs}: 40	P_{abs}: 47	1.75
$Ti_{1.1}CrMn$	T_{abs} and T_{des}: 23	P_{abs}: 33; P_{des}: 1	1.80
FeTi	T_{abs}: 25	P_{abs}: 100	1.92
V–7.4%Zr–7.4%Ti–7.4%Ni	T_{abs}: 40	P_{abs}: 10; P_{des}: 1	2.00
$V_{0.375}Ti_{0.25}Cr_{0.30}Mn_{0.075}$	T_{abs} and T_{des}: 30	P_{abs}: 50; P_{des}: 0.2	2.20
$Ti_{45}Zr_{38}Ni_{17}$	T_{abs}: 300	P_{abs}: 80	2.23
Ti–V–Cr	T_{abs} and T_{des}: 40	P_{abs}: 100	2.80
Ti–10Cr–18Mn–32V	T_{abs}: 60	P_{abs}: 30; P_{des}: 1	3.36
$TiCr_{1.1}V_{0.9}$	T_{abs} and T_{des}: 30	P_{abs}: 17; P_{des}: 0.5	3.50
Ti–V–Cr–Mn	T_{des}: 247–472	P_{abs}: 30; P_{des}: 0.03	3.98
$La_{1.8}Ca_{0.2}Mg_{14}N_{13}$	T_{abs} and T_{des}: 27–327	P_{abs}: 40; P_{des}: 1	5.00
$LaNi_5$	T_{abs}: 20	P_{abs} : 20	0.25
$La_{0.59}Ce_{0.29}Pr_{0.03}Ni_4Co_{0.45}Mn_{0.45}Al_{0.3}$	T_{abs}: 60	P_{abs}: 10; P_{des}: 0.6	1.27
$La_{0.9}Ce_{0.1}Ni_5$	T_{abs}: 0–100;T_{des}: 25	P_{abs}: 50	1.40
$LaNi_5$	T_{abs}: 0–100;T_{des}: 25	P_{abs}: 50	1.44

Other intermetallic compounds as A_2B, AB_3, A_2B_7, A_3B, etc. have either good hydrogen capacities but do not have favorable PCT properties or these with suitable PCT properties usually have poor hydrogen capacities or too narrow plateaus.

Magnesium hydride is directly formed from the reaction of hydrogen gas with elemental magnesium and currently has the highest reversible capacity - 7.6 wt%. The main disadvantage of this alloy is the large enthalpy of formation, which results in high operating temperatures ~300 ^{o}C and a slow reaction kinetics. Faster sorption kinetics can be reached by the use of suitable catalysts such as Nb and V and proper preparation methods as nanostructuring of powders. On the other hand, alloying with a 3d transition metals can lead to a reduction of the reaction enthalpy but that causes a reduction of the gravimetric storage density below 3.6 wt.% (tab. 1.3.3.1.5) [61].

Higuchi *et al.* [62] have discovered that palladium coated nanostructured magnesium films are able to adsorb approximately 5 wt% at 100 °C under a hydrogen atmosphere of 1 bar and completely desorbs below 100 °C under vacuum.

Initially just few ternary hydrides between magnesium and alkali or alkaline-earth elements were investigated. One of the first fully characterized examples was $Ca_4Mg_3H_{14}$ that has been reported in 1992. Ternary hydrides between magnesium and alkali or alkaline-earth elements that were investigated until 1997 are described in the Hydride–Fluoride Crystal Structure Data Base (fig. 1.3.3.1.6) [63].

The highest recently referred volumetric hydrogen density for Mg_2FeH_6, accordingly – 48w%. However, all hydrides with a hydrogen to metal ratio of >2 are ionic or covalent compounds and belong to the complex hydrides [64, 65].

Table 1.3.3.1.5 (left side): Compositions, structural properties and hydrogen storage efficiencies of magnesium based ternary metal hydrides containing alkali (A) and alkaline-earth (Ae) or lanthanide elements (Eu, Yb) (adapted from [64])

[b] Relative volume contraction compared to weighted sums of volumes of corresponding binary hydrides

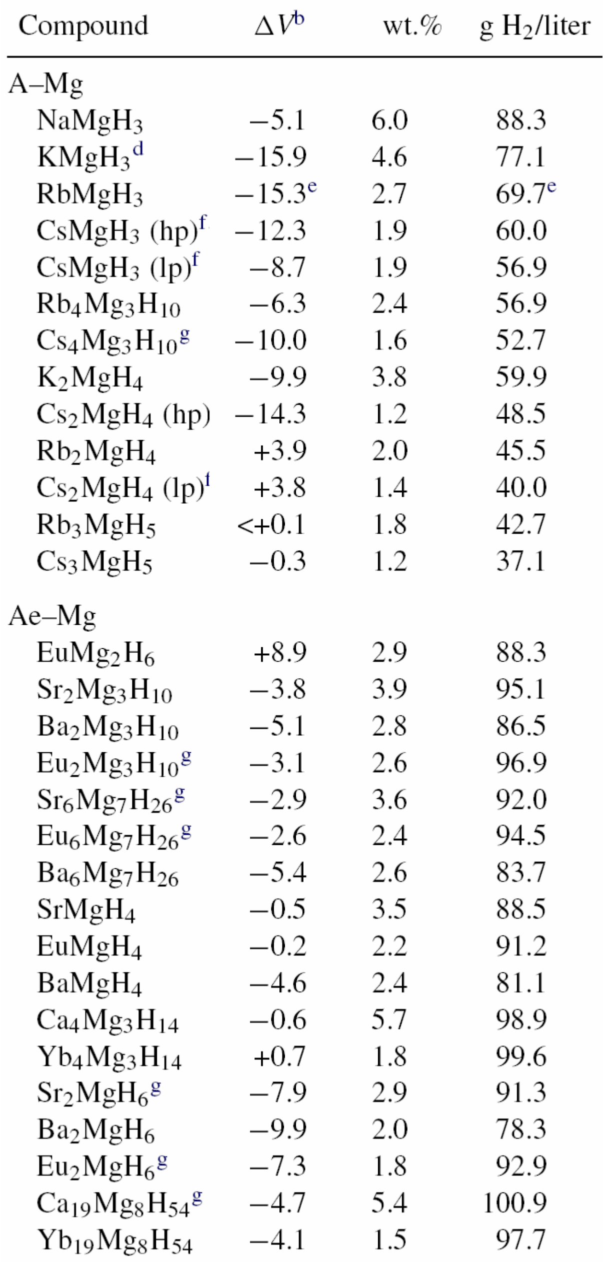

Compound	ΔV^b	wt.%	g H_2/liter
A–Mg			
$NaMgH_3$	−5.1	6.0	88.3
$KMgH_3{}^d$	−15.9	4.6	77.1
$RbMgH_3$	-15.3^e	2.7	69.7^e
$CsMgH_3$ (hp)^f	−12.3	1.9	60.0
$CsMgH_3$ (lp)^f	−8.7	1.9	56.9
$Rb_4Mg_3H_{10}$	−6.3	2.4	56.9
$Cs_4Mg_3H_{10}{}^g$	−10.0	1.6	52.7
K_2MgH_4	−9.9	3.8	59.9
Cs_2MgH_4 (hp)	−14.3	1.2	48.5
Rb_2MgH_4	+3.9	2.0	45.5
Cs_2MgH_4 (lp)^f	+3.8	1.4	40.0
Rb_3MgH_5	<+0.1	1.8	42.7
Cs_3MgH_5	−0.3	1.2	37.1
Ae–Mg			
$EuMg_2H_6$	+8.9	2.9	88.3
$Sr_2Mg_3H_{10}$	−3.8	3.9	95.1
$Ba_2Mg_3H_{10}$	−5.1	2.8	86.5
$Eu_2Mg_3H_{10}{}^g$	−3.1	2.6	96.9
$Sr_6Mg_7H_{26}{}^g$	−2.9	3.6	92.0
$Eu_6Mg_7H_{26}{}^g$	−2.6	2.4	94.5
$Ba_6Mg_7H_{26}$	−5.4	2.6	83.7
$SrMgH_4$	−0.5	3.5	88.5
$EuMgH_4$	−0.2	2.2	91.2
$BaMgH_4$	−4.6	2.4	81.1
$Ca_4Mg_3H_{14}$	−0.6	5.7	98.9
$Yb_4Mg_3H_{14}$	+0.7	1.8	99.6
$Sr_2MgH_6{}^g$	−7.9	2.9	91.3
Ba_2MgH_6	−9.9	2.0	78.3
$Eu_2MgH_6{}^g$	−7.3	1.8	92.9
$Ca_{19}Mg_8H_{54}{}^g$	−4.7	5.4	100.9
$Yb_{19}Mg_8H_{54}$	−4.1	1.5	97.7

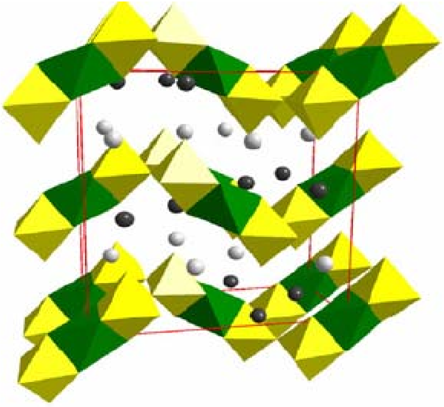

$A_4Mg_3H_{10}$ (A= Rb, Cs)

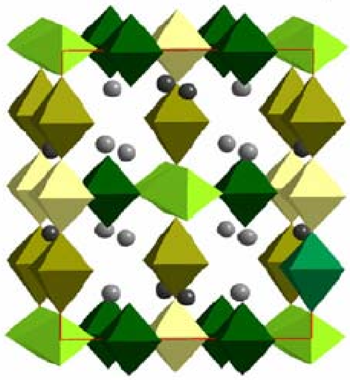

$Ba_6Mg_7H_{26}$

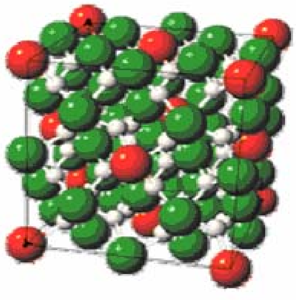

Mg_7TiH_{16}

Figure 1.3.3.1.6 (right side): Structure of the Mg_7TiH_{16} The hydrogen ions sit in tetrahedral holes of the cubic Mg-Ti lattice, Mg-green, Ti-red, H-gray [66]

1.3.3.2 Complex hydrides

Complex hydrides are formed from light elements as Li, Mg, B, Al and build a large variety of metal–hydrogen complexes that can absorb two hydrogen atoms per metal atom in many cases. The tetrahydroborates $M(BH_4)$, and the tetrahydroaluminate $M(AlH_4)$ are promising storage materials; however, they form a very stable hydrides and decompose only at elevated temperatures and often above the melting point of the complex. Bogdanovich *et al.* reported the adsorption at 180°C and desorption at 210°C for catalysed $NaAlH_4$, besides the system reversibly absorbed and desorbed hydrogen up to 4.2 mass%. Later they found a new results where a desorption hydrogen pressure was 2 bar at 60°C of Ti-doped $NaAlH_4$,that indicates that the equilibrium hydrogen pressure at room temperature is approximately 1 bar and the reaction is reversible[67]. The sorption properties for sodium alanates are provided in Table 1.3.3.2.1.

Table 1.3.3.2.1: Hydrogen absorption/desorption properties of sodium alanates (adapted from[60])

Material	**Temperature (C°)**	**Pressure (bar)**	**Max wt% of H_2**
Na_3AlH_6	T_{des}: 200	P_{des}: 1	2.50
Na_2LiAlH_6	T_{abs}: 211	P_{abs}: 45	2.50
$NaAlH_4$–2 mol%	T_{abs} and T_{des}: 125–165	P_{abs} and P_{des}: 101–202	3.00
$Zr(OPr^i)_4$ $NaAlH_4$–4 mol% Ti	T_{abs}: 120	P_{abs}: 120	3.30
	T_{des}: 150	P_{des}: 1	
$NaAlH_4$–2 mol% Ti	T_{des}: 25–160	P_{abs}: 20–120	3.80
	T_{abs}: 25–193	P_{des}: 1	
$NaAlH_4$–2 mol%	T_{abs}: 120	P_{abs} and P_{des}: 60–150	4.00
$(Ti(Obu^n)_4$	T_{des}: 180–260		
$NaAlH_4$–2 mol%	T_{abs}: 135–120	P_{abs} and P_{des}: 150–130	4.00
$Ti(Obu^n)_4$	T_{des}: 180–160		
$NaAlH_4$–2 mol% $TiCl_3$	T_{des}: 125–100	P_{des}: 83–91	4.00
$NaAlH_4$–2 mol%	T_{des}: 200	P_{des}: 1	4.00
$Zr(OPr)_4NaAlH_4$–2 mol%	T_{abs}: 104	P_{abs}: 88	4.00
$(Ti(Obu^n)_4)NaAlH_4$	T_{abs} and T_{des}: 80–180	P_{abs} and P_{des}: 76–91	5.00
$NaAlH_4$–2 mol%	T_{des}: 200	P_{des}: 1	5.00
$Ti(Obu^n)_4$-C $NaAlH_4$–2 mol% TiN	T_{abs}: 104–170	P_{abs}: 115–140	5.00

The compound with the highest gravimetric hydrogen density at room temperature is $LiBH_4$ (18 mass%) and that could be the ideal hydrogen storage material for mobile applications (tab. 1.3.3.2.2). Tough there is very little known about the mechanism of the thermal hydrogen desorption from $LiBH_4$ and the absorption and further investigations is necessary. Also $Al(BH_4)_3$, is a new complex hydride with a gravimetric hydrogen density of 17 mass% and the highest known volumetric hydrogen density of 150 $kg \cdot m^{-3}$. Furthermore, the melting point for $Al(BH_4)_3$ is –65°C that means that it is liquid at room temperature that is the only liquid hydride at room temperature (without regard to the covalent hydrocarbons).

Table 1.3.3.2.2 Hydrogen absorption/desorption properties of Li based hydrides (adapted from [60]).

Material	**Temperature, °C**	**Pressure (bar)**	**Max wt% of H_2**
$LaNi_3BH_3$	T_{abs}: 25	P_{abs}: 4	0.84
Li_2NH	T_{abs} and T_{des}: 230–200	P_{abs}: 7	3.10
		P_{des}: 1	
$LiNH_2$–LiH–1 mol%	T_{des}: 150–250	P_{abs}: 30	5.00
$TiCl_3$	T_{abs}: 180		
Li_2O–Li_3N	T_{abs}: 180	P_{abs}: 7	5.20
$Li_2MgN_2H_2$	T_{abs} and T_{des}: 180	P_{abs}: 90	5.50
		P_{des}: 1	
Li_3N	T_{abs}: 50	P_{abs}: 0.5	6.00
	T_{des}: 240–270	P_{des}: 1	
Li_2NH	T_{abs} and T_{des}: 255–285	P_{abs}: 10	6.50
		P_{des}: 1.5	
$Li_3BN_2H_8$	T_{des}: 250–364	P_{des}: 1	10.00
$LiBH_4$-0.5MgH_2–2 mol%	T_{abs} and T_{des}: 315–450	P_{abs}: 4.5–19	10.00
$TiCl_3$		P_{des}: 2–3	

Commonly metal hydrides are very effective for storing large amounts of hydrogen in a safe and compact way but they are mostly heavy or working in the not suitable conditions for vehicle applications. The transition hydrides are reversible and works around ambient temperature and atmospheric pressure but the gravimetric hydrogen density is limited to <3 mass%. It is still a challenge to explore the properties of the lightweight metal hydrides or investigate new hydride composite materials.

1.3.3.3 Glass microspheres

A relatively new concept of high pressure gas storage in commercially available microballoons was studied by Teitel *et al.*[68]. They offered a potentially advantageous lightweight, low cost, and simply designed system for compressed hydrogen gas storage by glass micro encapsulation. Yan *et al.* investigated storage of compressed hydrogen gas in cylindrical glass microcapsules [69].

The storage model is established on the exponential temperature dependence of the permeability of hydrogen through a glass wall. Hollow glass microspheres in diameter 50-200µm are heated and pressurized until the spheres are saturated with hydrogen. Afterwards the temperature is reduced and the hydrogen overpressure removed, thereby the gas is captured in the volume of the spheres (fig. 1.3.3.3.1).

To charge the microspheres with hydrogen gas a pressure of at least 450 bars at a temperature of *ca* 400°C is needed. An operation temperature of 200°C is necessary for extraction of hydrogen. The capacity of 5- 6 wt % have been achieved at 490 bars, although, the volumetric density is just 0.01 kg/l. To load and remove 1 kilogram of hydrogen around 1,13 kWh energy is needed [70].

Duret and Saudin [71] affirms that the tested mechanical strength for external overpressure and for hydrogen internal pressure of microspheres can be up to 1500 bar.

Though, there have to be solved a problem of an aging of the glass, uniformity of spheres, breakage and other handling disadvantages of fragile materials to include this hydrogen storage technology into everyday usage.

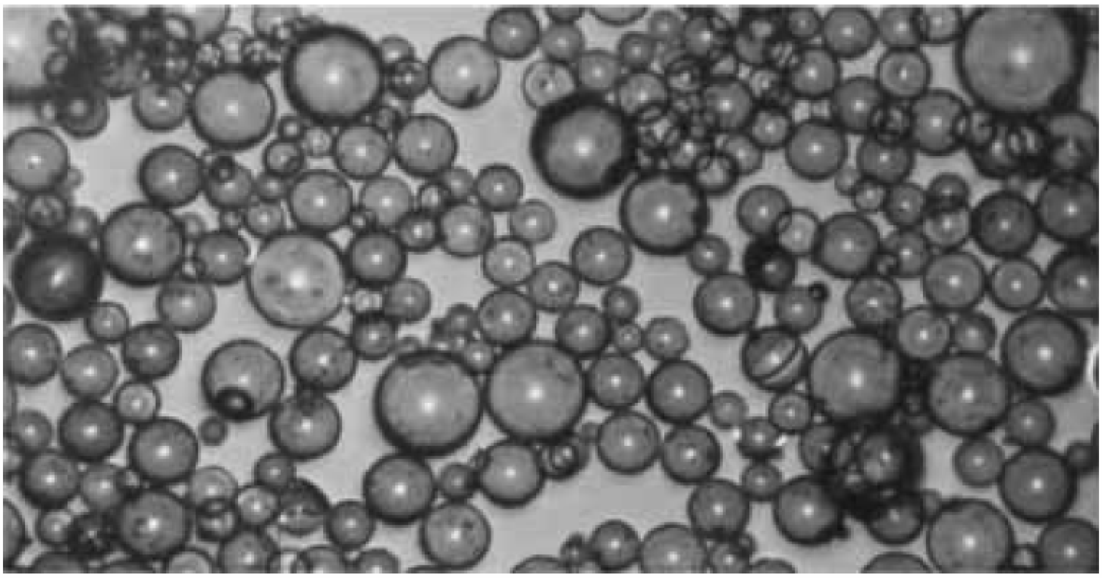

Figure 1.3.3.3.1: Microspheres for hydrogen storage[68]

1.3.3.4 Porous media.

Low temperature hydrogen storage is based mostly on a physisorption phenomenon which is based on weak van der Waals forces between adsorbate and adsorbent and observed typically in porous systems. The porous materials include carbon nanotubes, nanofibres, cubic boron nitride alloys, organics, polymers, zeolites, aerogels and porous silicon. Hydrogen storage by gas compression, liquefaction, or in the form of metal hydrides has various disadvantages – low volume/weight density of stored hydrogen, cryogenic temperatures, heavy weight, costly systems etc. Porous systems can offer the advantage of lower pressure hydrogen storage, increased safety, design flexibility and reasonable volumetric storage efficiency. However, the technology is not yet well established mostly due to the low temperatures; under -100°C [72].

Various carbon materials, such as carbon nanotubes, activated carbon, fullerens and carbon nanofibers have attracted a lot of interest; however, the values for their hydrogen storage capacity alternate over in the large amplitude. At present hydrogen storage capacities in carbon materials at room temperature are less than 1 wt%, however, higher values can be reached by lowering the temperature.

The density functional calculations have shown that theoretically in proper conditions a single-walled nanotube (SWNT) can adsorb over 14 wt% and a multi-walled nanotube (MWNT) about 7.7 wt% of hydrogen.

Figure 1.3.3.4.1 shows a top and side views of various hydrogen adsorptions in (5,5) SWNT. Insert (a) and (b) describes the initial geometry of hydrogen atoms adsorbed at the interior of the wall for θ=1,0. In the next configuration, (c) and (d), the fully relaxed geometry of (a), whereas insert (e) and (f) shows the fully relaxed geometry for θ=1,2 where θ is the coverage that is defined as the ratio of the number of hydrogen atoms to the number of carbon atoms [73].

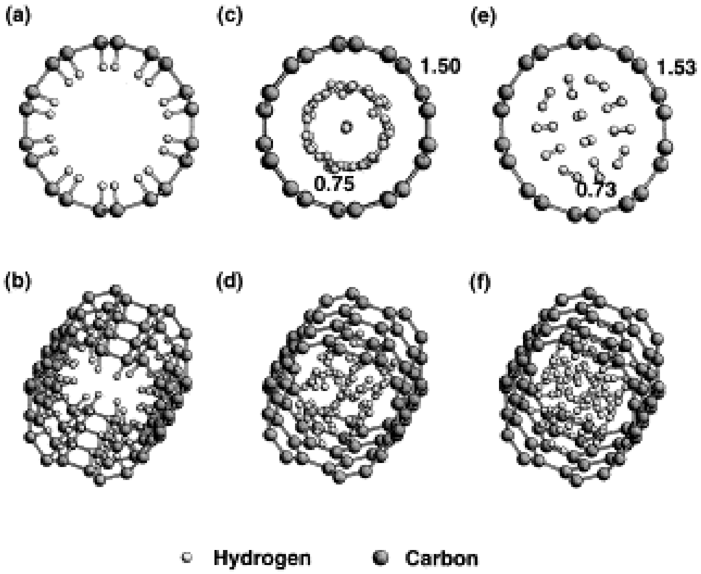

Figure 1.3.3.4.1: Various hydrogen adsorption cases in (5,5) SWNT Bond lengths are expressed in Å.

Figure 1.3.3.4.2 shows top and the side views of various hydrogen adsorptions in (10,10) SWNT; where (a) and (b) describes the geometry of (10,10) CNT for θ=2.0, and configuration (c) and (d) for a θ=2.4.

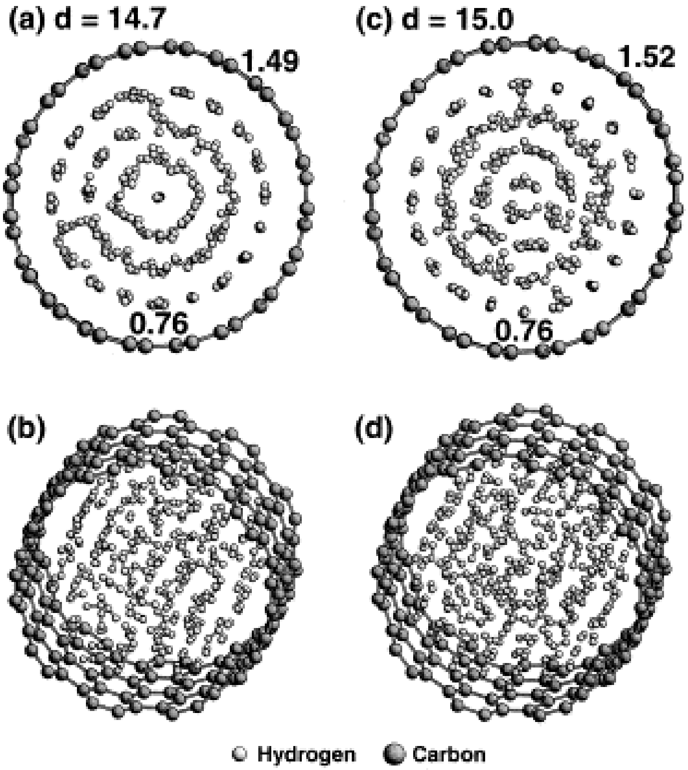

Figure 1.3.3.4.2 Various hydrogen adsorption cases in (10,10) SWNT, bond lengths are expressed in Å.

Calculations indicate that hydrogen can be adsorbed at the outer surface of the tube wall by H-C bonds with a H/C coverage 1.0 or inside the tube by H-H bonds with a coverage up to 2.4, as shown in Figures 1.3.3.4.1 and 1.3.3.4.2 [73]. The adsorption into the interior wall of the tube is also possible but as observed the bond isn't enough stable. The hydrogen relaxes inside the tube forming H-H bonds.

Lee *et al.* supposed that multi-walled nanotubes that consist from SWNT can adsorb hydrogen between them[74]. The hydrogen causes the radius of the tubes to increase and thus makes a multi-walled nanotube less stable. In nanotube bundles hydrogen can also be adsorbed in the middle of different tubes. Recent results on hydrogen storage in carbon nanotubes are summarized in Table 1.3.3.4.1 [75].

Table 1.3.3.4.1: Summary of experimentally reported hydrogen storage capacities in carbon nanotubes (graphite nanofibers (GNFs), K-doped MWNTs, Li-doped MWNTs)

Material	Gravimetric H storage amount, wt%	Storage temperature, K	Stporage pressure, MPa
SWNTs (low purity)	5-10	273	0,04
SWNTs (high purity)	3,5-4,5	298	0,04
SWNTs (50% purity	4,2	300	10,1
GNFs (tubular)	11,26	298	11,35
GNFs (herring bone)	67,55	298	11,35
GNFs (platelet)	53,68	298	11,35
Li-MWNTs	20	473-673	0,1
K-MWNTs	14	<313	0,1
CNFs	5-10	300	10,1
Li/K GNTs	10	300	8-12
GNFs	6,5-10	300	8-12
MWNTs	5	300	10
Nano-structured graphite (SWNTs)	7,4	300	1

There is developed that the amount of the physisorbed hydrogen depends almost linearly on the specific surface area. Therefore the authors [76] believe that the hydrogen adsorption process is based on the local interaction between the hydrogen molecule and the surface, independently from the long-range order, curvature or ordered arrays of the carbon sheets. Therefore it is terminated that nanostructures with high surface area and micropore density are promising materials for hydrogen adsorption. The different carbon nanostructure specific surface areas according to Panella *et al.* are showed at the Table 1.3.3.4.2.

Table 1.3.3.4.2: Carbon nanomaterials investigated for hydrogen storage and their structural properties

Sample (country)	**BET SSA (m^2/g)**	**Average pore diameter (Å)**	**Pore volume for pores with radius <6.5 Å (cm^3/g)**	**Helium density (g/cm^3)**
Activated carbon I (Canada)	2564	11.75	0.75	2.0
Porous carbon I (Mexico)	1646	11.08	0.46	2.2
Activated carbon II (Germany)	1065	18.23	0.49	2.0
Purified SWCNT I (USA/Germany)	1024	15.37	0.39	2.0
Porous carbon II (Mexico)	946	10.60	0.25	2.1
Purified SWCNT II (USA)	854	17.09	0.36	2.1
Amorphous CNT (China)	369	14.48	0.13	2.2
SWCNTs (Russia)	124	15.52	0.05	1.7
Ros 1 (Cyprus)	34	11.46	0.01	2.1
Ros 3 (Cyprus)	22	11.32	0.0065	2.0

They conclude that among all investigated materials activated carbon with high grade of porosity is the best carbon nanostructure for hydrogen adsorption. It has a fast adsorption and desorption kinetics and the reversibility that is one of the main conditions for successful storage media.

Fullerenes are synthesized carbon molecules usually shaped like a football, such as C_{60} and C_{70}. Fullerenes are able to hydrogenate through the reaction [50]

$$C_{60} + xH_2O + xe^- \Leftrightarrow C_{60}H + xOH^-$$

A spherical cyclic alkene chain of fullerene, C_{60}, contains 30 conjugated double with a variety of closed and open graphene architectures. For the completely hydrogenated fullerene, $C_{60}H_{60}$, the theoretical capacity is 2234 mAh/g with the volumetric capacity of 3820 mAh/cm^3. Theoretical calculations show that the most stable hydrogenated products of C_{60} are $C_{60}H_{24}$, $C_{60}H_{36}$ and $C_{60}H_{48}$. Due to its unique molecular structure, fullerene is the very attractive form of carbon that potentially can be reversibly hydrogenated and de-hydrogenated. The 30 double C-C bonds on each C_{60} sphere could be opened-up to form C-H bonds under certain conditions; theoretical heats of formation for C_{60} and $C_{60}H_{36}$ are 890 and 330 kcal/mole, respectively. Thin film fullerene (C_{60}/C_{70}) electrodes on various substrates have been investigated, and a discharge capacity of about 1600 mAh/g, corresponding to $C_{60}H_{48}$ was measured. This is about four times higher than for any metal hydride. Another advantage of using the fullerene hydride system might be a very fast charging time. Unfortunately, a cycle life of actually fullerene electrodes is rather poor.[77, 78]

Another approach to increase amount of hydrogen sorption reactivity is based on changing the electronic structure of fullerenes by doping with alkali metals as Na, K, Li. Alkali metals give their electrons to fullerenes that causes a charge transfer and results as formation of *fulleride anions* [79].

$C_{60} + n\ e \rightarrow C_{60}^{n-}$, n = 1, 2, 3, 4, 5, 6

Resulting alkali metal-fullerene compounds is reactive with hydrogen under mild conditions without requiring additional catalyst. The experimental results of Loutfy *et al.* of hydrogenation of alkali metal-doped fullerenes are described in the Table 1.3.3.4.3.

Table 1.3.3.4.3 Hydrogen Storage Capacity of Na, K, Li - Doped Fullerenes at 200oC

Starting material	Process parameters		Final product	Wt% hydrogen
	Pressure, psi(MPa)	Time, h		
Na_3C_{60}	600 (~4)	6	$Na_3C_{60}H_{19}$	2,30
Na_3C_{60}	1500 (~10)	6	Na_3C_{60} H_{23}	2,74
Na_3C_{60}	2000 (~14)	6	Na_3C_{60} H_{26}	3,19
Na_3C_{60}	2000 (~14)	24	Na_3C_{60} H_{33}	3,91
Na_6C_{60}	1500 (~10)	24	Na_6C_{60} H_{36}	3,99
K_3C_{60}	600 (~4)	2	K_3C_{60} H_5	0,58
K_3C_{60}	1500 (~10)	2	K_3C_{60} H_{10}	1,10
K_3C_{60}	1500 (~10)	24	K_3C_{60} H_{29}	<3,0
Li_3C_{60}	1500 (~10)	6	Li_3C_{60} H_{10}	1,30
Li_3C_{60}	1500 (~10)	24	Li_3C_{60} H_{24}	<3,0
Li_6C_{60}	600 (~4)	2	Li_6C_{60} $H_{7,5}$	0,95
Li_6C_{60}	1500 (~10)	6	Li_6C_{60} H_{17}	2,17
$Li_{20}C_{60}$	1500 (~10)	24	$Li_{20}C_{60}$ H_{27}	<3,0

Ammonia borane NH_3BH_3, also known as borazane is being studied as a hydrogen-storage compound. There is estimated that roughly 15 wt % of hydrogen can be released from borazene compound either through direct thermal decomposition or by catalytic decomposition of aqueous ammonia borane solutions. As ammonia borane decomposes, the material evolves hydrogen and is converted to polyaminoborane-type compounds and related substances. The reaction also forms borazine, a boron-nitrogen analogue of benzene that can foul fuel cells. Gutowska *et al.* tried to remove borazine from the hydrogen stream by running the reaction in a highly porous silica support. In addition to removing borazine, they found that dispersing ammonia borane in the nanometer-sized pores of silica increased the hydrogen desorption kinetics by a factor of 100 relative to the bulk form of ammonia borane. [80]

Microporous solids like **zeolites** and **metal–organic frameworks** (MOFs) are another class of materials under investigation for hydrogen storage. MOFs are crystalline solids that are compiled by the connection of metal ions or clusters through molecular bridges. They are shoving similar properties to the building blocks as geometric rigidity, chemical functionality, or chirality. The benefit of using molecular bridges is the extension of the length between the metal centres that can organize large cavity regions (fig. 1.3.3.4.3). The components that make up the porous materials can be varied widely, leading to a large class of robust crystalline compounds with potential for high-capacity hydrogen storage [81].

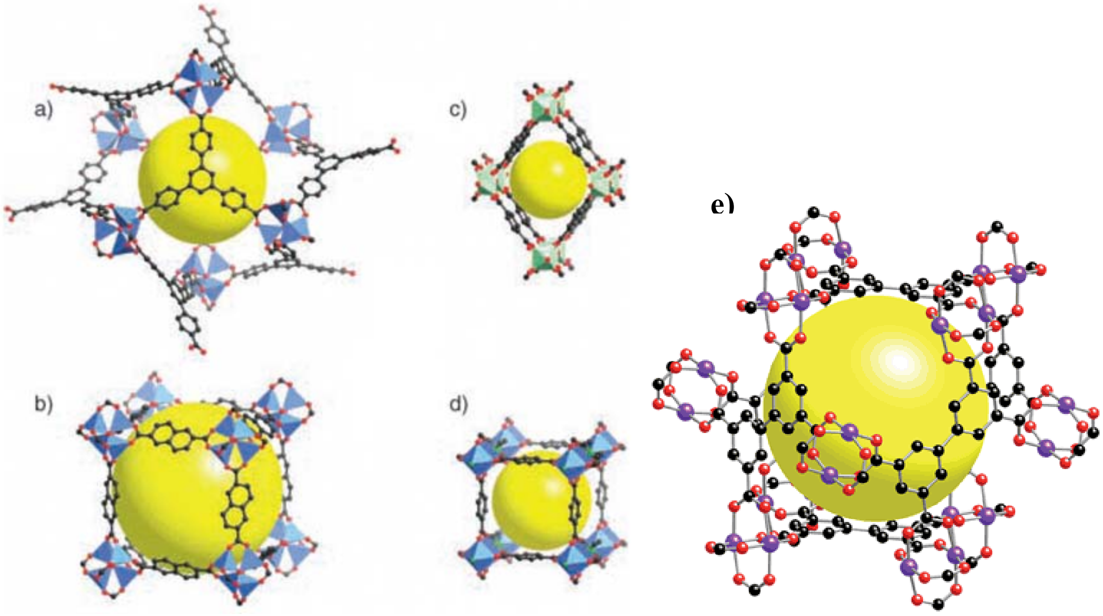

Figure 1.3.3.4.3: Examples of MOFs for hydrogen storage: a) Zn_4O(benzene-1,3,5-tribenzonate)$_2$, b) ZnO_4(naphtalene-2,6-di-carboxylate)$_3$, c) M(OH)(1,4-diazabicyclol) (M=Al^{3+} or Cr^{3+}), d) Zn_2(1,4-diazabicyclo(2,2,2)octane)$_2$, e) $Cu_2(CO_2)_4$ (biphenyltetracarboxylic acid). Pores are illustrated as yellow spheres, C-black, N-green, O-red, Zn – blue polyhedra, M=green actahedra, Cu - violet.

Different MOFs characteristic data have been summarized in Table 1.3.3.4.4.

Used acronyms: bdc=benzene-1,4-dicarboxylate, R^6-bdc=1,2-dihydrocyclobutylbenzene-3,6-dicarboxylate, ndc=naphthalene-2,6-dicarboxylate, hpdc=4,5,9,10-tetrahydropyrene-2,7-dicarboxylate, tmbdc=2,3,5,6-tetramethylbenzene-1,4-dicarboxylate, btb=benzene-1,3,5-tribenzoate, hfipbb=4,4′-hexafluoroisopropylidene) bisbenzoate, cyclam=1,4,8,11-tetraazacyclotetradecane, bpydc=2,2'-bipyridyl-5,5'-dicarboxylate, dabco=1,4-diazabicyclo(2.2.2)octane, bpy=4,4′-bipyridine, btc=benzene-1,3,5-tricarboxylate, 3-pic=3-picoline, pd=1,2-propanediol, L^1=6,6′-dichloro-2,2′-diethoxy-1,1′-binaphthyl-4-4′-dibenzoate, L^2=6,6′-dichloro-2,2′-dibenzyloxy-1,1′-binaphthyl-4,4′-dibenzoate, bptc=biphenyl-3,3′,5,5′-tetracarboxylate.

Table 1.3.3.4.4 Different MOFs characteristic

Material	**Free/fixed diameters (Å)**	**Accessible volume fraction**	**Apparent surface area(m^2 g^{-1})**	**Pore volume (cm^3 g^{-1})**	**H_2 uptake (wt %)**	**Conditions**
$Zn_4O(bdc)_3$	7.8/15.2	0.59	3362	1.19	1.32 1.0 1.65	77 K, 1 atm RT, 20 bar RT, 48 atm
$Zn_4O(R^6\text{-}bdc)_3$	5.9/15.2	0.50	2630	0.93	1.0	RT, 10 bar
$Zn_4O(ndc)_3$	8.4/18.0	0.66	1466	0.52	1.50 2.0	77 K, 1 atm RT, 10 atm
$Zn_4O(hpdc)_3$	6/12.4	0.40	1911	0.68	1.62	77 K, 1 atm
$Zn_4O(tmbdc)_3$	5.4/13.8	0.42	1501	0.53	0.89	77 K, 1 atm
$Zn_4O(btb)_2$	9.6/11.8	0.63	4526	1.61	1.25	77 K, 1 atm
Al(OH)(bdc)	6.4/6.4	0.29	1590, 1020	-	3.8	77 K, 16 bar
Cr(OH)(bdc)	6.6/6.6	0.29	1500, 1026	-	3.1	77 K, 16 bar
$Mn(HCO_2)_2$	3/4.7	0.10	297	-	0.9	77 K, 1 atm
$Cu_2(hfipbb)_2(H_2hfipbb)$	3/4.7	0.03	-	-	1.0	RT, 48 atm
Ni(cyclam)(bpydc)	6.1/7.6	0.18	817	0.37	1.1	77 K, 1 atm
$Zn_2(bdc)_2(dabco)$	7.8/9.5	0.45	1450	-	2.0	77 K, 1 atm
$Ni_2(bpy)_3(NO_3)_4$	2.4/4.0	0.05	-	0.181	0.8	77 K, 1 atm
$Ni_2(bpy)_3(NO_3)_4$	2.1/4.2	0.05	-	0.149	0.7	77 K, 1 atm
$Ni_3(btc)_2(3\text{-}pic)_6(pd)_3$	8.5/10.7	0.30	-	0.63	2.1	77 K, 14 bar
$Zn_4O(L^1)_3$	3.8/7.8	0.21	502	0.20	1.12	RT, 48 atm
$Zn_4O(L^2)_3$	3.8/5.4	0.17	396	0.13	0.98	RT, 48 bar
$Cu_2(pzdc)_2(pyz)$	3.4/5.0	0.04	-	-	0.2	89 K, 1 atm
$Cu_2(bptc)$	6.7/10.1	0.37	1646	0.63	2.48	77 K,1 atm

Zeolites are microporous crystalline solids with well-defined structures. Generally they contain silicon, aluminium and oxygen in their framework and cations, water and/or other molecules. Many occur naturally as minerals others are synthetic, and are made commercially for specific uses. Reversible occlusion of gases in zeolites is a well known phenomenon that includes also hydrogen. The working principle is that under elevated temperatures and pressures the hydrogen molecules are forced into the cavities of the molecular sieve host. Upon cooling to room temperature, hydrogen is trapped inside the cavities. It can be released again by raising the temperature (fig. 1.3.3.4.4). The storage capacity strongly depends on the framework structure and composition of the zeolite[82, 83].

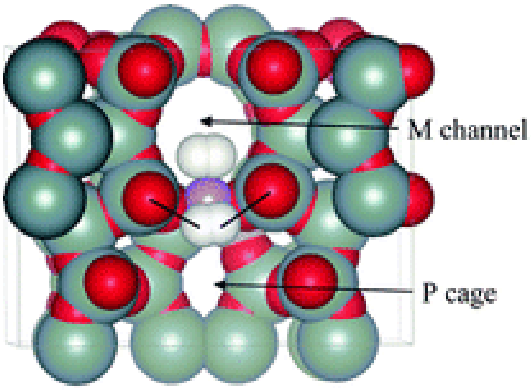

Figure 1.3.3.4.4: Adsorption complexes of two H2 molecules on Li+ cations at the I2/T2 intersection site[84]

In table 1.3.3.4.5 is descripted hydrogen storage capacity in different zeolites[83].

Table 1.3.3.4.5

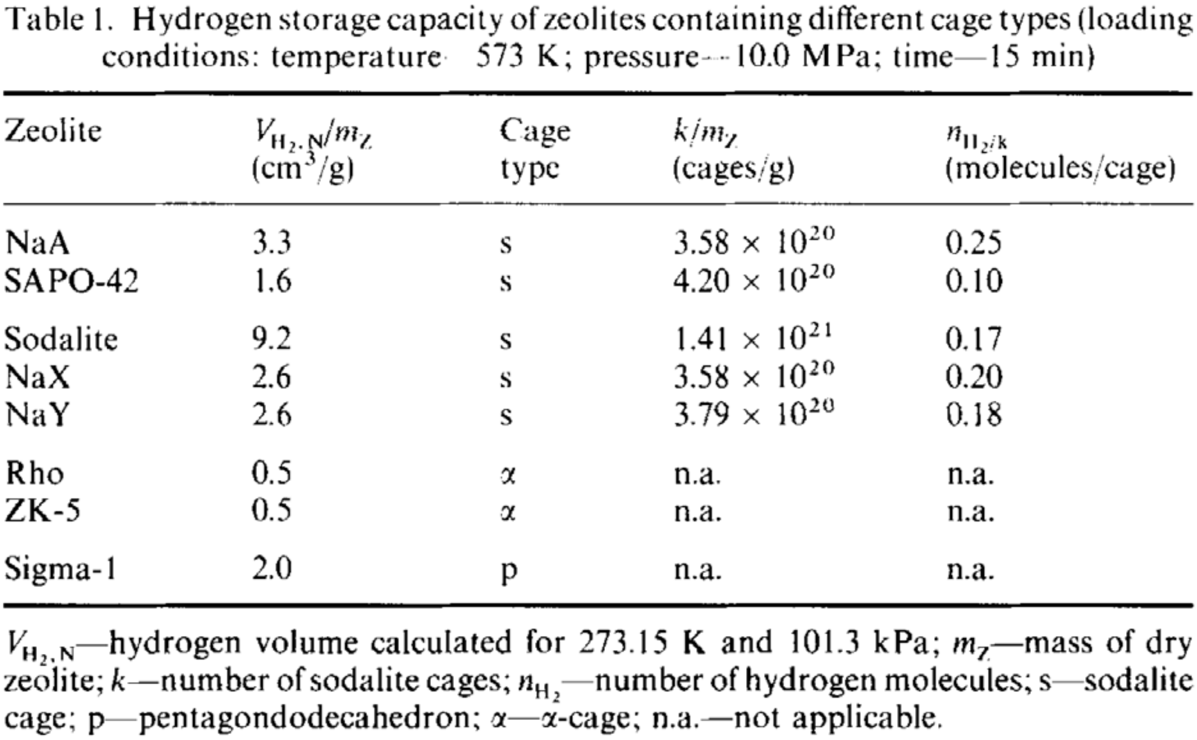

Table 1. Hydrogen storage capacity of zeolites containing different cage types (loading conditions: temperature 573 K; pressure 10.0 MPa; time—15 min)

Zeolite	$V_{H_2,N}/m_Z$ (cm^3/g)	Cage type	k/m_Z (cages/g)	n_{H_2}/k (molecules/cage)
NaA	3.3	s	3.58×10^{20}	0.25
SAPO-42	1.6	s	4.20×10^{20}	0.10
Sodalite	9.2	s	1.41×10^{21}	0.17
NaX	2.6	s	3.58×10^{20}	0.20
NaY	2.6	s	3.79×10^{20}	0.18
Rho	0.5	α	n.a.	n.a.
ZK-5	0.5	α	n.a.	n.a.
Sigma-1	2.0	p	n.a.	n.a.

$V_{H_2,N}$—hydrogen volume calculated for 273.15 K and 101.3 kPa; m_Z—mass of dry zeolite; k—number of sodalite cages; n_{H_2}—number of hydrogen molecules; s—sodalite cage; p—pentagondodecahedron; α—α-cage; n.a.—not applicable.

Figure 1.3.3.4.5 shows an overview of some hydrides comparing with liquid and gaseous hydrogen. There is well noticeable that Mg_2FeH_6 shows the highest known volumetric hydrogen density that is more than double that of liquid hydrogen. $BaReH_9$ has the largest H/M ratio – 4,5 hydrogen atoms per metal atom. $LiBH_4$ exhibits the highest gravimetric hydrogen density of 18 mass%. Pressurized gas storage is shown for steel and a hypothetical composite material.

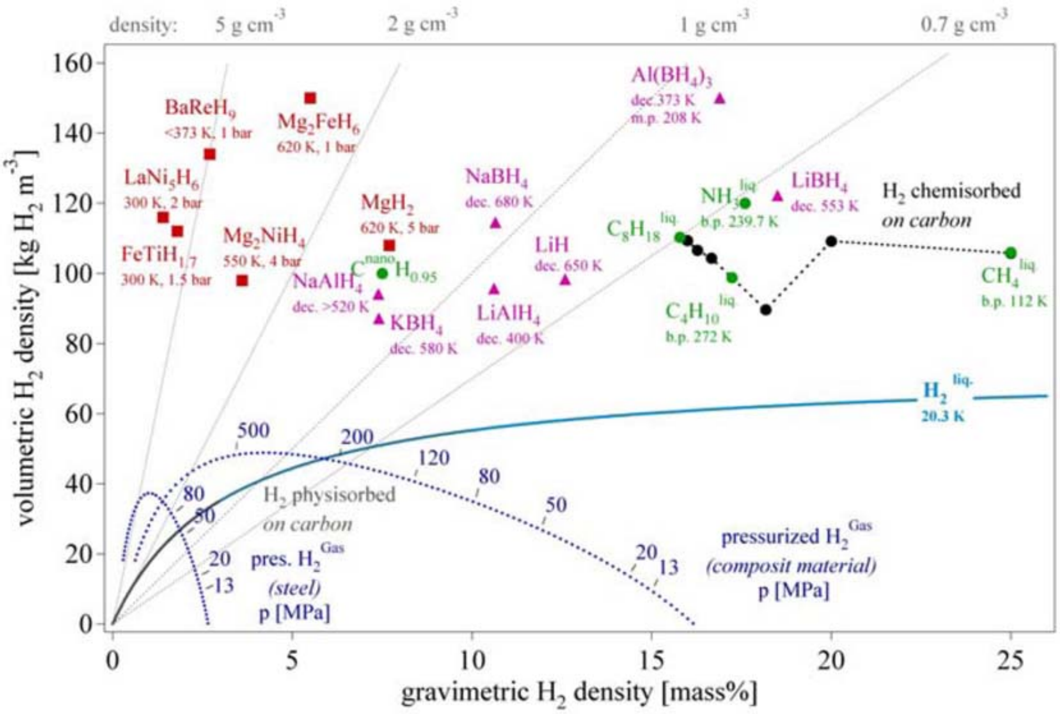

Figure 1.3.3.4.5: Volumetric and gravimetric hydrogen density of some selected hydrides[46].

1.4 Hydrogen spillover

The phenomenon of formation of tungsten bronze from the reduction of tungsten oxide mixed with supported platinum at room temperature was explained by spillover effect in the early 1960s. The fundamental hydrogen spillover models and theories were studied in the next years and the first Conference on Spillover was organized just in 1984. At the end of this conference was postulated but in the second (1989) one scientists made an agreement that a definition of spillover should be following: “Spillover involves the transport of an active species sorbed or formed on a first surface onto another surface that does not under the same conditions sorb or form the active species. Subsequently, the spillover species may diffuse across the accepting surface” [85] Thus, the adsorbed species gain access to a different surface phase (accepting surface) that is in contact with the original adsorbing and activating surface. Diffusion across the first surface may proceed spillover and several processes may take place on the accepting surface following spillover: surface diffusion or transport, diffusion or reaction in the bulk, reactions on or with the surface, and creation of sites capable of adsorption or catalysis (fig. 1.4.1).

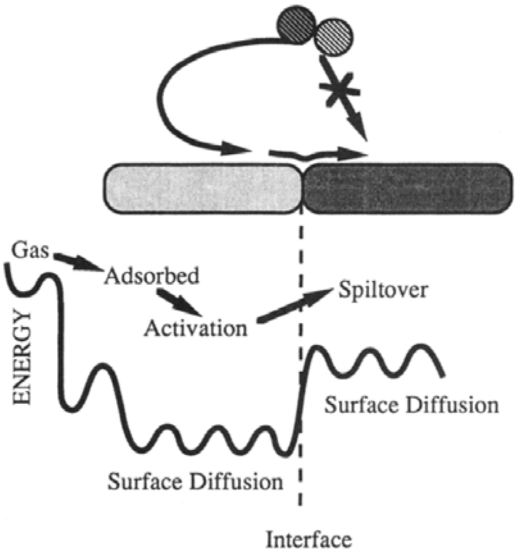

Figure 1.4.1: Schematic representation of spillover of a gaseous diatomic from an adsorbing onto a non-adsorbing surface. A reasonable energy level diagram for the processes is shown [86]

During the following years different kind of experiments and investigations were performed to establish theory and made a modelling of spillover processes. Though, the mechanism of transport of hydrogen spillover is still poorly understood and quite little is known about the nature of the activated H_2 and what is known is somewhat contradictory.

Levy et al [87] considers that chemisorbed hydrogen loses its electron to the conduction band of the metal and the required energy for breaking the bond between the metal and the chemisorbed hydrogen atom is compensated by the formation of a solvated proton. The co-catalyst acts as proton acceptor and the transported species is the solvated proton.

The mechanisms for solid-gas system proposed by Keren and Soffer [88] is that molecular hydrogen is dissociated to electrons and protons based on the observed electronic or ionic surface conductivity. These species migrate through the solid conduction band and the surface hydroxyl groups, to chemisorption sites much farther from the palladium particles.

Fleisch and Abermann [89] presumes that it is highly unlikely that the reactive hydrogen species migrate as a proton via a co-catalyst. They believe that the chemisorbed hydrogen atoms diffuse directly from the Pt film to the substrate.

The more recent in situ studies of proton NMR by Lenz et al describes that in spillover process hydrogen acts like a radical atom that interacting with the surface hydroxyl groups and adsorption peaks that are associated with spillover-induced active sites were observed. Thereby they concluded that if the active species is radical-like, then due to the high electron density at active sites they nature is metallic, anionic, or basic [90].

Conner and Falconer [86] presents a brilliant overview about spillover in heterogeneous catalysis. The mentioned data shows that diffusion coefficient on the Pt surfaces was in the order 10^{-6} cm^2/s but for Ru it varied between 10^{-6} and 10^{-7} cm^2/s depending on the temperature and contact of particles. The table 1.4.1 gives a short summary about the hydrogen diffusion coefficients on the oxide surface.

Table 1.4.1: Hydroge diffusion coefficients on oxide surfaces [86]

Accepting surface	Diffusion coefficient, cm^2/s	Temperature, K
WO_3 to make H_xWO_3	$7 \cdot 10^{-6}$	300
Ce-Y zeolite	10^{-10}	413
Y zeolite	10^{-15}	298
Al_2O_3	$9 \cdot 10^{-15}$	673
Exchange with OH on zeolite	10^{-10}	293
	10^{-6}	473
SiO_2 in Pd/SiO_2	$1{,}5 \cdot 10^{-3}$	413
SiO_2 (Pt/SiO_2 source)	$10^{-4} – 10^{-5}$	473

To understand mean of diffusion coefficient in Conner and Falconer work a sample is presented. The adsorbed species with diffusion coefficient 10^{-6} can reach an area around $10^{-6} cm^2$ in 1 second, thus the diffusing species could come in contact with approximately 10^9 surface atoms or 10^7 active sites.

The concentration of active sites created by spillover is experimentally defined in the work of Cevallos Candau et al by FTIR analysis and reaches 1012on square centimetre on SiO2 [91]. There was concluded that the mechanism of migration is directly coupled to the presence and concentration of OH groups on the surface of silica.

The most recent studies of Lachawiec et al[92] and Li at al[93] showed that hydrogen spillover phenomena can be used to explain the enhanced hydrogen storage in nanostructured carbons and metal-organic frameworks, respectively. They specify that the creation of physical “bridges” has been crucially important for spillover from the dissociation sites on metals to the substrate. Lachawiec et al describes two processes. Primary spillover where the atomic hydrogen is transported from the metal particle to the support and secondary spillover where the transport to the receptor is proceed. Figure 1.4.2 depicts the spillover process in a supported catalyst system.

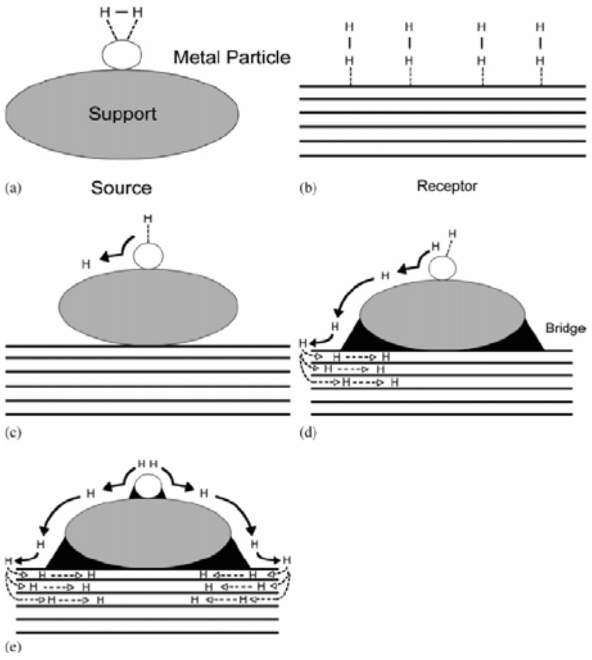

Figure 1.4.2: Hydrogen spillover in a supported catalyst system: (a) adsorption of hydrogen on a supported metal particle; (b) the low-capacity receptor; (c) primary spillover of atomic hydrogen to the support; (d) secondary spillover to the receptor enhanced by a physical bridge; (e) primary and secondary spillover enhancement by improved contacts and bridges [92]

Sermon and Bond [94] describes the ratio of chemisorbed hydrogen atoms to metal atoms by equation:

$$\frac{n_H}{n_M} = \frac{n_H}{n_{M(s)}} \cdot \frac{n_{M(s)}}{n_M} ,$$

where n_H is the number of chemisorbed hydrogen atoms, n_M is the total number of metal atoms and $n_{M(s)}$ is the number of surface metal atoms. The experimental data from different authors for some well-characterized unsupported metals are given in the table 1.4.2.

Table 1.4.2: Values of $n_H/n_{M(s)}$ for various unsupported metals (adapted from[94])

Metal	$n_H/n_{M(s)}$	Temperature, °C	Hydrogen pressure, kPa
Pt	0,9	10	13,33
Pt	0,8	10	13,33
Pt	0,7	<0,2	0,27
Pt	0,9	24	32
Pt	0,6	0,9	1,2
Pt	0,9	5	6,67
Pt	1,0	-	-
Pd	1,0	0,1	0,13
Pd	1,0	0	0
Ru	1,5	10	13,33
Ni	0,9-1,2	10^{-5}	$13{,}33 \cdot 10^{-5}$
Re	0,5	10	13,33
Rh	1,1	0	0

Further, these authors speculated that normally the value $n_H/n_{M(s)}$ has to be equal or less for supported than for unsupported metals. The table 1.4.3 summarizes the values of supported metals. It is shown that these values are higher that is explained by hydrogen spillover phenomena. The particle size impact on adsorption process also is overviewed. According to the transmission electron microscope and x-ray line bordering is concluded that there is not wise to use particles smaller than 20-50 Å.

Table 1.4.3: Maximum values of $n_H/n_{M(s)}$ measured for some supported metals by hydrogen adsorption (adapted from [94])

Metal	Support	Maximum n_H/n_M	Temperature of adsorption, °C	Hydrogen pressure, kPa
Pd	SiO_2	4,0	-196	53,33
Pd	Al_2O_3	5,0	-	-
Pd	Al_2O_3	3,2	25	-
Pt	SiO_2	1,35	20	0,13
Pt	SiO_2	1,5	-196	-
Pt	SiO_2	1,6	-196	$13{,}33 \cdot 10^{-3}; \cdot 10^{-6}$
Pt	Al_2O_3	2,44	250	16
Pt	Al_2O_3	2,19	250	16
Pt	Al_2O_3	2	300	-
Pt	Al_2O_3	1,5	200	1,2
Pt	Al_2O_3	>1	200	1,2
Pt	Al_2O_3	10,0	-	-
Pt	C	75	350	79,99
Pt	Zeolite	1,4	21	-
Pt	Zeolite	2	100	-
Pt	Zeolite	2	200	6,67 – 26,66
Rh	Al_2O_3	1,39	25	0

2. Experimental part

2.1. Sample preparation methods

The next section provides a thorough description of the methodology and materials used in this study.

2.1.1. Material selection

As hydrogen absorber, $LaNi_5$ has been one of the most investigated intermetallic compounds during the last decades. Despite of its high hydrogen capacity - one hydrogen atom to each metal atom - and easy activation, the binary compound is not suitable for applications due to its high plateau pressure and short lifecycle [46]. However, modification of the physical and chemical properties of $LaNi_5$ can be achieved by substituting lanthanum atom with a rare earth metal (e.g. Ce, Pr, Nd, Er) or nickel with a transition metal (Al, Mn, Co, Cr)[26, 95]

Lanthanum nickel alloys (AB_5) with trade names ‘7-10’, ‘DLY-2005’ and ‘17W’ produced by the company Metal Rare Earth Limited of China as well as $LaNi_5$ from “Treibacher”, Austria were used as catalyst and bulk material for hydrogen storage.

A silica based Pyrex glass was applied as material with a large surface for adsorption of spilled atomic hydrogen from AB_5 grain surfaces. According to the previous studies of Kleperis *et al.* [96].

2.1.2. Ball milling

Specific sample preparation methods, such as melt–spinning, sputtering and mechanical milling have been used to improve the hydrogenation kinetics of intermetallic compounds. The resulting alloys exhibit particular structural characteristics as nano-crystalline grain size with a high density of grain boundaries and lack a long-range order that is similar to an amorphous state. These microstructures currently provide fast hydrogenation kinetics and better lifecycle behaviour. Mechanical milling has become a popular technique because of its simplicity, relative inexpensive equipment and applicability to most intermetallic compounds. The mechanical milling has been used for several hydrogen storage alloys; a good improvement in hydrogen activation and kinetics was observed [95, 97].

A ball mill is device that can be used to grind chemicals much more easily and to a finer consistency than can possibly be done by hand with a mortar and pestle. It is often useful to grind chemicals in order to increase their surface area. This will generally increase the rate at which they react in a pyrotechnic composition and make mixtures more homogenous which results in a steady burn rate. For making good quality black powder at home a ball mill is essential, and black powder is needed in very many pyrotechnic devices. Ball milling inevitably causes friction and shocks and possibly leads to static electricity build-up as well depending on the design. Ball milling of mixtures should only be attempted when an appropriate place is available to operate the mill (ie one where it causes no damage or injury in case of explosion) and it must be turned on and off remotely. Most chemicals can be milled more safely but several sets of balls and containers must be available to prevent contamination and milling of metal powders can be dangerous as they may become pyrophoric [98].

RETSCH MM301 mixer mills (Fig. 2.1.2.1) have been specifically developed for dry and wet grinding of small sample quantities. The mixer mills MM 200 and MM 301 work so efficiently that the duration of the grinding process is very short with minimum temperature rise. Thus, most materials can be ground and mixed without cooling. Temperature-sensitive and elastic materials can be successfully processed by pre-cooling the grinding materials and jar. Agate and ceramic jars should not be cooled excessively, in order to prevent damage during the size reduction process.

Figure 2.1.2.1 RETSCH MM301 mixer mills [98]

The grinding container performs radial vibrations in a horizontal position. Thus, the material is hit alternately from various sides by the grinding balls. The intensity can be set precisely between 3 and 30 vibrations per second. A speed control keeps this value constant during the grinding process. The grinding and mixing time can be digitally preset from 10 seconds up to 99 minutes. In stand-by mode, all parameters are maintained for subsequent trials. With 3 memory functions, different standard settings can be programmed. This guarantees maximum reproducibility for the preparation of samples. Screw-top grinding jars offer the ideal prerequisite for grinding. We used steel and tungsten carbide grinding jars and balls (Fig. 2.1.2.2)

Figure 2.1.2.2. Grinding jars and balls for the RETSCH MM301 mixer mills

According to different articles published in press there was considered to use a ball milling technique to improve hydrogen absorbing/desorbing properties of samples [99-101]. A tungsten – carbide crucibles with 2 balls from the same material and a high energetic ball mill Retsch® MM200 was used. Two regimes of grinding and several weight ratios of constituents were used for composite material preparation: the first of 80 minutes at 15 Hz and the second of 30 minutes at frequency 25 Hz (Table 2.1.2.1).

Table 2.1.2.1 Composition of the composite samples used in this work.

C1	Glass + Alloy 7-10 (19:1, weight parts)
C2	Glass + Alloy 7-10 (9:1, weight parts)
C3	Glass + Alloy 7-10 (4:1, weight parts)
C4	Glass+ Alloy 7-10+Nipowder (4.2:0.4:0.4)
C5	Glass + Alloy 7-10 (1:3.7, weight parts)
C6	Glass + Alloy DLY (1:3.7, weight parts)
C7	Glass + Alloy 17W (1:3.7, weight parts)

For further experiments in the RISØ National Laboratory the alloy 7-10 was chosen due to the sample size and easier activation.

2.1.3. Electrode preparation for electrochemical investigation

Electroless plating is undoubtedly the most important catalytic plating process in use today. The principal reasons for its widespread commercial and industrial use are to be found in the unique properties of the electroless nickel deposits. The chemical and physical properties of an electroless nickel coating depend on its composition, which in turn depends on the formation and operating conditions of the electroless plating bath. Typically, the constituents of an electroless nickel solution are: a source of nickel ions, a reducing agent, suitable complexing agents, stabilizers/inhibitors and energy [102].Catalytic reactions, such as electroless nickel plating, require energy in order to proceed. The energy is supplied in the form of heat. Temperature is a measure of the energy (heat) content of the plating solution. Energy which is added to the plating bath is considered a bath variable like other reactants. The quality of energy required by the system or added to it is one of the most important factors affecting the kinetics and rate of the deposition reaction. The metal and the electron source (the reducing agent) are consumed in the electroless plating reaction and so their concentrations in the bath are continuously decreasing [103].There are no anodes available to maintain a near-constant metal concentration, and no external electron source (rectifier) to keep a constant flow of electrons moving into the system, as in an electrolytic plating process. In order to have a continuous and consistent electroless plating process, the reactants must be replenished. The electroless plating reaction not only yields a nickel alloy; it also generates by-products, which accumulate in the solution. As the concentrations of the by-products increase, their influence on the plating reaction also increases. There are a few variables (components) that influence the deposition reaction, namely, the effect of reactants, temperature on rate, pH etc. The rate of the deposition reaction is dependent on temperature in an exponential manner, and the relationship is independent of the acidity or alkalinity of the solution. As the plating reaction proceeds, the pH of an alkaline solution decreases [102, 103]

Three different nickel substrates were used in our work for electrode preparation: bulk nickel, electroplated Ni foil and porous bulk nickel (Fig. 2.1.3.1). The bulk nickel (Nip, 0,2 mm thick casted nickel plate) and 0,1 mm thick electroplated nickel foil (Ni_{epf}) was purchased from Byelorussian Powder metallurgical institute (Minsk, Byelorussia) [104].Porous bulk nickel (Ni_{por} – 1 mm thick) was non-woven macroporous nickel fabric obtained by chemical and electrochemical nickel plating on non-woven plastic fibre cloth with subsequent annealing.

Palladium plate (0,2 mm thick) was used as reference working electrode for study the hydrogen absorption in samples.

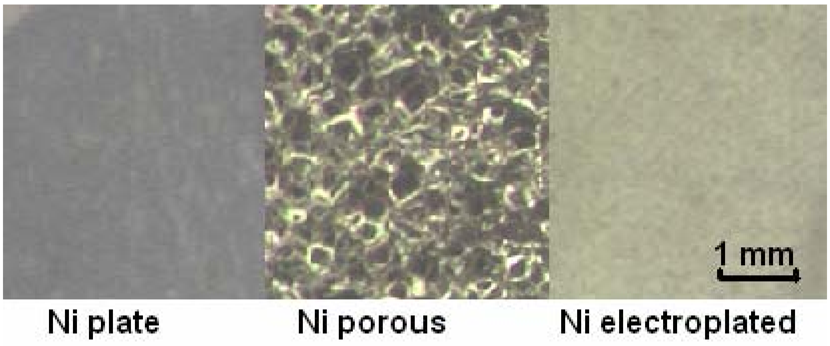

Figure 2.1.3.1 Different nickel substrate materials used as samples: a – starting materials, b – coated with thin Ni film in electroplating process.

Before experiments all nickel samples were etched in 2 M H_2SO_4. Electroplating was performed using modified Watt-type bath with following composition: $NiSO_4.6H_2O$ (300 g/l); $NiCl_2.6H_2O$ (45 g/l); H_3BO_4 (30 g/l). Composite-coating method was used to obtain co-deposited nickel and metal hydride alloy: during nickel plating the particles of AB_5 alloy (40 g/l) was co-deposited on the cathode together with a nickel metal from electrolyte.

The pH of solution was 5.0 - 5.2, temperature of bath 58-60 ^oC and typical currents during plating not above ~30 mA/cm^2. The rate of growth of electroplated nickel was about 0.4 µm per minute, and an amount varied from 10 to 20 µmg/cm^2. Deposition time equal to 5 minutes was chosen for all substrates, and it equal to thickness 2 µm approximately. A commercially available powder of Hydralloy B ($MmNi_5$, AB_5 - type) was added to the bath equipped with a mixer to ensure uniform dispersion during plating (Fig. 2.1.3.2). The Ni^{2+} ion concentration of the bath was kept constant by the dissolution of the nickel anode. As cathode and substrate for an electrode three different nickel substrates were used. Thin palladium film (thickness 1-2 µm) was obtained during electroplating from the bath containing $PdCl_2$ and NH_4Cl.

All electrodes were prepared by cutting equal rectangles 2x1 cm from all samples. Only square 1 cm^2 was left free on the front of sample, all another sample was isolated in an epoxy resin.

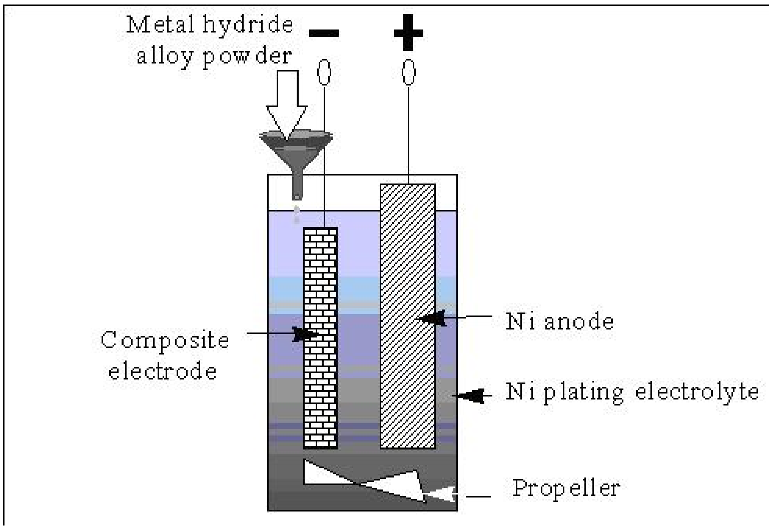

Figure 2.1.3.2. Electrochemical cell to obtain composite nickel electrode for hydrogen adsorption/absorption researches.

Electroless deposition. In our investigation ceramic crucible was activated through the direct immobilization of the palladium catalyst for the subsequent electroless nickel plating. The sensitisation of the ceramic crucible was carried out by directly immersing the polymer in an aqueous solution prepared by dissolving 1g/L $PdCl_2$, 50g/L $SnCl_2.2H_2O$, 170g/L of KCl and 150ml/L of KCL(ρ = 1.19g/ml) in de-ionized water (Tab. 2.1.3.1) and then washed with copious amounts of distilled water. The temperature of the solution was kept between 18 and 25°C.

Table 2.1.3.1: Compositions and characteristics of sensitization and activation bath

Component	**Amount (mg/L)**
$PdCl_2$	1
$SnCl_2.2H_2O$	50
KCl	170
HCl	150 ml/L
Na_2SO_4	60
Temperature (°C)	25
pH	2

The nickel metallization was carried out via the electro- and electroless plating. The surface-activated membranes were immersed in Ni electroless plating bath at a temperature of between 20 – 30°C for 5 – 30min. The basic bath composition and the plating conditions are listed in Table 2.1.3.2

Table 2.1.3.2: Composition of nickel electroless bath and plating conditions

Component	Amount
$NiCl_2 - 6H_2O$	25 g/L
NH_4Cl	27 g/L
$NaH_2PO_2 - H_2O$	37 g/L
NH_4OH	35 ml/L
$NaNO_2$	0.05 g/L
pH	10
Bath temperature	20 – 30°C
Time	5 – 30 min

2.2. Morphological and structural analysis

Many efforts are made to measure physical properties of micro and nano size powders for hydrogen storage [105]. A detailed study of the dependency of the morphology and composition of AB_5 alloys and silica glass composite on the preparation conditions was performed. Characterization methods are restricted to surface techniques. The morphology of the composites was systematically investigated by scanning electron microscopy (SEM). The texture and parameters of an elementary cell of the composite was analyzed by X-ray diffraction (XRD). Active surface area and pore volume was investigate with sorptometer Kelvin 1024.

2.2.1. Scanning electron microscopy (SEM)

Topographic details of a surface can be revealed with great clarity and detail by utilizing the scanning electron microscopy (SEM). Although, with additional equipment can give information about the composition of the sample in an area as small as 1 μm^2. Morphology details of less than 5nm can be resolved by SEM and it possesses a depth of focus more than 500 times higher than that of the optical microscope at equivalent magnification. Typical resolutions for SEM are around 10nm.

The basic design of an SEM is illustrated in Figure 2.2.1.1. The scanning coils, the feature that SEM takes its name from, scan the beam in a grid-like fashion, dwelling on points for a period of time determined by the scan speed. The objective lens then focuses the scanning beam on the part of the sample to be studied. When the electron beam strikes the sample interactions occur, which are detected by various instruments, such as secondary and backscatter electron detectors. Before the beam moves to its next point these instruments count the number of interactions and a pixel is displayed on a monitor whose intensity is proportional to the number of interactions counted. This process is repeated until the grid scan is complete, creating an SEM image.

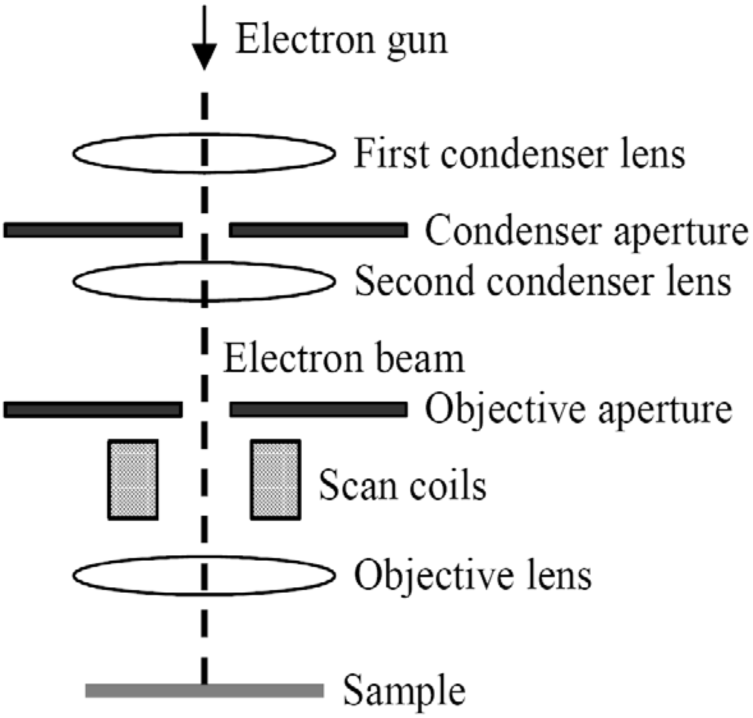

Figure 2.2.1.1 Basic schematic of a typical SEM [38]

For SEM/EDX measurements the Scanning Electron Microscope of Carl Zeiss brand, model EVO 50 XVP located at the Institute of Solid State Physics was used. The SEM images were taken in secondary electrons (SE); the acceleration voltage was equal to 30 kV, and the emission current was between 0,5pA and 500nA (Fig. 2.2.1.2)

The energy dispersive detector for X-rays (EDX) was used for composite determination, gained data (Fig. 2.2.1.3,Tab. 2.2.1.1) shows that the composition of the sample corresponds to formula $A_{0,96}B_{5,04}$ (A=La, Ce, Nd, Pr; B=Ni, Co, Mn, Al, Cr) that is close to AB_5 stoichiometry and the molecular mass of this sample becomes 435,74 g/mol.

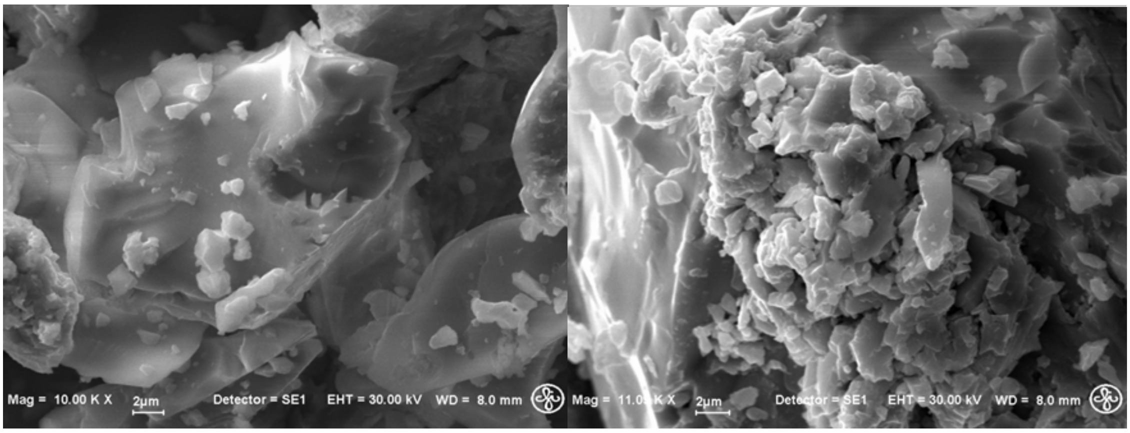

(a) (b)

Figure 2.2.1.2 SEM pictures of alloy 7-10 before (a) and (b) after hydrogenation.

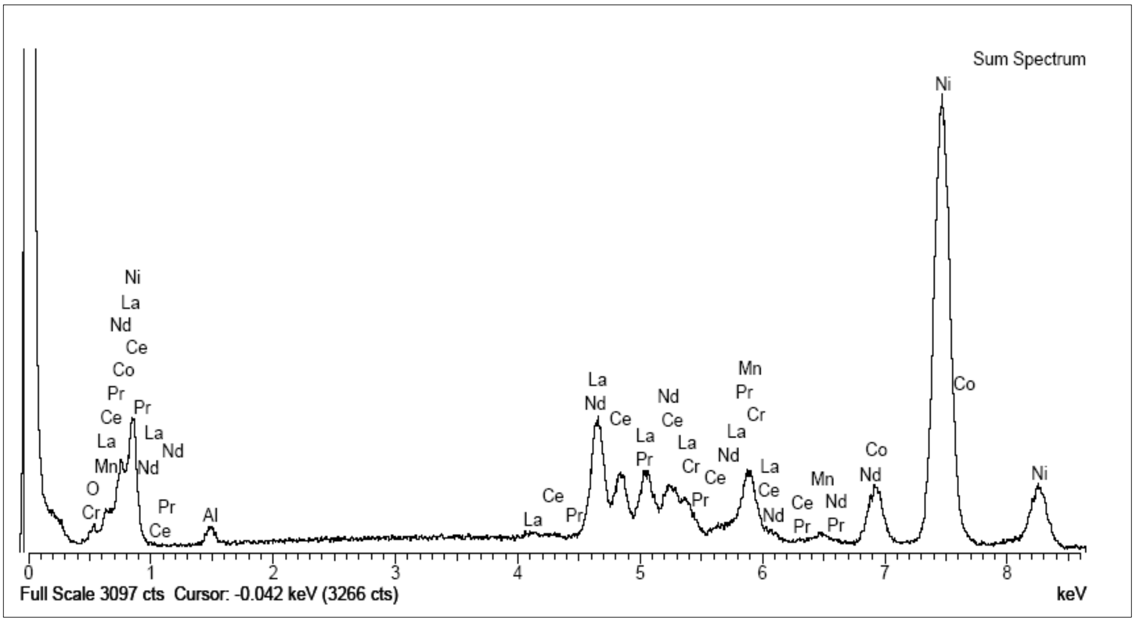

Figure 2.2.1.3 X-Ray disperse energy analysis of sample 7-10

Table 2.2.1.1 Composition of AB$_5$ type alloy 7-10

Element	wt%	Atom %
O	2,03	8,30
AL	1,93	4,67
Cr	0,39	0,49
Mn	5,08	6,05
Co	6,23	6,91
Ni	52,89	58,89
La	17,51	8,24

Ce	9,88	4,61
Pr	0,98	0,45
Nd	3,07	1,39

The oxygen presence in the alloy is nothing unacceptable, anyhow in the further calculations it is assumed that during the high temperature treatment in the hydrogen atmosphere the remaining oxygen is negligible.

The constitution of Pyrex glass used in this work is given in Table 2.2.1.2.

Table 2.1.1.2. Composition of Pyrex glass used as carrier in this work.

Element	Atom number	Proportion
B	5	0.040064
O	8	0.539562
Na	11	0.028191
Al	13	0.011644
Si	14	0.377220
K	19	0.003321

Calculations showed that obtained composition is as follows (in wt%): SiO_2 - 80.5 %; Al_2O_3 – 2.2%; Cl - 0.10%; B_2O_3 – 12.9%; K_2O – 0.4%; MgO – 0.05%; Na_2O – 3.8%; CaO – 0.10%; Fe_2O_3 – 0.04% .

2.2.2. X-Ray diffraction (XRD)

Another structural tool used in this thesis is X-ray diffraction.

The distance separating ions or atoms in a crystal is in the same order of magnitude as wavelength of x-rays (100 pm). The comparable size of the wavelength and inter-species spacing causes a crystal to diffract an x-ray beam passing through it. The crystal diffracts the beam at signature angles depending on the crystal orientation and structure, and x-ray wavelength.

Xray beams are primarily diffracted by the electron density of a crystal, denoted by peak in the recorded XRD pattern. Analysis of the diffracted beams allows the creation of an electron density map of the crystal, from which information about the crystal structure of the material can be deduced[106].

A typical x-ray diffractometer has an x-ray tube to generate x-rays by bombarding a metal target with high energy electrons of 10-100 keV, causing emission of core electrons. An electron from the outer shell then fills the vacant hole in the inner shell and emits an x-ray photon. Molybdenum and copper are common targets, as they both produce strong x-ray emissions at 0.071 and 0.154 pm respectively. The beam created by the x-ray generator strikes the sample and is diffracted and then detected by either photographic film or a movable proportional counter (Figure 2.2.2.1).

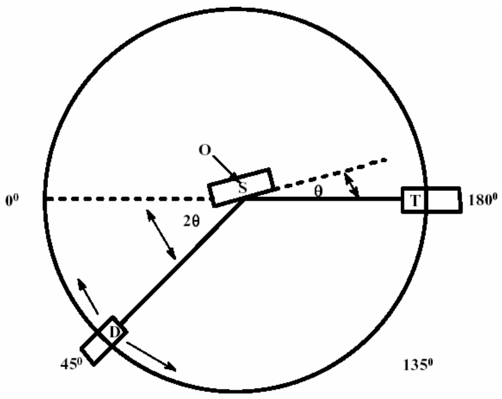

Figure 2.2.2.1: Schematic diagram of an X-ray diffractommetry. T = x-ray source, θ = angle, S = specimen, D = detector and O = axis about which specimen and detector rotate.

The peaks in an x-ray diffraction pattern are directly related to the atomic distances which can be explained using geometry of Bragg's law (Figure 2.2.2.2).

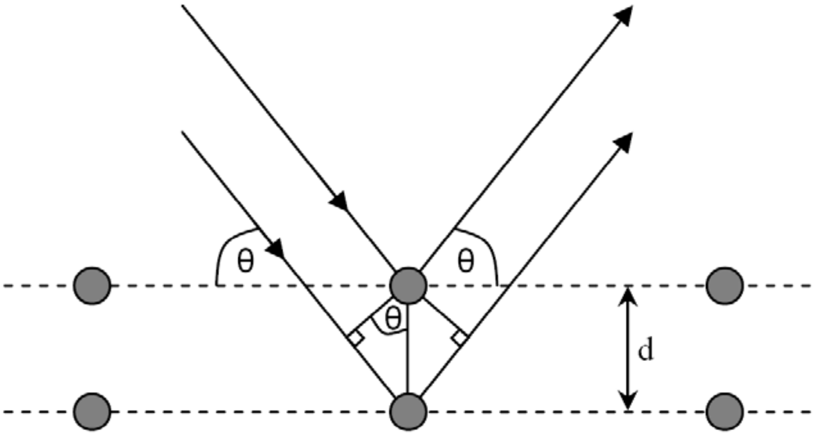

Figure 2.2.2.2 Geometrical representation of Bragg's Law

If parallel lattice planes at a distance *d* are considered, the path length difference for rays reflected from adjacent planes is $2d \sin \theta$, where θ is the angle formed between the plane and the incident beam. If the extra distance the wave has to travel to strike the next row of atoms is an integer value of the wavelength λ of the x-rays, the reflected waves are in phase and constructive interference occurs [38, 107], that can be described by Bragg's law:

$$\mathbf{n\lambda = 2d \sin \theta} \qquad (2.2.2.1)$$

Therefore *d* was measured from the peaks of intensity.

Structural properties of the samples were studied by X-ray Diffractometer System X-STOE Theta/theta, using Kα Cu radiation, and the diffraction patterns were analyzed by appropriate software of STOE system at the RISØ National Laboratory (RNL).

The sample was horizontal while both the detector and X-ray tube moved symmetrically through an angle θ. The X-ray yield is plotted as a function of 2θ. The movement was computer controlled allowing variable scanning speed and digital data acquisition. The standard set up was 0.05° per step and 1 second per step. Figure 2.2.2.3 shows the work file of XRD spectra for glass sample, raw alloy 7-10 and composite material.

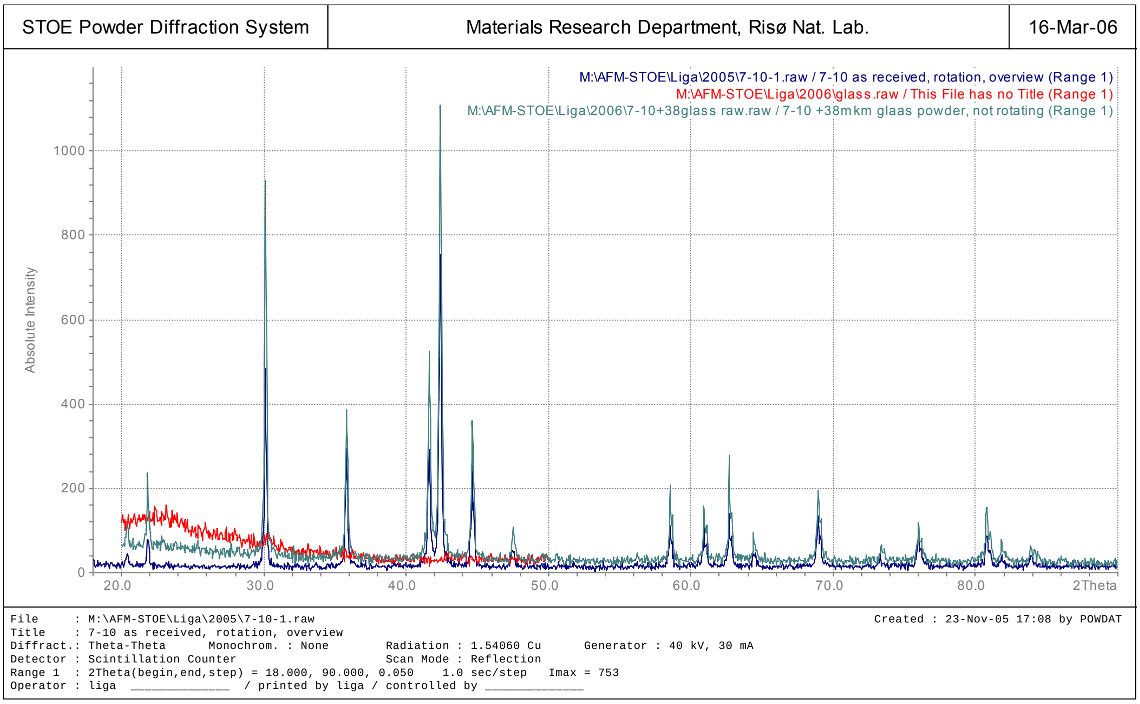

```
File      : M:\AFM-STOE\Liga\2005\7-10-1.raw                                                                    Created : 23-Nov-05 17:08 by POWDAT
Title     : 7-10 as received, rotation, overview
Diffract.: Theta-Theta      Monochrom. : None        Radiation : 1.54060 Cu      Generator : 40 kV, 30 mA
Detector : Scintillation Counter                     Scan Mode : Reflection
Range 1   : 2Theta(begin,end,step) = 18.000, 90.000, 0.050    1.0 sec/step   Imax = 753
Operator : liga  ______________  / printed by liga / controlled by ______________
```

Figure 2.2.2.3 XRD patterns for the raw alloy 7-10(dark blue), Pyrex glass (red) and composite from both (light blue).

XRD pattern shows that they belong to single phase $LaNi_5$ hexagonal $CaCu_5$-type structure in the space group P6/mmm.

2.2.3 BET analysis

The Langmuir adsorption isotherm model is used if the solid surface is uniform and contains a number of equivalent sites, each of which may be occupied by one molecule of adsorbate only and if adsorbate molecules are continually colliding with the surface. If they impact a vacant site they adsorb, if they impact a filled site they are reflected.

The major restriction for the use of the Langmuir adsorption isotherm is that it does not consider the multiple layers of adsorbates that may sometimes form on an adsorbent. This can often lead to an over-estimation of the calculated surface area of the adsorbent. By a number of simplifying assumptions, the BET adsorption isotherm provides a model to multilayer adsorption. That works if the second layer adsorption can only occur on top of the first layer, third on second etc., then the pressure of the system will be equal to the saturated pressure of the adsorbate and when the number of layers is greater than or equal to two, the equilibrium constants and the corresponding values of enthalpy of adsorption and of vaporisation are equal.

The BET isotherm is the most widely used adsorption isotherm model for surface area studies [38, 108]. The used commercial BET machine utilises nitrogen adsorption at -196 °C as a standard method. Isotherms are recorded by the stepwise introduction of known amounts of adsorbate and the recording of the equilibrium pressure; from the isotherm produced both Langmuir and BET calculations may be made.

Gained results showed that the Langmuir and BET active surfaces for a pure alloy 7-10 is more than 3 times less than that for a composite material, however, the pore volume for the composite increased more than 5 times (tab. 2.2.3.1. - 2.2.3.2).

Table 2.2.3.1 Active surface area and pore volume for composite 7-10+glass

BET Surface Area:	0,84	sq.m/g
Langmuir Surface Area:	1,31	sq.m/g
Total pore volume:	2,73	cub.mm/g

Tale 2.2.3.2 Active surface area and pore volume for raw alloy 7-10

BET Surface Area:	0,27	sq.m/g
Langmuir Surface Area:	0,38	sq.m/g
Total pore volume:	0,50	cub.mm/g

2.3. Electrochemical characterisation

Electrochemical methods cover a wide range of analytical techniques. The fundamental signal measured is electrical in nature, either current (Faradaic) or voltage (Potentiometric), resulting from redox reactions. Like other analytical techniques, electrochemical methods yield both quantitative and qualitative information. In addition, some electrochemical methods, will give information about non-redox chemical processes occurring before or after redox reaction.

Charge transfer can occur homogeneously in solutions or heterogeneously on electrode surfaces. For a heterogeneous reaction, the electrode acts as either a source (for reduction) or a sink (for oxidation) of electrons transferred to or from species in solution. Because this is a surface phenomenon, the electroactive species in the solution needs to get to the electrode surface. Therefore, in a still solution, the concentration of species at the electrode surface depends on the mass transport of these species from bulk solution. If the kinetics of the electrode reaction is much faster than this transport the reaction is reversible [109, 110].

Standard electrode potentials, E^0, are measured relative to hydrogen. The standard potential is defined for a cell in which all activities are unity. The formal potential is the reduction potential that applies under specific conditions. Cyclic voltammetry, chronoamperometry are faradaic techniques used in this investigation. The electrochemical methods are extremely useful for the characterisation of nickel structures, as well as being an attractive technique for their electrosynthesis.

Working electrode. Designs of working electrodes (WE) are diverse. Most commonly in experiments to study mechanism and kinetics in the laboratory, the working electrode is a small sphere, disc, or a short wire, but it could also be metal foil, a single crystal of metal, an evaporated thin film, or a powder in the form of pressed disc or pellets [111]. An essential feature is that the electrode should not react chemically with the solvent or solution components. The useful working range is difficult to define as it may be limited by a number of different processes such as oxide formation, hydrogen or oxygen evolution, or solvent decomposition, as well as depending on the reactants and products of the system under study. It is desirable to have an even current and potential distribution and hence for the cell to be designed, so that all points on the working electrode surface are geometrically equivalent with respect to the secondary electrode (Figure 2.3.1).

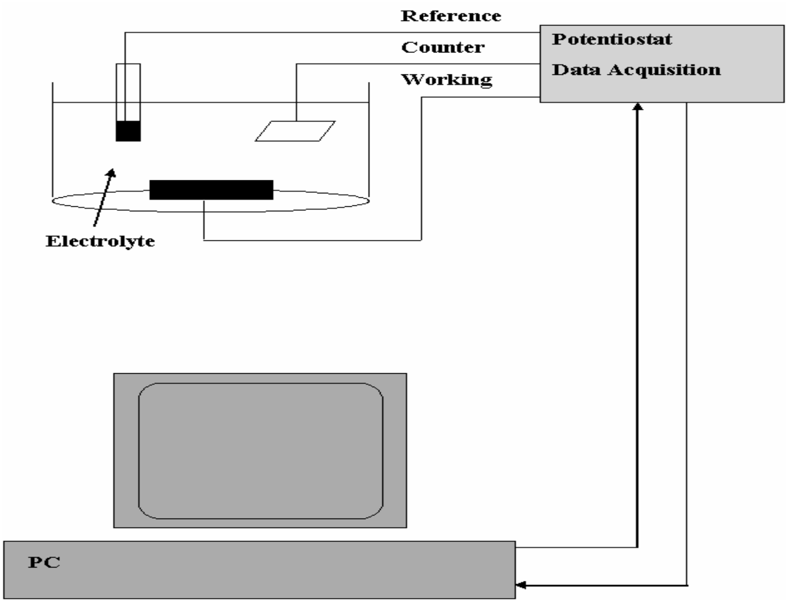

Figure 2.3.1 A schematic diagram of scanning electrochemical microscopy cell and sample holder[112].

Counter electrode. The purpose of the counter electrode (CE) is to supply the current required by the working electrode without limiting the measured response of the cell [110]. It is essential that the electrode process be a decomposition of the electrolyte medium or the oxidation/reduction of a component of the electrolyte, so that the current flows readily without the need for a large overpotential. In some cases, it can be arranged that the counter electrode reaction is a gas evolution or the reverse of the working electrode reaction, so that the composition of the electrolyte is unaltered. The products of the counter electrode reaction should always be considered since they must not interfere with the reaction being studied on the working electrode.

Reference electrode. The role of the reference electrode (RE) is to provide a fixed potential which does not vary during the experiments. It should be independent of current density. In most cases, it will be necessary to relate the potential of RE to other scales, for example to the normal hydrogen electrode, the agreed standard for thermodynamic calculations [110]. In potentiostatic experiments the potential between RE and WE is controlled by a potentiostat, and as the reference half cell is maintained at a fixed potential, any change in applied potential to the cell appears directly across the interface between WE and solution. The RE serves dual purposes of providing a thermodynamic reference and also isolating WE as the system. Thus, a good RE should be able to maintain a constant potential even if a few microamperes are passed through its surface. We used calomel Hg/HgO reference electrode from Radiometric Ltd.

2.3.1. Cyclic Voltammetry (CV)

In conventional cyclic voltammetry a triangular potential waveform is applied to the electrode and the corresponding current is recorded. This technique has been widely applied in the studies of the electrochemistry of solution species and in the study of electrochemical reactions with subsequent chemical reaction steps. Cyclic voltammetry is the most common and perhaps most straightforward electrochemical technique used [113]This technique finds a particular use in preliminary studies of new systems. It also shows the potential range over which the solvent is stable and the degree of reversibility of the electrode reaction. It is also useful for studying electrochemical cell characteristics. It enables independent estimation of oxidation as well as reduction reaction potentials and throws light in their mechanism. Furthermore, within certain limitations, it enables estimations to be made of various parameters such as charge capacity, coulombic efficiency, and reversible potential [110, 114]This involves applying an external triangular voltage to the electrochemical cell, sweeping through a potential range and reversing the direction of the sweep in a cyclic fashion [113](as shown in Figure 2.3.1). The real power of this technique lies in its ability to investigate mechanisms and potentials of electrode reactions.

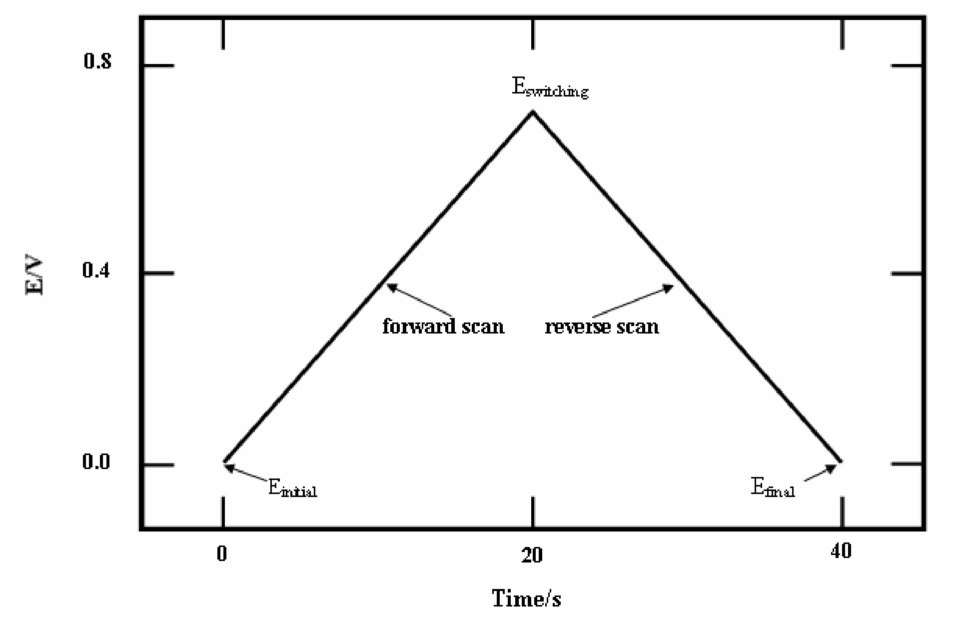

Figure 2.3.1 Waveform excitation signal for cyclic voltammetry.

The potential is increased linearly with time to some specified potential value and then decreased over the same period of time back to the initial potential. The current at E_p can be calculated using the Randles-Sevcik equation (eq. 2.3.1.1),

$$i_p = (2.69\times10^5)n^{3/2}AD^{1/2}v^{1/2}C^* \qquad 2.3.1.1$$

where i_p is the peak current, n is the number of electrons transferred, A is the electrode area, D is the diffusion coefficient of the species, v is the scan rate and C^* is the bulk concentration of the species.

The resulting current (I) is monitored as a function of applied potential (E) to give the I-E curve which in this kind of experiment is called a cyclic voltammogram. Typically a three electrode potentiostated system is used: a working electrode, reference electrode and a counter electrode. The current flows between the working electrode and the counter electrode. The potential is controlled relative the reference electrode which is placed as close to the working electrode as possible to reduce ohmic (IR) potential drop.

However, if the potential is scanned too far in an anodic direction, poorly defined irreversible peaks develop, corresponding to a loss in redox reversibility of the film. Cyclic voltammetry may also be used to show the ability of the film to store charge and to respond to the applied potential. The areas underneath the oxidation and reduction peaks show that approximately equal amounts of charge accompany each process demonstrating the electrochemical reversibility and efficiency of the redox process[113].

Hydrogen electrochemistry was studied by using the method of cyclic volt-ammetry. For working electrode 1 cm^2 was left free and the rest of the sample was isolated with epoxy resin. The simple immersion method was used in all electrochemical measurements using PTFE sample holder. 0.1 M H_2SO_4 water solution was used as an electrolyte in an electrochemical cell supplied with calomel reference electrode and large surface Pd counter electrode. A Potentiostat/Galvanostat VoltaLab of "Radiometer Analytical Ltd" and Ecochemie AutoLab PGSTAT30 was used to record the voltamperic characteristics and polarization curves.

In the University of Western Cape the methodological work of pellet preparation was performed to adapt the sample preparation and measurement technique.

From examined methods the following was considered as the most convenient for preparing 1 pellet: 1 gram of LaMm powder + 5% additives. To form the pellet pressure of 5 tons to square centimeter for 10 minutes was applied. For PTFA and zeolite additions drying in the vacuum oven was performed for 3.5 hours at 150 and 50 ^0C, respectively. For PVA additions the drying at air and 50 ^0C was used. Before measurements all pellets was immersed into 6M KOH for several hours to activate them. In the figure 2.3.1.1, is showed that there are no big differences between all additives.

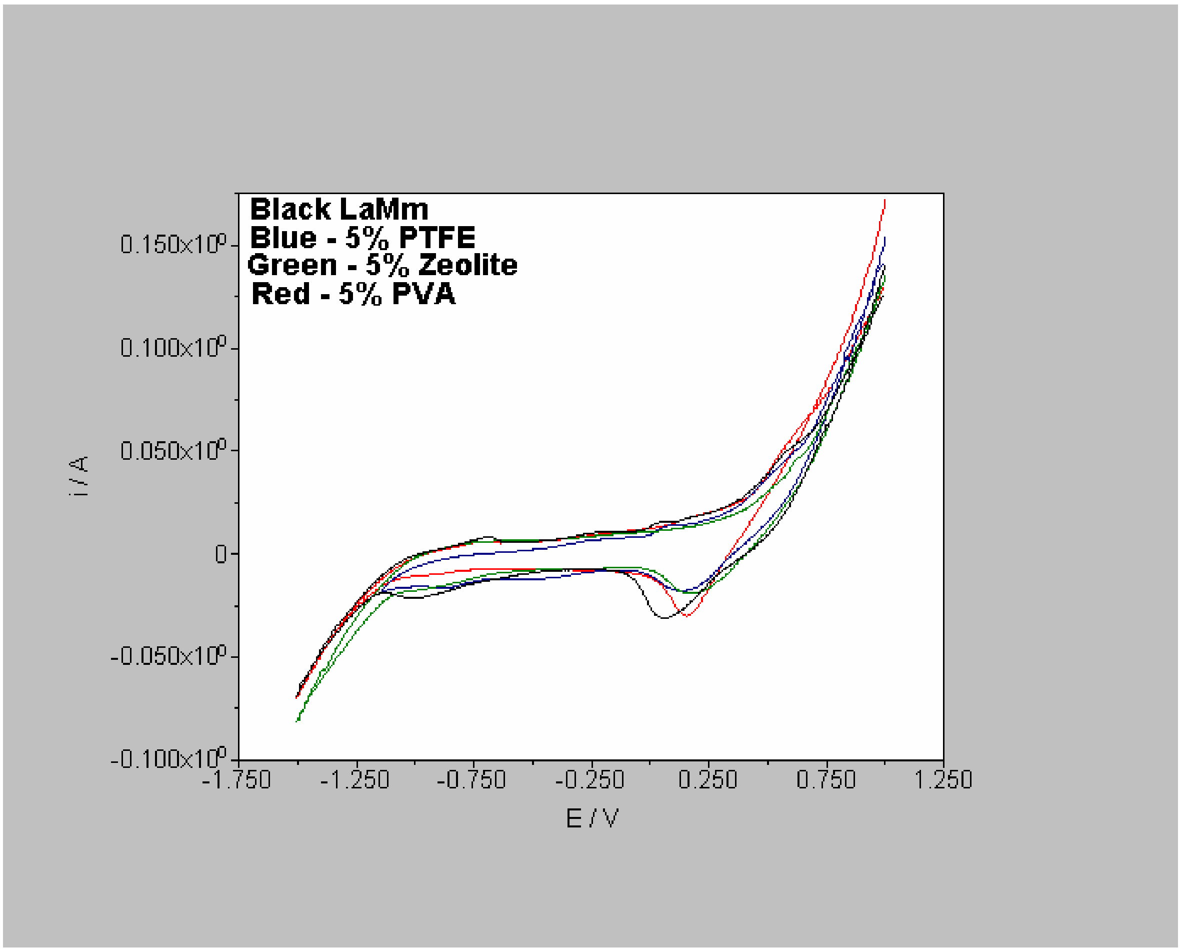

Figure 2.3.1.2 **Volt-ampere curves of pure LaMm sample and with additives**

2.3.2. Electrochemical Impedance Spectroscopy (EIS)

Almost everyone knows about the concept of electrical resistance. It is the ability of a circuit element to resist the flow of electrical current. Ohm's law (Eq 2.3.2.1) defines resistance in terms of the ratio between voltage E and current I.

$$R = \frac{E}{I} \qquad (2.3.2.1)$$

While this is a well known relationship, its use is limited to only one circuit element - the ideal resistor. An ideal resistor has several simplifying properties as it follows Ohm's Law at all current and voltage levels, its resistance value is independent of frequency and AC current and voltage signals though a resistor are in phase with each other.

The real world contains circuit elements that exhibit much more complex behaviour. These elements force us to abandon the simple concept of resistance. In its place we use impedance, which is a more general circuit parameter. Like resistance, impedance is a measure of the ability of a circuit to resist the flow of electrical current[115].

Electrochemical impedance is usually measured by applying an AC potential to an electrochemical cell and measuring the current through the cell. The response to this sinusoidal potential excitation is an AC current signal, containing the excitation frequency and its harmonics. This current signal can be analyzed as a sum of sinusoidal functions (a Fourier series). EIS is normally measured using a small excitation signal. This is done so that the cell's response is pseudo-linear. Linearity is described in more detail in a following section. In a linear (or pseudo-linear) system, the current response to a sinusoidal potential will be a sinusoid at the same frequency but shifted in phase (Figure 2.3.2.1.)

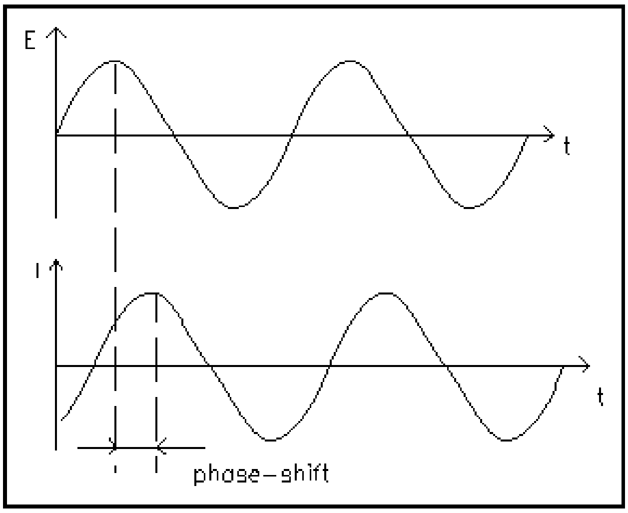

Figure 2.3.2.1: Sinusoidal Current Response in a Linear System

The excitation signal, expressed as a function of time, has the form

$$E(t) = E_0 \cos(\omega t) \quad (2.3.2.2)$$

E(t) is the potential at time t_r E_o is the amplitude of the signal, and w is the radial frequency. The relationship between radial frequency w (expressed in radians/second) and frequency f (expressed in hertz) is:

$$\omega = 2\pi f \quad (2.3.2.3)$$

In a linear system, the response signal, I_t, is shifted in phase () and has a different amplitude, I_0:

$$I(t) = I_0 \cos(\omega t - \phi) \quad (2.3.2.4)$$

An expression analogous to Ohm's Law allows us to calculate the impedance of the system as:

$$Z = \frac{E(t)}{I(t)} = \frac{E_0 \cos(\omega t)}{I_0 \cos(\omega t - \phi)} = Z_0 \frac{\cos(\omega t)}{\cos(\omega t - \phi)} \quad (2.3.2.5)$$

The impedance is therefore expressed in terms of a magnitude, Z_0, and a phase shift, f. If we plot the applied sinusoidal signal on the X-axis of a graph and the sinusoidal response signal I(t) on the Y-axis, an oval is plotted. This oval is known as a "Lissajous figure". Analysis of Lissajous figures on oscilloscope screens was the accepted method of impedance measurement prior to the availability of lock-in amplifiers and frequency [116, 117]. Using Eulers relationship,

$$\exp(j\phi) = \cos\phi + j\sin\phi \quad (2.3.2.6)$$

it is possible to express the impedance as a complex function. The potential is described as,

$$E(t) = E_0 \exp(j\omega t) \quad (2.3.2.7)$$

and the current response as,

$$I(t) = I_0 \exp(j\omega t - j\phi) \quad (2.3.2.8)$$

The impedance is then represented as a complex number,

$$Z = \frac{E}{I} = Z_0 \exp(j\phi) = Z_0(\cos\phi + j\sin\phi) \quad (2.3.2.9)$$

Data presentation. The expression for Z(w) (2.3.2.9) is composed of a real and an imaginary part. If the real part is plotted on the Z axis and the imaginary part on the Y axis of a chart, we get a "Nyquist plot" (Figure 2.3.2.2.) where the y-axis is negative and that each point on plot is the impedance at one frequency.

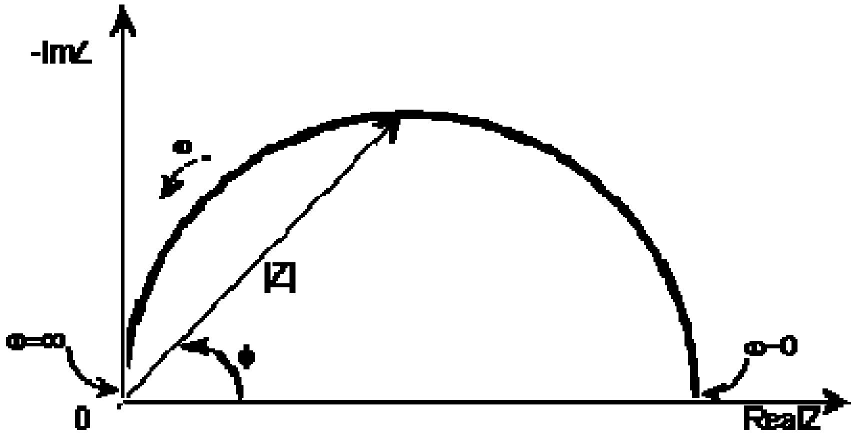

Figure 2.3.2.2 Nyquist Plot with Impedance Vector

On the Nyquist plot the impedance can be represented as a vector of length |Z|. The angle between this vector and the x-axis is f. Nyquist plots have one major shortcoming. When you look at any data point on the plot, you cannot tell what frequency was used to record that point[118].

Electrolyte Resistance. Solution resistance is often a significant factor in the impedance of an electrochemical cell. A modern 3 electrode potentiostat compensates for the solution resistance between the counter and reference electrodes. However, any solution resistance between the reference electrode and the working electrode must be considered when you model your cell. The resistance of an ionic solution depends on the ionic concentration, type of ions, temperature and the geometry of the area in which current is carried. In a bounded area with area A and length l carrying a uniform current the resistance is defined as:

$$R = \rho \frac{l}{A} \quad (2.3.2.10)$$

where r is the solution resistivity. The conductivity of the solution, k , is more commonly used in solution resistance calculations. Its relationship with solution resistance is:

$$R = \frac{1}{\kappa} \cdot \frac{l}{A} \quad \Rightarrow \quad \kappa = \frac{l}{RA} \quad (2.3.2.11)$$

Standard chemical handbooks list k values for specific solutions. For other solutions, you can calculate k from specific ion conductance. The units for k are Siemens per meter (S/m). The Siemens is the reciprocal of the ohm, so 1 S = 1/ohm. Unfortunately, most electrochemical cells do not have uniform current distribution through a definite electrolyte area. The major problem in calculating solution resistance therefore concerns determination of the current flow path and the geometry of the electrolyte that carries the current. A comprehensive discussion of the approaches used to calculate practical resistances from ionic conductance is well beyond the scope of this manual. Fortunately, you don't usually calculate solution resistance from ionic conductance. Instead, it is found when you fit a model to experimental EIS data [117].

Double Layer Capacitance. A electrical double layer exists at the interface between an electrode and its surrounding electrolyte. This double layer is formed as ions from the solution "stick on" the electrode surface. Charges in the electrode are separated from the charges of these ions. The separation is very small, on the order of angstroms. Charges separated by an insulator form a capacitor. On a bare metal immersed in an electrolyte, you can estimate that there will be approximately 30 mF of capacitance for every cm^2 of electrode area. The value of the double layer capacitance depends on many variables including electrode potential, temperature, ionic concentrations, types of ions, oxide layers, electrode roughness, impurity adsorption, etc.[117, 118]

Polarization Resistance. Whenever the potential of an electrode is forced away from it's value at open circuit, that is referred to as polarizing the electrode. When an electrode is polarized, it can cause current to flow via electrochemical reactions that occur at the electrode surface. The amount of current is controlled by the kinetics of the reactions and the diffusion of reactants both towards and away from the electrode. In cells where an electrode undergoes uniform corrosion at open circuit, the open circuit potential is controlled by the equilibrium between two different electrochemical reactions. One of the reactions generates cathodic current and the other anodic current. The open circuit potential ends up at the potential where the cathodic and anodic currents are equal. It is referred to as a mixed potential. The value of the current for either of the reactions is known as the corrosion current. Mixed potential control also occurs in cells where the electrode is not corroding. While this section discusses corrosion reactions, modification of the terminology makes it applicable in non-corrosion cases as well. When there are two simple, kinetically controlled reactions occurring, the potential of the cell is related to the current by the following (known as the Butler-Volmer equation).

$$I = I_{corr}\left(10^{\frac{(E-Eoc)}{\beta a}} - 10^{\frac{-(E-Eoc)}{\beta c}}\right) \qquad (2.3.2.12)$$

Where I is the measured cell current in amps, I_{corr} is the corrosion current in amps, E_{oc} is the open circuit potential in volts, b_a is the anodic Beta coefficient in volts/decade, b_c is the cathodic Beta coefficient in volts/decade.

If we apply a small signal approximation (E-Eoc is small) to equation 2.3.2.12, we get the following:

$$I_{corr} = \frac{\beta_a \beta_c}{2.303(\beta_a + \beta_c)} . (\frac{1}{R_p}) \qquad (2.3.2.13)$$

which introduces a new parameter, R_p, the polarization resistance. As you might guess from its name, the polarization resistance behaves like a resistor[118].

Charge Transfer Resistance [118]. A similar resistance is formed by a single kinetically controlled electrochemical reaction. In this case we do not have a mixed potential, but rather a single reaction at equilibrium. Consider a metal substrate in contact with an electrolyte. The metal molecules can electrolytically dissolve into the electrolyte, according to:

$$Me \Leftrightarrow Me^{n+} + ne^- \quad (2.3.2.14)$$

In the forward reaction in the first equation, electrons enter the metal and metal ions diffuse into the electrolyte. Charge is being transferred. This charge transfer reaction has a certain speed. The speed depends on the kind of reaction, the temperature, the concentration of the reaction products and the potential. The general relation between the potential and the current is:

$$i = i_0 \left[\frac{C_O}{C_O^*} e^{(\frac{\alpha n F \eta}{RT})} - \frac{C_R}{C_R^*} e^{\frac{-(1-\alpha) n F \eta}{RT}} \right] \qquad (2.3.2.15)$$

Where i_o = exchange current density, C_o = concentration of oxidant at the electrode surface, C_o^* = concentration of oxidant in the bulk, C_R = concentration of reductant at the electrode surface, F = Faradays constant, T = temperature, R = gas constant, a = reaction order, n=number of electrons involved, h = overpotential (E - E_0)

The overpotential, h, measures the degree of polarization. It is the electrode potential minus the equilibrium potential for the reaction. When the concentration in the bulk is the same as at the electrode surface, $C_o=C_o^*$ and $C_R=C_R^*$. This simplifies equation 2-18 into:

$$i = i_0\left[e^{\alpha\frac{nF}{RT}\eta} - e^{-(1-\alpha)\frac{nF}{RT}\eta} \right] \qquad (2.3.2.16)$$

This equation is called the Butler-Volmer equation. It is applicable when the polarization depends only on the charge transfer kinetics. Stirring will minimize diffusion effects and keep the assumptions of $C_o=C_o^*$ and $C_R=C_R^*$ valid.

When the overpotential, h, is very small and the electrochemical system is at equilibrium, the expression for the charge transfer resistance changes into:

$$R_{ct} = \frac{RT}{nFi_0} \qquad (2.3.2.17)$$

Diffusion can create impedance known as the Warburg impedance. This impedance depends on the frequency of the potential perturbation. At high frequencies the Warburg impedance is small since diffusing reactants don't have to move very far. At low frequencies the reactants have to diffuse farther, thereby increasing the Warburg impedance. The equation for the "infinite" Warburg impedance is:

$$Z = \sigma(\omega)^{-\frac{1}{2}}(1-j) \qquad (2.3.2.18)$$

On a Nyquist plot the infinite Warburg impedance appears as a diagonal line with a slope of 0.5. On a Bode plot, the Warburg impedance exhibits a phase shift of 45°.

In equation 2.3.2.18, s is the Warburg coefficient defined as:

$$\sigma = \frac{RT}{n^2F^2A\sqrt{2}}\left(\frac{1}{C_O^*\sqrt{D_O}} + \frac{1}{C_R^*\sqrt{D_R}}\right) \qquad (2.3.2.19)$$

In which, w = radial frequency, D_O = diffusion coefficient of the oxidant, D_R = diffusion coefficient of the reductant, A = surface area of the electrode, n = number of electrons transferred, C* = bulk concentration of the diffusing species (moles/cm^3)

This form of the Warburg impedance is only valid if the diffusion layer has an infinite thickness. Quite often this is not the case. If the diffusion layer is bounded, the impedance at lower frequencies no longer obeys the equation above. Instead, we get the form:

$$Z_O = \sigma\omega^{-1/2}\,(1-j)\,\tanh\left(\delta\left(\frac{j\omega}{D}\right)^{1/2}\right) \qquad (2.3.2.20)$$

with, d = Nernst diffusion layer thickness, D = an average value of the diffusion coefficients of the diffusing species[119].

Coating Capacitance. A capacitor is formed when two conducting plates are separated by a non-conducting media, called the dielectric. The value of the capacitance depends on the size of the plates, the distance between the plates and the properties of the dielectric. The relationship is:

$$C = \frac{\varepsilon_0 \varepsilon_r A}{d} \qquad (2.3.2.21)$$

With, e_o = electrical permittivity, e_r = relative electrical permittivity, A = surface of one plate, d = distances between two plates

Whereas the electrical permittivity is a physical constant, the relative electrical permittivity depends on the material [120].

Constant Phase Element. Capacitors in EIS experiments often do not behave ideally. Instead, they act like a constant phase element (CPE) as defined below.

The impedance of a capacitor has the form:

$$Z = A(j\omega)^{-\alpha} \qquad (2.3.2.22)$$

When this equation describes a capacitor, the constant A = 1/C (the inverse of the capacitance) and the exponent a = 1. For a constant phase element, the exponent a is less than one.

The "double layer capacitor" on real cells often behaves like a CPE instead of like like a capacitor. Several theories have been proposed to account for the non-ideal behavior of the double layer but none has been universally accepted. In most cases, you can safely treat a as an empirical constant and not worry about its physical basis[111, 115, 120].

Virtual Inductor. The impedance of an electrochemical cell can also appear to be inductive. Some authors have ascribed inductive behaviour to adsorbed reactants. Both the adsorption process and the electrochemical reaction are potential dependent. The net result of these dependencies can be an inductive phase shift in the cell current . Inductive behaviour can also result from nonhomogeneous current distribution, cell lead inductance and potentiostat non-idealities. In these cases, it represents an error in the EIS measurement[111].

Common Equivalent Circuit Models can be used to interpret simple EIS data. Elements used in the following equivalent circuits are presented in Table 2.3.2.1.and equations for both the admittance and impedance are given for each element.

Table 2-3 Circuit Elements Used in the Models

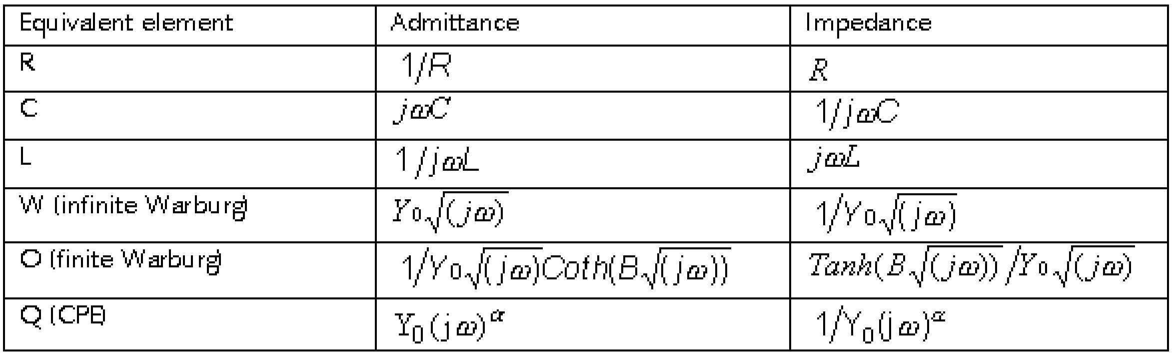

Equivalent element	Admittance	Impedance
R	$1/R$	R
C	$j\omega C$	$1/j\omega C$
L	$1/j\omega L$	$j\omega L$
W (infinite Warburg)	$Y_0\sqrt{(j\omega)}$	$1/Y_0\sqrt{(j\omega)}$
O (finite Warburg)	$1/Y_0\sqrt{(j\omega)}Coth(B\sqrt{(j\omega)})$	$Tanh(B\sqrt{(j\omega)})/Y_0\sqrt{(j\omega)}$
Q (CPE)	$Y_0(j\omega)^{\alpha}$	$1/Y_0(j\omega)^{\alpha}$

Non-linear Least Squares Fitting. Modern EIS analysis uses a computer to find the model parameters that cause the best agreement between a model's impedance spectrum and a measured spectrum. For most EIS data analysis software, a non-linear least squares fitting (NLLS) Levenberg-Marquardt algorithm is used. NLLS starts with initial estimates for all the model's parameters which must be provided by the user. Starting from this initial point, the algorithm makes changes in several or all of the parameter values and evaluates the resulting fit. If the change improves the fit, the new parameter value is accepted. If the change worsens the fit, the old parameter value is retained. Next a different parameter value is changed and the test is repeated. Each trial with new values is called iteration. Iterations continue until the goodness of fit exceeds an acceptance criterion, or until the number of iterations reaches a limit[111, 121].

In the University of Western Cape (UWC) prepared pellets of AB_5 type alloy with different additives (PVA, PTFE, zeolite) were used for electrochemical measurements and equivalent circuit method was used in order to calculate the charge transfer resistances. In the figure 2.3.2.3 it showed how is changing charge transfer resistance according to applied voltage.

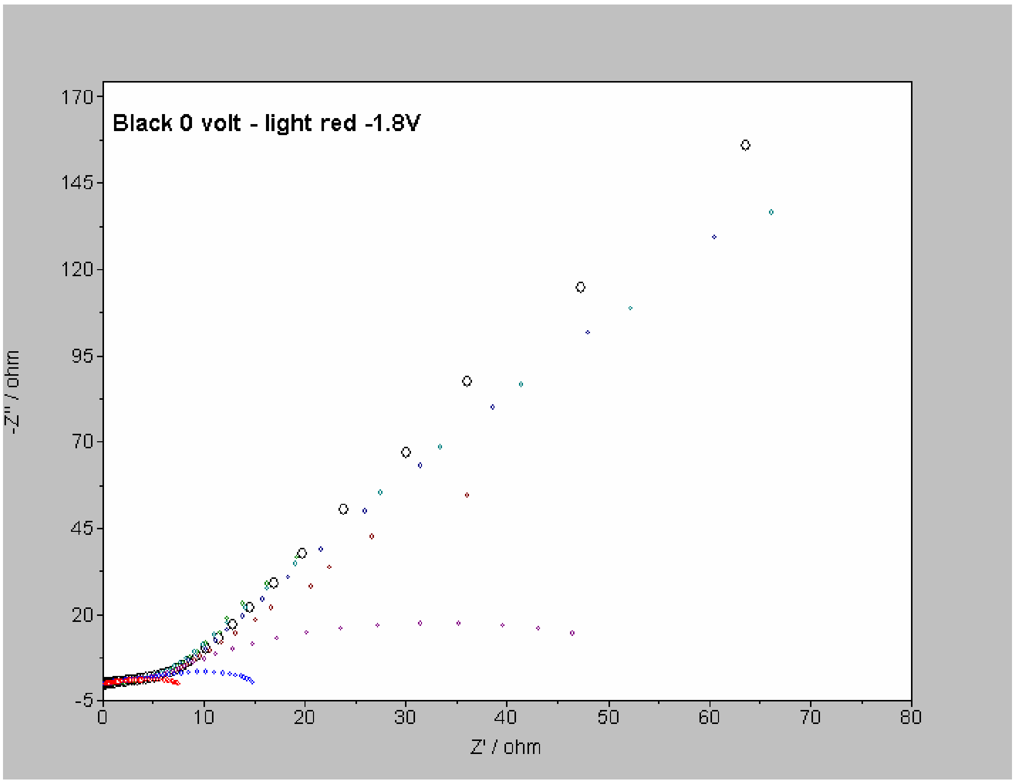

Figure 2.5.2.3 Charge transfer resistance changes dependence of applied voltage.

That is good observable that the charge transfer resistance decreasing with increasing voltage. At the maximum applied voltage the charge transfer resistance decreased from 3945 to 3.86 Ohm. Scheme showed in the figure 2.3.2.4 was used to describe processes what is happening on the Ni electrodes. The first part that consists of two resistances (R1 and R2) and one constant phase element gives the system resistance and but the second semicircle depicts charge transfer resistance. Simulation and fit what is possible with Boukamp software showed that for plain Ni electrodes these scheme (fig. 2.3.2.4) suites enough good (figure 2.3.2.5 - 6).

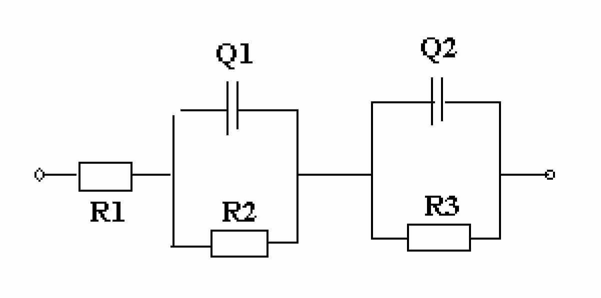

Figure : 2.3.2.5 Equivalent scheme of EIS for Ni electrode

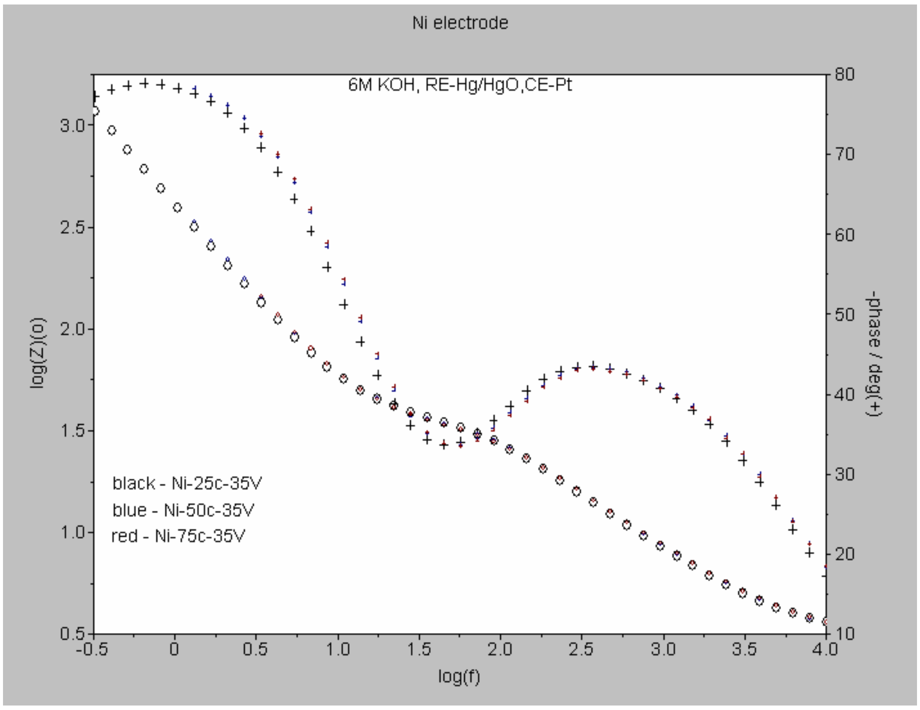

Figure 2.3.2.6 Simulation and fit of Bode plot of Ni electrode.

2.3.3. Charge – Discharge and Chronoamperometry

Chronoamperometry is a potential step method that has a square wave form {[46]6}. A potential is stepped from an initial value that causes no current to flow to a potential that causes current to flow. Because the experiment is diffusion controlled after a certain time almost all molecules that are able to reach the electrode are reduced (oxidised). The resulting current is measured as it decreases over time. The signal follows the Cottrell Equation,

$$i = \frac{nFAD^{1/2}C^*}{\pi^{1/2}t^{1/2}} \qquad (2.3.3.1)$$

Where *i* is the current, *n* number of electrons, *F* is the faradays constant, *A* area of the electrode, *D* diffusion coefficient, *C** concentration and *t* time. This equation can be used to calculate the surface area of an electrode or the concentration of analyte in solution[122, 123].

Charge discharge cycling of commercial metal hydride batteries was performed in RISØ National Laboratory for comparison of electrochemical properties with metal hydride alloy 7-10. Figure 2.3.3.1 shows cycling curves. The charging and discharging was done by changing polarity of the current of 100mA. The cut off potential was kept 1,12 V.

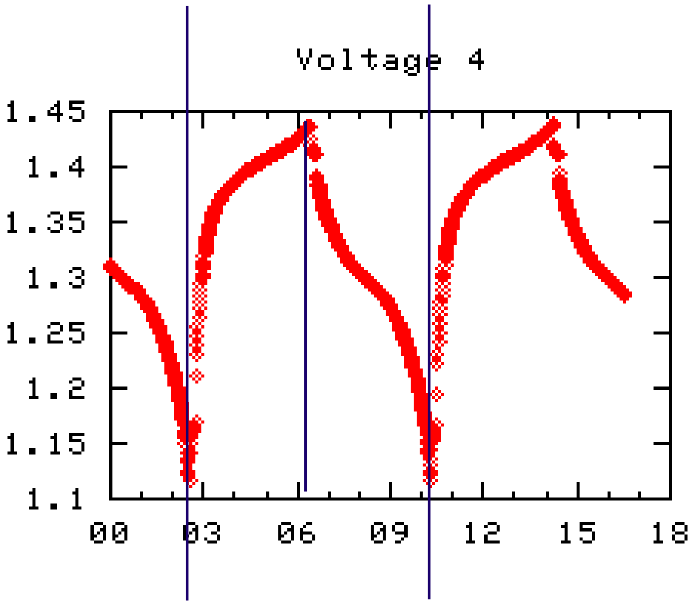

Figure 2.3.3.1 Charge and discharge cycles of commercial MH battery with current ±0,1A

As a current was constant it is possible to use a simplified model for calculations of an ideal curve of battery state of charge.

$$E_{dis}(Q) = E_{Ni,dis}(Q) - E_{MH,dis}(Q) - 0.1 \cdot R \quad (2.3.3.2)$$

$$E_{ch}(Q) = E_{Ni,ch}(Q) - E_{MH,ch}(Q) + 0.1 \cdot R \quad (2.3.3.3),$$

where E_{dis} total are difference between discharge voltage on Ni counter electrode and sum of voltage on MH electrode and inner resistance voltage. E_{ch} total are difference between sum of charge voltage and inner resistance voltage and charge voltage on MH electrode. Difference between charge and discharge voltage gives us a voltage from inner resistance of the electrolyte and electrodes, what in ideal case have to be constant line and sum of both voltages gives us a ideal curve of battery state of charge. If one cycle is reverse then there we are getting two cycles that is plotted of on a graph (figure 2.3.3.2).

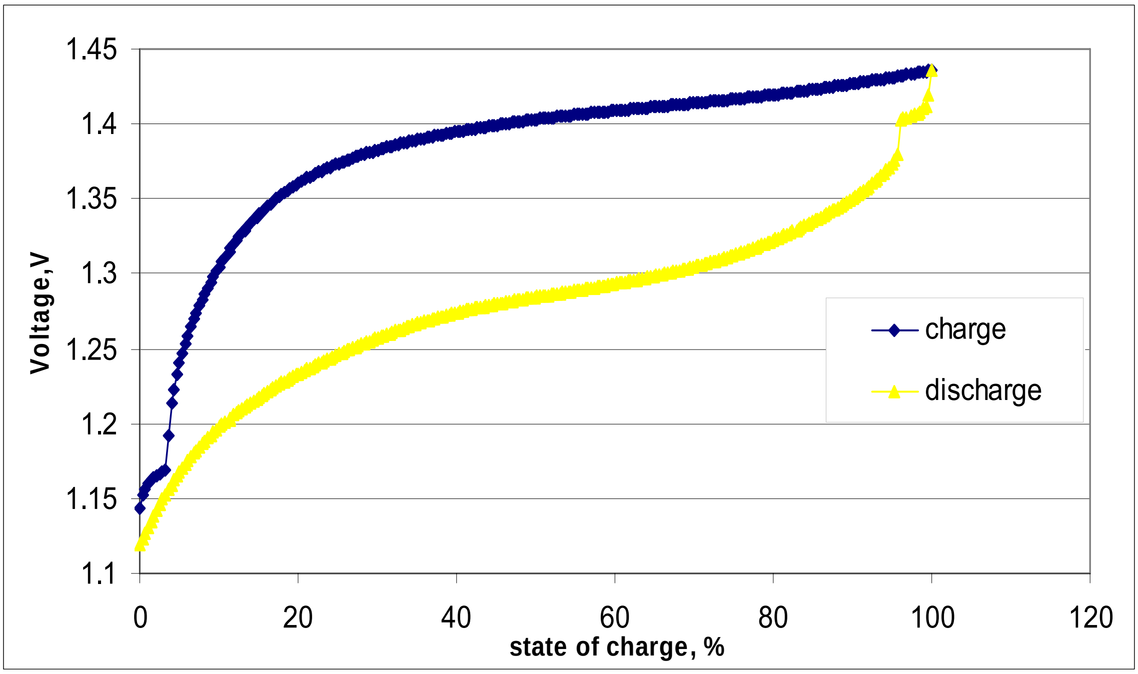

Figure 2.3.3.2: Charge and reverse discharge curve of comercial MH battery

In ideal case the both curves have to fall in one, but there nothing is ideal. Approximating the curves with polynomial equation it is possible to calculate an ideal curve and parasitic voltage given by inner resistance (figure 2.3.3.3)

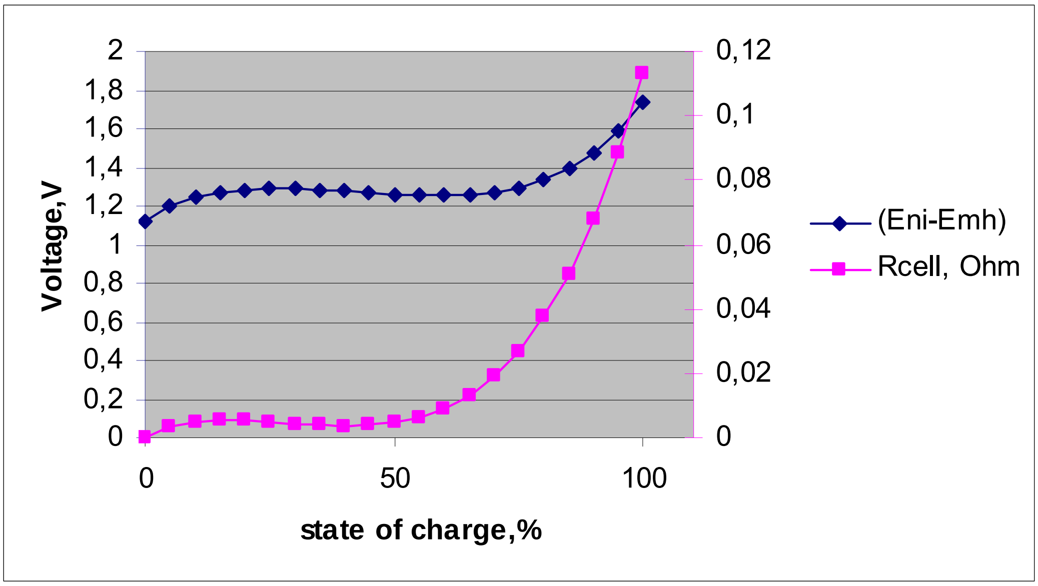

Figure 2.3.3.3 The inner resistance (pink) and ideal voltage curve for MH battery

For electrochemical measurements approximately 100mg of alloy 7-10 and 300mg of Cu powders was mixed together. Pellets was cold pressed under 5 tonnes of pressure on cm^2. Electrolyte was 6M KOH, Ni was used as a counter electrode, but calomel as reference. The discharge cut-off potential was set at -0,6V. Electrodes were cycled with constant current ± 2 mA. Equilibrium potential was measure with pulsed cycle method, i.e. current was applied for 20 min and after a pause the open circuit potential was measured. This procedure was repeated while electrode is fully charged (2.3.3.4).

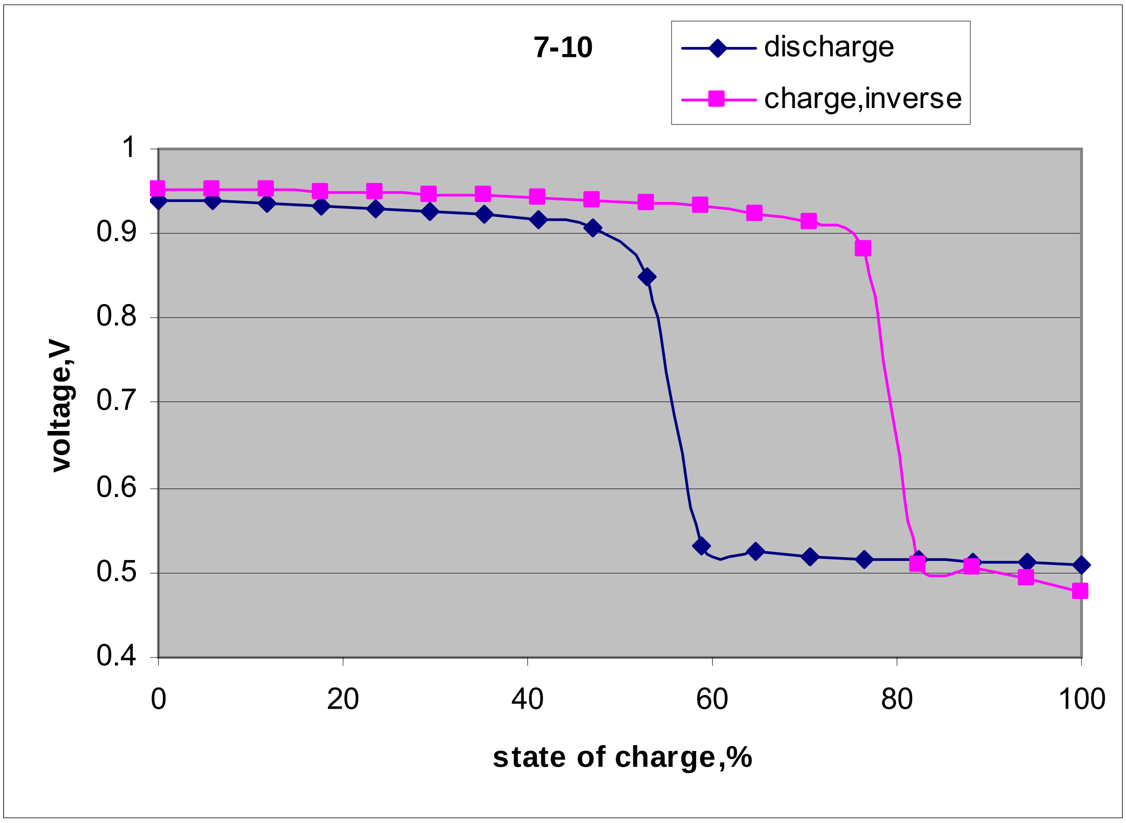

Figure 2.3.3.4 Discharge and reverse charge cycles for alloy 7-10.

2.4. Gravimetric and volumetric hydrogen sorption analysis

A thermogravimetric technique has been used to study the hydrogen sorption on prepared samples. The measurements were performed by equipment based on the Sartorius high pressure balance (HPB) combined with pressure, temperature and gas supplying systems. The sample is placed in the steel container that can be sealed to provide a vacuum or gas atmosphere and the pressure and temperature ranges of $1 \cdot 10^{-3}$ –30 bar and from room temperature to 300°C, respectively.

Experiments were started with sample 7-10 (manufacturer's title) and glass additives. The particle size of metalhydride alloy varied between 2 to 50 µm with maximum amount at 10 µm but for glass phase it varied between 63 to 125 µm.

For experiment crucible with weight w_c=1143.88 mg was chosen and weight of powder was m_{7-10}=340.20mg. The treatment procedure was performed in the following way:

1. Vacuuming the system
2. Rinsing with He up to 15 atm pressure, then lowering pressure to 1,5 atm
3. Heating the system with rate 10 ^{0}C per min up to 250 ^{0}C
4. Vacuuming the system
5. Rinsing with He up to 5 atm, then to 1,5 atm
6. Cooling the system
7. Vacuuming the system
8. Starting measurement at room temperature

In the beginning of measurements the sample was held in vacuum for 22 min, then 0,5 atm for 34 min, 1 atm for 40 min, 5 atm - 1360 min (22h 40min), 10 atm - 306 min (5h 6min), 20 atm – 5800min (96h40min). Such a long period is due to very slow absorption rate and the weight of sample still wasn't stable at the end of measurements (figure 2.4.1)

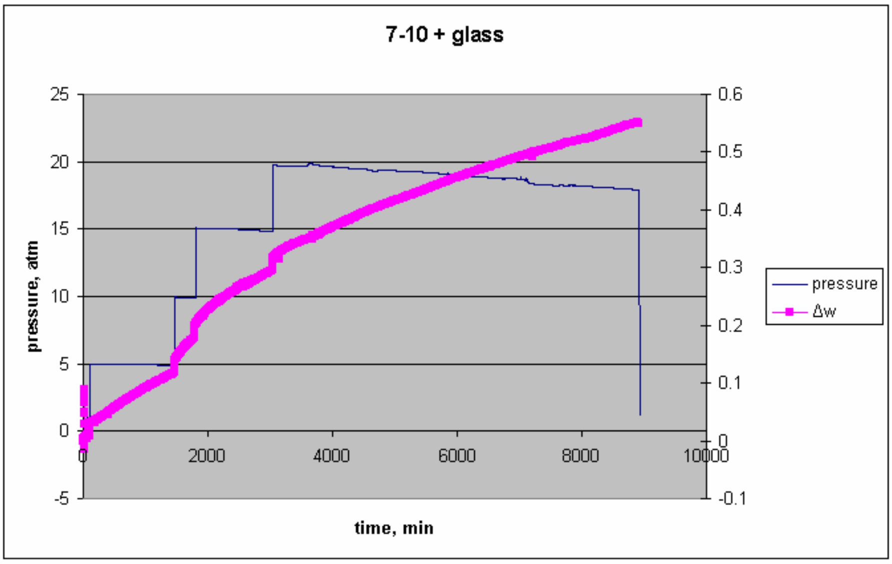

Figure 1: The weight change of composite material at different hydrogen pressures

Comparing to the same metalhydride powder hydrogenation curve the slower kinetics and decrease of absorbed hydrogen amount is observed (figure 2.4.2)

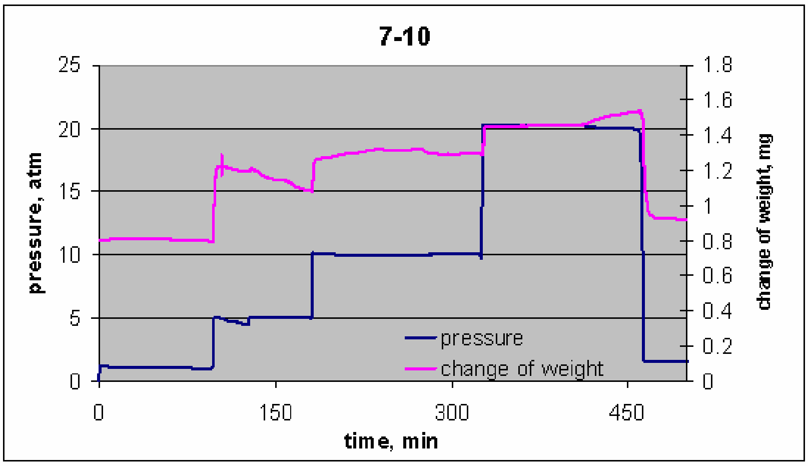

Figure 2.4.2: Change of weight for pure 7-10 alloy

Some calculations to outline amount of absorbed hydrogen is described below.

Mass of raw sample – 340.71mg, mass of sample with glass phase – 340.20mg. Weight ratio in composite 0.7359g of Pyrex and 2.7357g of alloy. Molar mass of alloy $M_{7\text{-}10}$=427.25g/mol; of hydrogen atom M_H=1g/mol.

Weight% of alloy in composite:

$$w\%_{7-10} = \frac{2,7357}{0,7359 + 2,7357} * 100 = 78,8\% \quad (2.4.1)$$

The mass of alloy in composite sample then is calculated as:

$$w_{7-10} = 0,788 \cdot 340,20 \cdot 10^{-3} = 268.08mg \quad (2.4.2)$$

Amount of substance of alloy

$$n_{7-10} = \frac{m_{7-10}}{M_{7-10}} = \frac{268,08mg}{427.25\frac{g}{mol}} = 0,627mmol \quad (2.4.3)$$

If the gain of the weight within hydrogenation is 0,507mg due to absorbed hydrogen atoms then amount of hydrogen in alloy

$$n_H = \frac{0,507mg}{1\frac{g}{mol}} = 0,507mmol \;, \quad (2.4.4)$$

Amount of hydrogen in composition AB_5H_x what was hydrogenated in this experiment is

$$x = \frac{n_H}{n_{7-10}} = \frac{0{,}507\,mmol}{0{,}627\,mmol} = \underline{\underline{0{,}81}}. \qquad (2.4.5)$$

For raw alloy 7-10 the max change of weight 1,5mg was observed

$$x = \frac{n_H}{n_{7-10}} = \frac{1{,}5\,mmol}{0{,}797\,mmol} = \underline{\underline{1{,}88}}. \quad (2.4.6)$$

Following common knowledge that in these compositions amount of hydrogen on one molecule of alloy could be 6 atoms AB_5H_6 then we can predict the max change of weight what could show that alloy is fully hydrogenated.

$\Delta w = M_H \cdot x \cdot n_{7-10} = 1 \cdot 6 \cdot 0{,}797 = 4{,}782\,mg$ For raw sample

$\Delta w = M_H \cdot x \cdot n_{7-10} = 1 \cdot 6 \cdot 0{,}627 = 3{,}762\,mg$ For sample with glass phase

The results are not fitting with gained and conclusion is that sample wasn't completely hydrogenated. That could be caused by not efficient activation process, the system activation cycles of heating and cooling in atmosphere of hydrogen of sample was performed to improve hydrogenation options. After 3 time heating and cooling cycles, the change of weight was close to theoretically possible, thereby improvement of alloy hydrogenation was reached (Figure 2.4.3) and enlarged part of 2nd and 3rd heating/cooling cycles Figure 2.4.4).

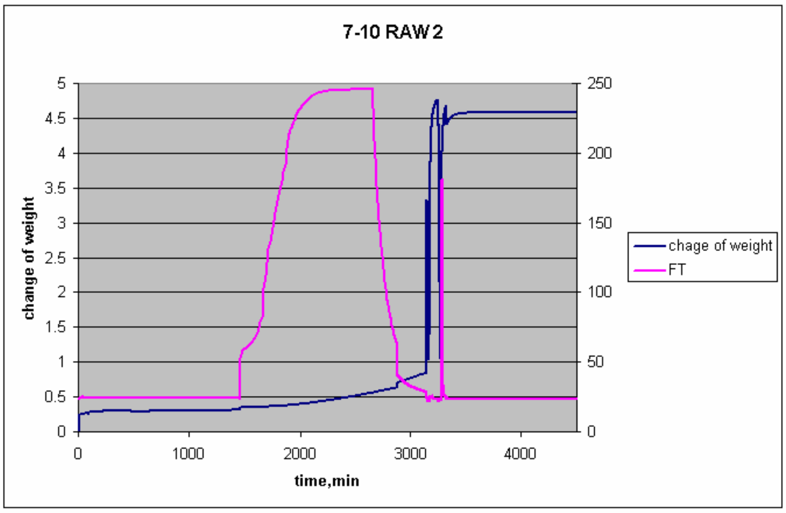

Figure 2.4.3: The difference of weight after system treatment.

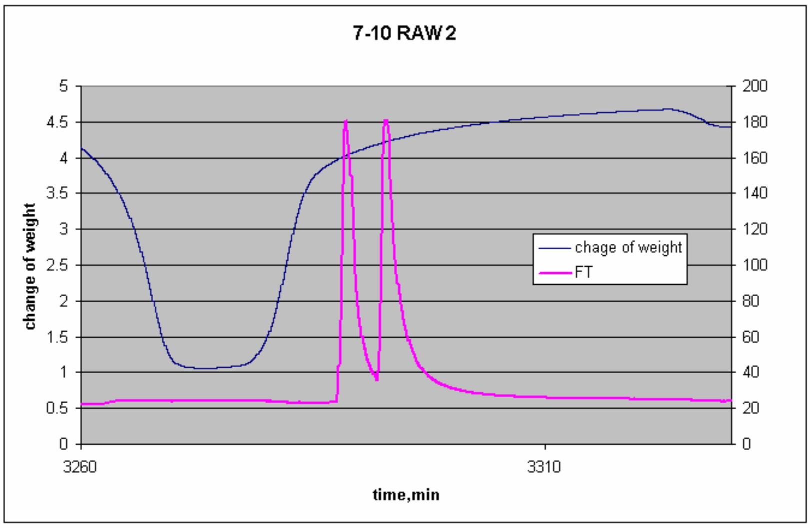

Figure 2.4.4: Enlarged part of 2nd and 3rd cycles.

The same kind of experiments with alloy 7-10 and glass phase with particle size 38μm and smaller were performed to observe any heating/cooling cycle improvement on PCT characteristics of the sample. Figure 2.4.4 shows comparison of the alloys 7-10 and composite materials that had been activated once or three times.

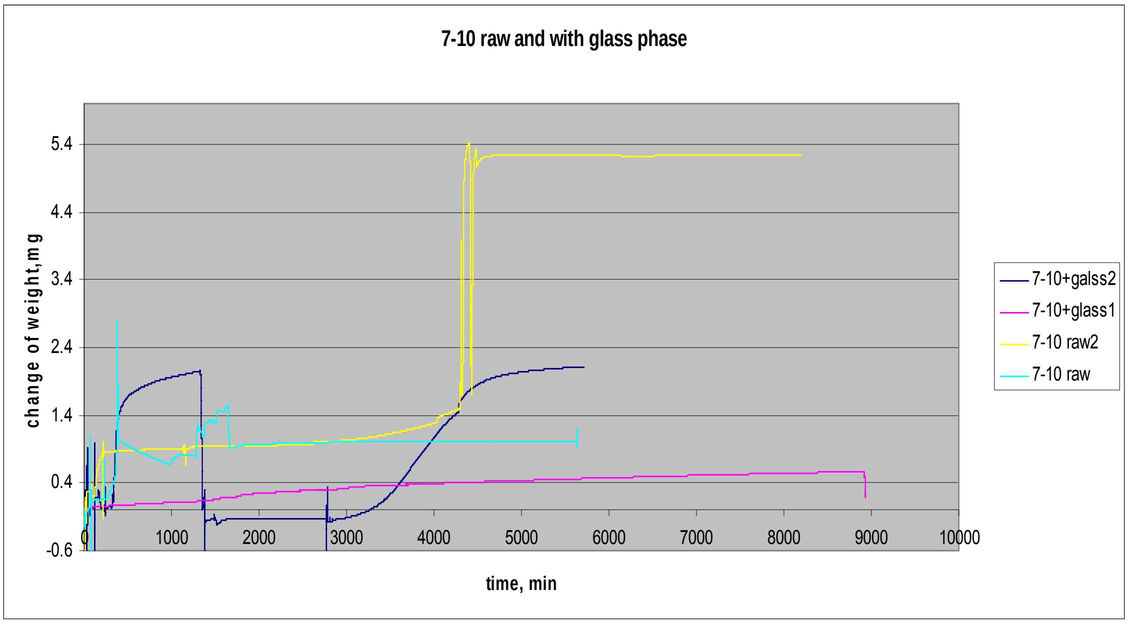

Figure 2.4.4 weight change comparison of alloy 7-10 (light blue) activated once with alloy 7-10 activated 3 times (yellow) and composite activated once (pink) and activated 3 times (dark blue).

Volumetric analysis

During the PhD studies in the Institute of Solid State Physics was constructed autoclave type device that could be used for volumetric investigations of the hydride alloys after the end of the cooperation project with RNL (Figure 2.4.5). It is equipped with pressure sensors ECO-1 from Greisinger Electronic GmbH and a stainless steal container with an internal volume of 36 cm^3. The changes of pressure during hydrogenation of alloys and composites were observed due to the absorption/adsorption and desorption of hydrogen in the sample. It can be used at constant temperatures and at constant pressure in the container.

A method was developed to determine the amount of permanently stored hydrogen in the samples, using an automatic differential thermogravimeter (TG) DTG-60 by Shimadzu Corporation with pressure regulator FC-60A in argon flow 75 ml/min. Measurements started from room temperature to 500 °C. After hydrogenation the samples were transported to the TG instrument through open air. During the open-air transportation it could be possible that there is a loss of stored hydrogen, especially, for composite materials, were not only the surface but also the bulk hydrogen could be lost.

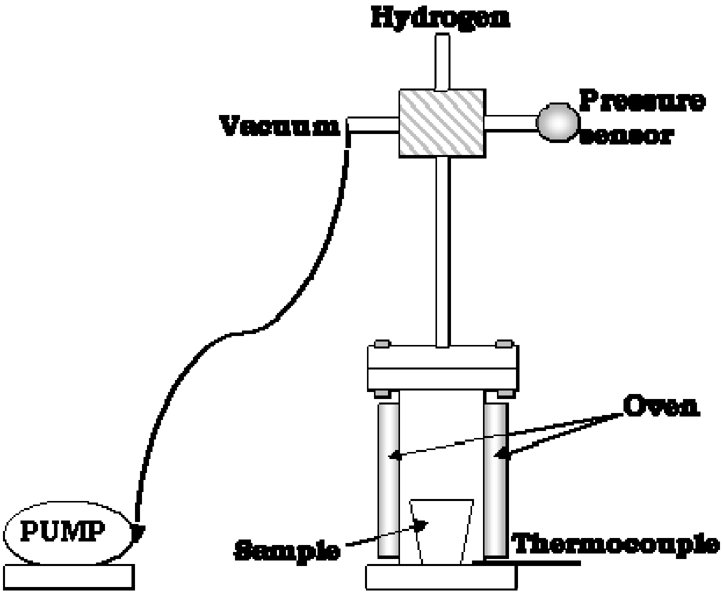

Figure 2.4.5. Self-made equipment for volumetric investigations.

Pressure dependence measurements from temperature of an empty camera of the new device is shown in figure 2.4.6.

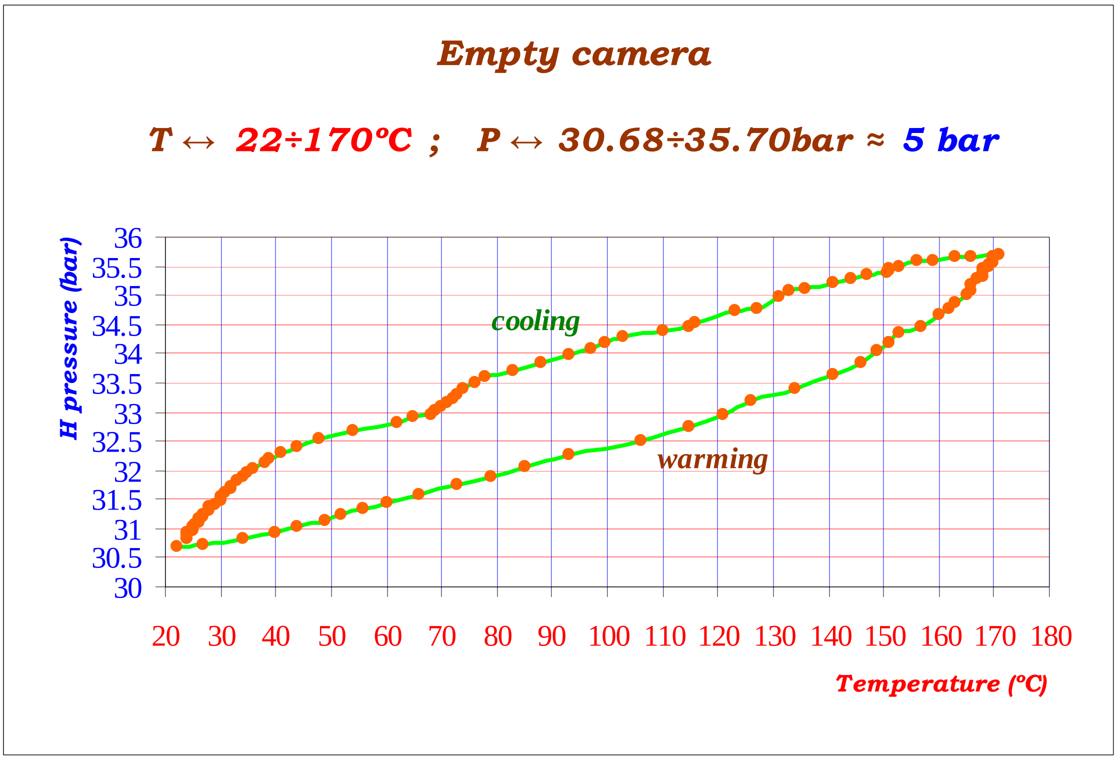

Figure 2.4.6. Pressure dependence from the change of temperature in the empty camera.

The new device was used also for volumetric measurements of the alloy 7-10 (fig. 2.4.7) and composite materials (fig. 2.4.8) as well as for classical alloy $LaNi_5$ (fig. 2.4.9).

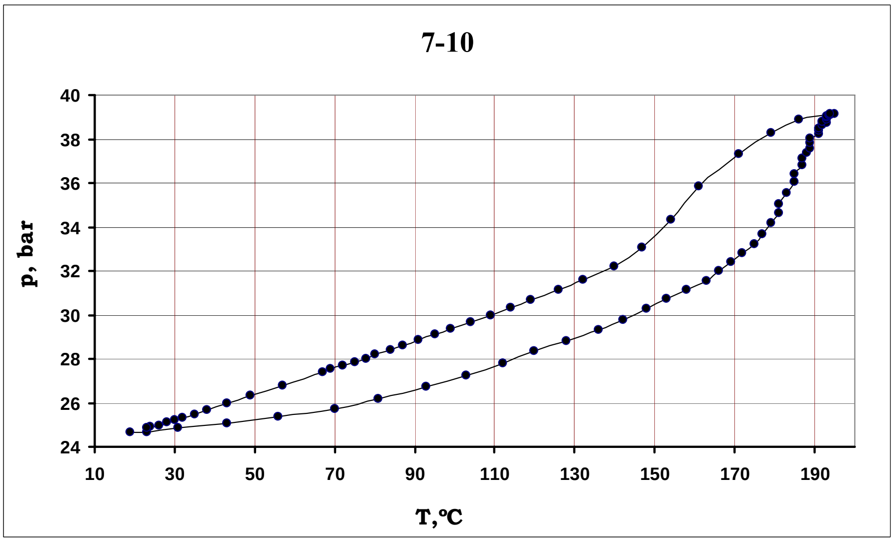

Figure 2.4.7. Volumetric changes depending on temperature and absorption of hydrogen of alloy 7-10

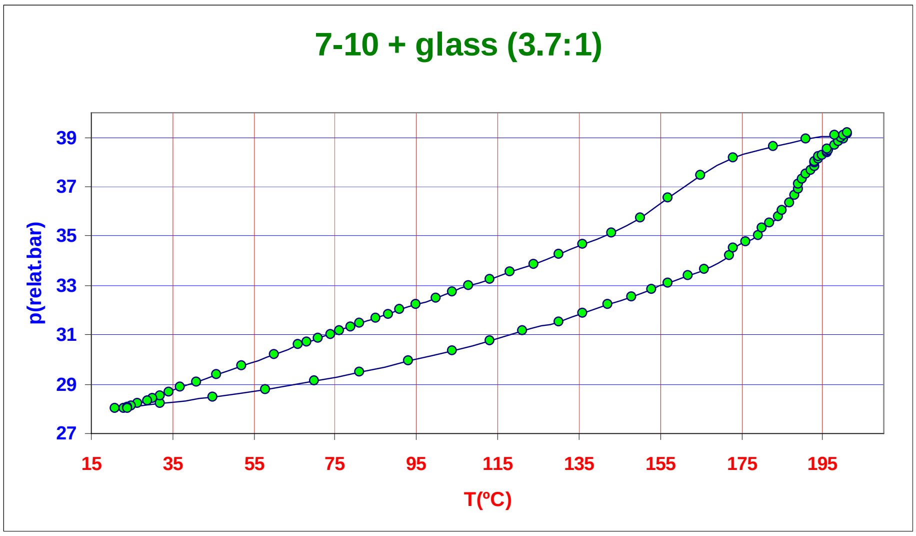

Figure 2.4.8. Volumetric changes depending on temperature and absorption of hydrogen of composite material alloy 7-10+glass

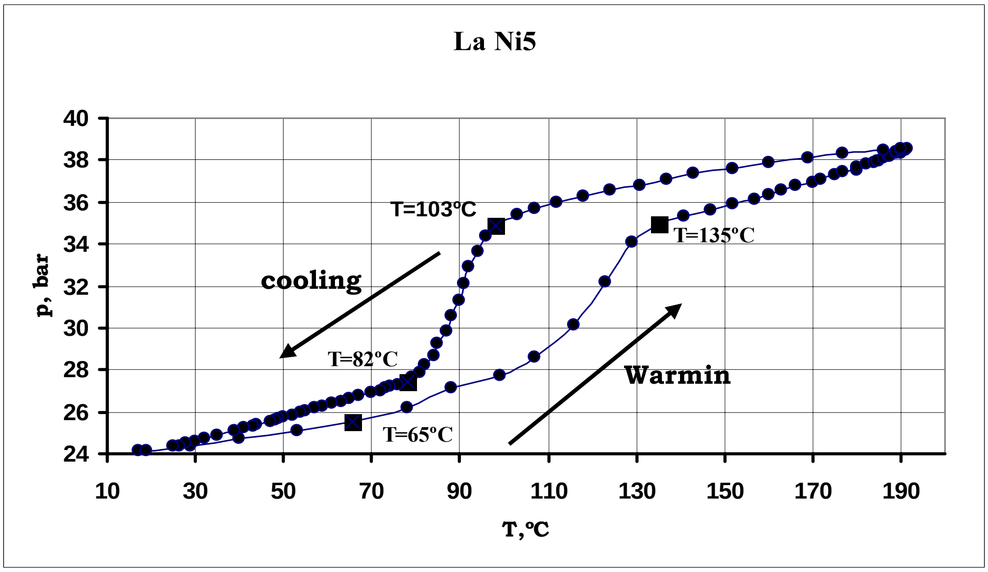

Figure 2.4.9. Volumetric changes depending on temperature and absorption of hydrogen of alloy 7-10

The weight loss in hydrogenated samples was determined by differential thermogravimeter DTG-60. Figures 2.4.10 and 2.4.11 show the analysis of $LaNi_5$ and alloy 7-10. There is defined not only the change of weight in the desorption process but also the temperature change during the dehydrogenation.

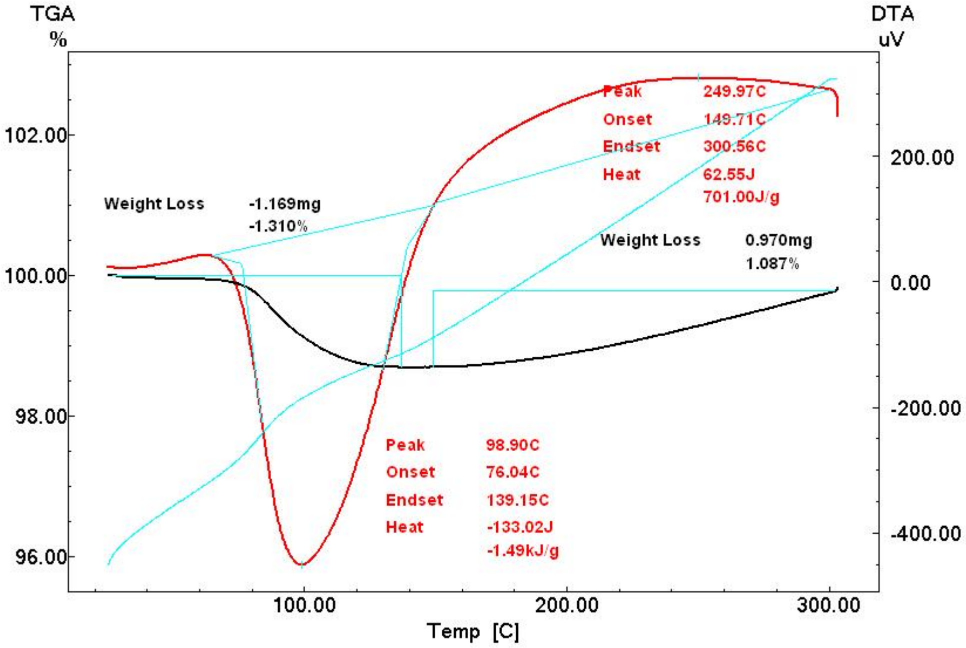

Figure 2.4.10 Desorption characteristics of LaNi5.

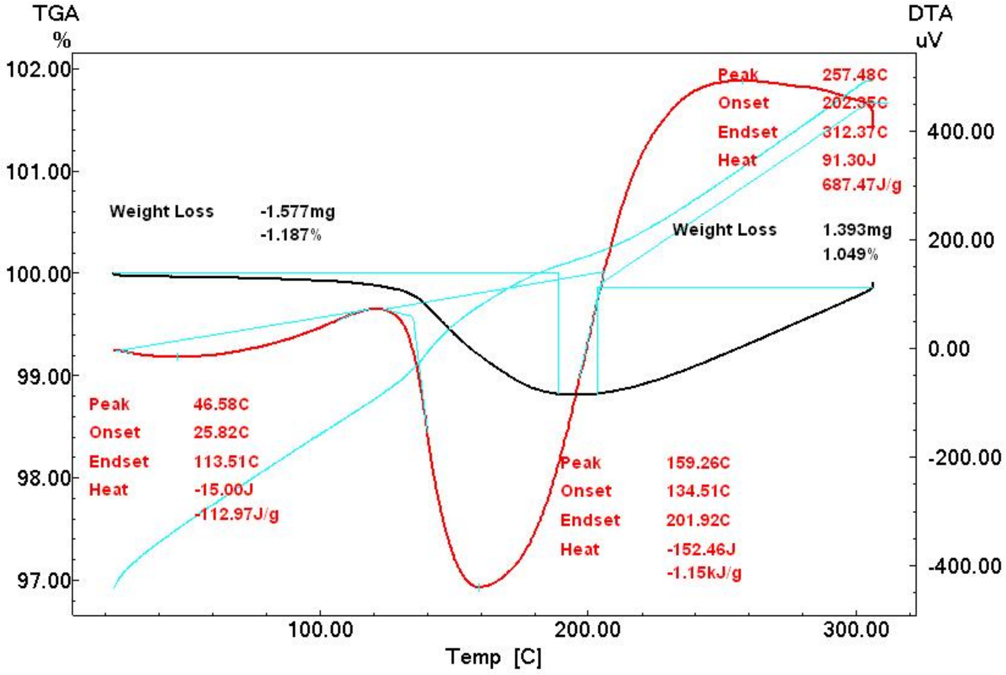

Figure 2.4.11 Desorption characteristics of alloy 7-10.

3. Results

Analyzing treated data it was figured out that raw hydride material 7-10 absorbing more hydrogen than classical $LaNi_5$ by itself. The HPB plots clearly show that pure $LaNi_5$ absorbing and desorbing hydrogen when the pressure is changed (Figure 3.1). There just 0.26 w% of hydrogen is remaining in the pure $LaNi_5$ sample at the one atmosphere.

Though, the data plot of LaMm sample 7-10 displays opposite tendency – the absorbed hydrogen amount just slightly decreasing after lowering the pressure to the one atmosphere (figure 3.2).

That effect could be explained by the substitution of Ni with corresponding B-components: Al, Mn and Co as well as with decreasing of La constituent in the alloy. The Co substitution also results in the increase of cyclic stability of the materials, mainly due to their higher resistance to decrepitation and Mn allows preserve a high hydrogen sorption capacity [100]

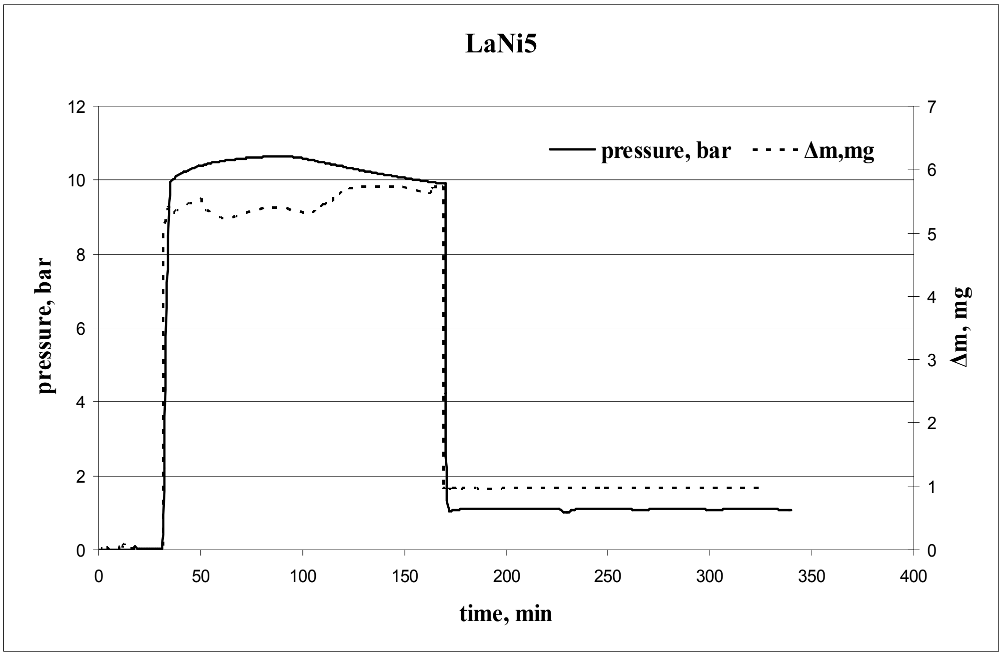

Figure 3.1: HPB data plot of the pure $LaNi_5$ at the room temperature.

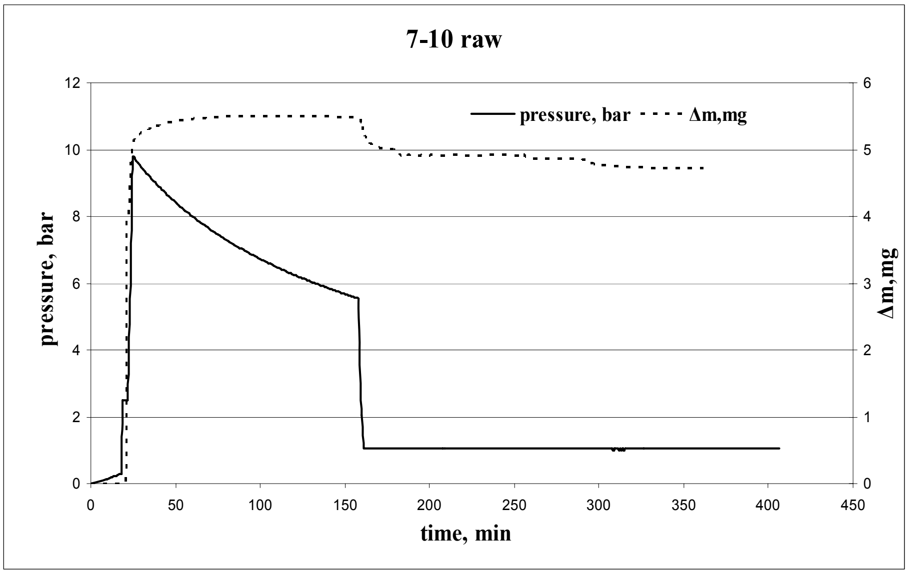

Figure 3.2: HPB data plot of the raw sample 7-10, at the room temperature.

Comparison of HPB plots of both materials with the glass phase additives confirmed the same tendency – sample 7-10 and glass absorbed more hydrogen than $LaNi_5$ with glass (Fig. 3.3 – 3.4).

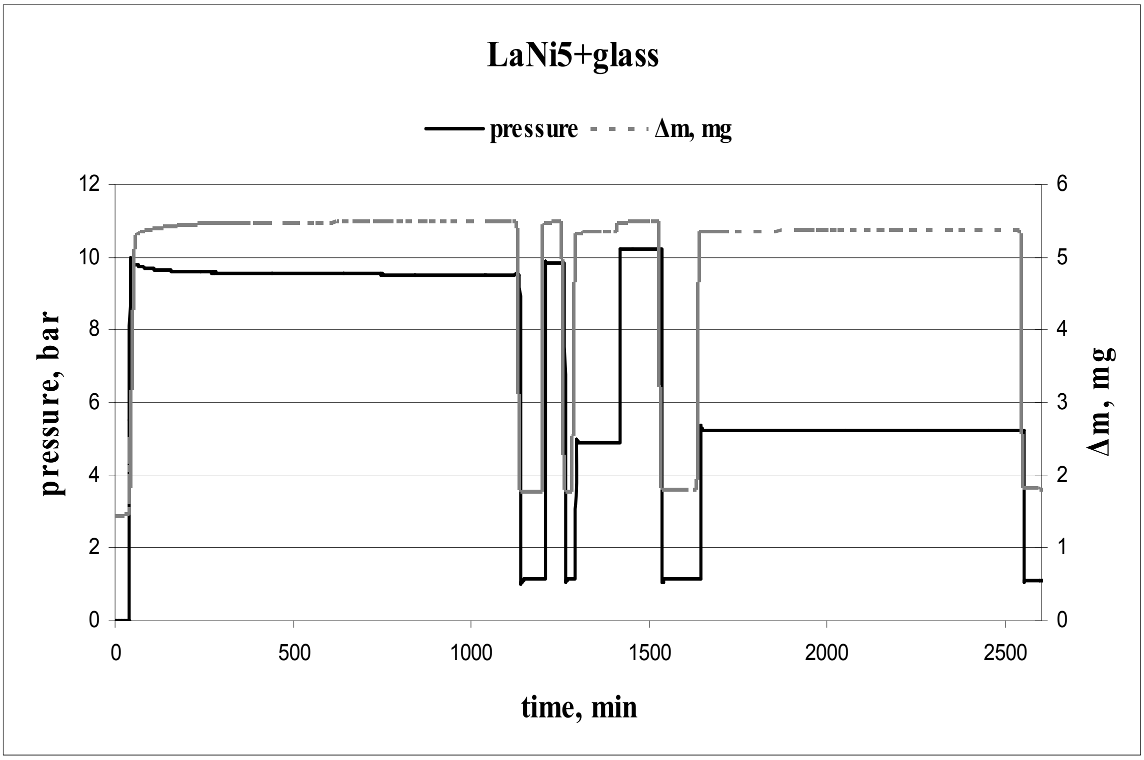

Figure 3.3: HPB plot of $LaNi_5$ with the glass phase after 3 cycles at 10 and 5 bar hydrogen pressure.

Figure 3.3 shows an activation process and three cycles of $LaNi_5$ with addition of 1/3 of the alloy volume % of glass. It is observed that the absorbed amount of hydrogen differs just a little with changing hydrogen pressure from 10 bars to 5 bars. Amount of absorbed and desorbed hydrogen was pretty stable.

A three cycles of composite 7-10 and glass (figure 3.4) was performed with changing the temperature from room temperature to 80°C. The room temperature in the time of these experiments was 33°C what is much higher comparing with previous experiments in the RNL. It could be seen that activation of alloy was done at the 10 bars of hydrogen pressure but in the further experiment time the hydrogen atmosphere was close to 1 bar. The small changes in pressure are caused by desorbed hydrogen. Due to the time consuming process of heating and cooling the system (Fig. 3.5) it is very hard to compare the absorption and desorption rate of $LaNi_5$ and alloy 7-10 because the temperature reaches total equilibrium after ~130 min. Nevertheless it allows comparing this value between raw alloy and composite.

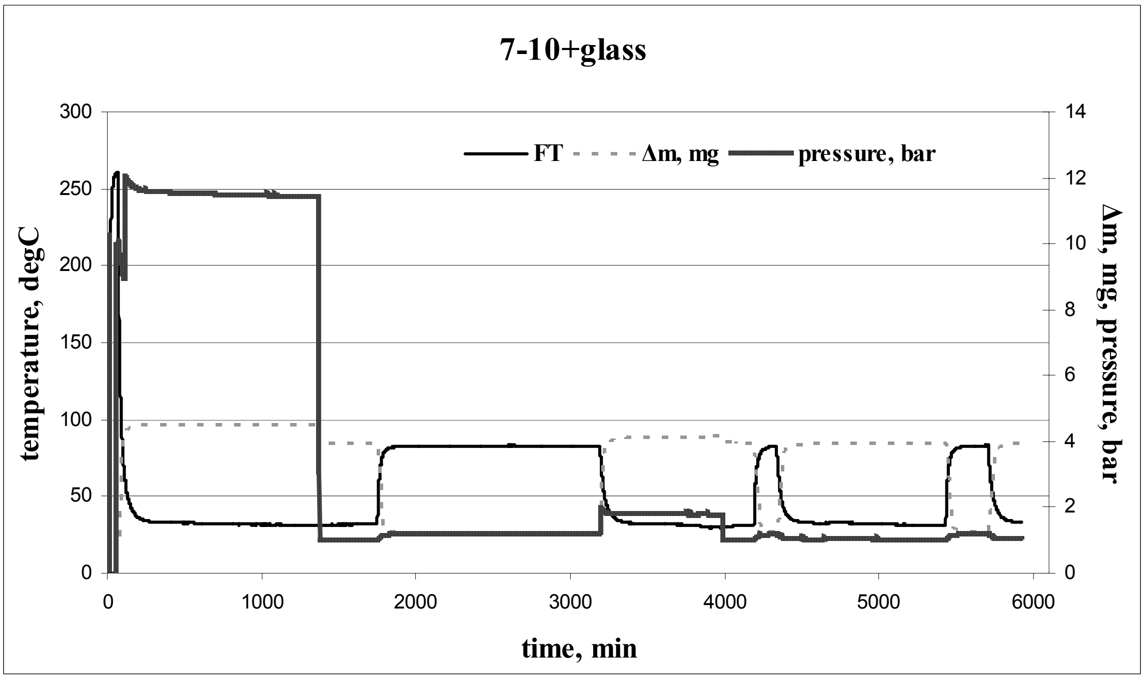

Figure 3.4: HPB plot of alloy 7-10 with the glass phase after 3 cycles at 1 bar hydrogen pressure in temperature range room temperature to + 80°C.

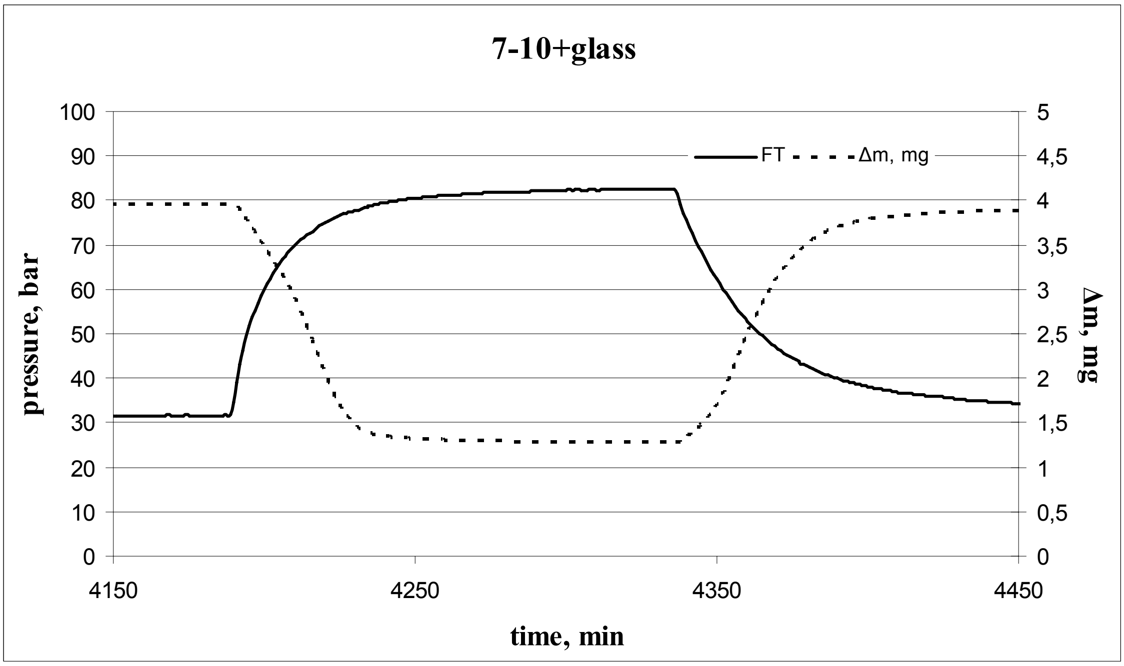

Figure 3.5: Enlarged HPB plot of alloy 7-10 with glass phase. The temperature reaches its stability point after ~150 min.

According to the gained data there is not a great difference in the absorption/desorption rates. It was observed that the absorption was faster for the composite than for the raw alloy 7-10 but vice versa for desorption process, however the difference didn't exceeded 10 min for the desorption and 20 min for the absorption process.

Unexpected result was observed after hydrogenation of the composite – 7-10 with glass (Figure 3.6).

The XRD results showed that the diffraction peaks of hydrogenated alloy 7-10 were largely shifted to the smaller angles than that of the starting alloy, indicating that the α-phase of hydride is changed into the β-phase and the lattice parameters and cell volume of the hydride is larger than that of the starting alloy.

For the composite the observed shift of XRD peaks after hydrogenation was even larger than that for pure 7-10 alloy. Also corresponding lattice parameters and cell volume for hexagonal P6/mmm symmetry was larger of hydrogenated composite sample as for fully hydrogenated alloy 7-10 (Table 3.1.) [124].

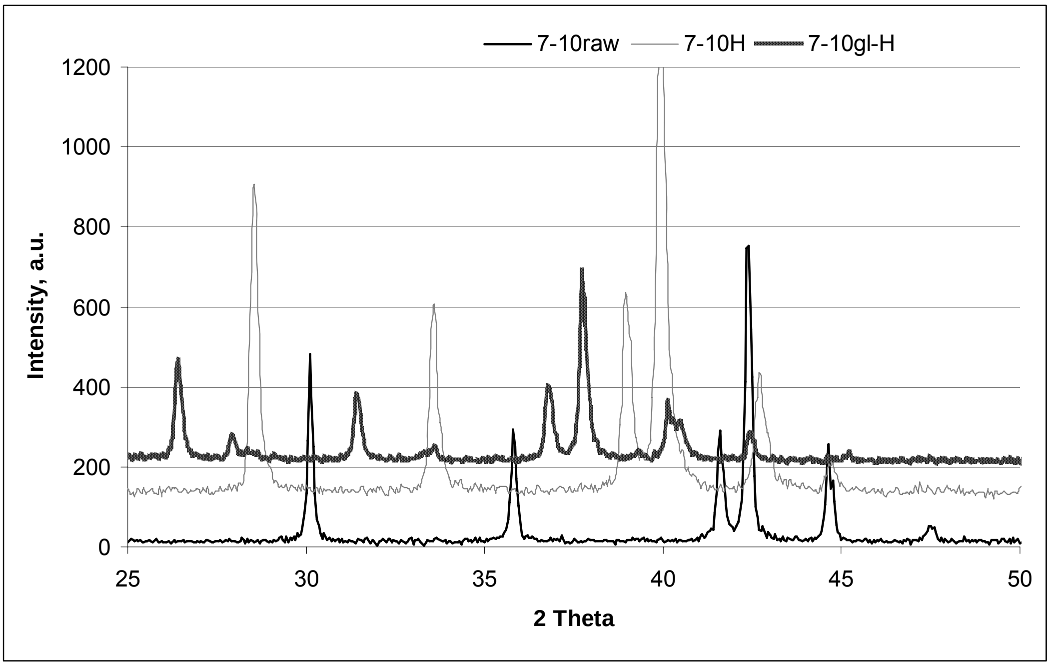

Figure 3.6: XRD plot of raw (7-10raw), hydrogenated pure 7-10 (7-10H) and hydrogenated alloy 7-10 with glass phase (7-10gl-H).

Table 4: Structural parameters of raw and hydrogenated samples

Cell size Sample	a, Å	c, Å	V, Å3
7-10	5,0083	4,0567	88,12
7-10hydrogenated	5,326	4,234	104,0
7-10+glass hydrogenated	5,369	4,2754	106,78

The calculations of absorbed hydrogen for the composite, converting to the hydrogen absorbed in the alloy, shows that it is more than for pure alloy sample 7-10 (Table 5). That could be explained with hydrogen spillover and absorption in alloy-glass mixture.

Table 5: Calculations of HPB data for raw alloy (7-10) and composite (7-10+glass) where the Δm_{total} – total change of weight, Δm_{av} – average change of weight during cycling, $\Delta m(1atm)$ – change of weight if system is at 1 atm.

7-10	Δm, mg	w%	x
Δm_{total}	5,507E-03	1,582	6,966
Δm_{total}	5,138E-03	1,477	6,499
$\Delta m(1atm)$	4,883E-03	1,405	6,177
7-10+glass			
Δm_{total}	5,048E-03	1,643	7,242
Δm_{av}	4,616E-03	1,504	6,621
$\Delta m(1atm)$	4,393E-03	1,433	6,302

During the PhD studies in the Institute of Solid State Physics was constructed autoclave type device that could be used for volumetric investigations of the hydride alloys after the end of the cooperation project with RNL (Figure 3.7). It is equipped with pressure sensors ECO-1 from Greisinger Electronic GmbH and a stainless steal container with an internal volume of 36 cm^3. The changes of pressure during hydrogenation of alloys and composites were observed due to the absorption/adsorption and desorption of hydrogen in the sample. It can be used at constant temperatures and at constant pressure in the container.

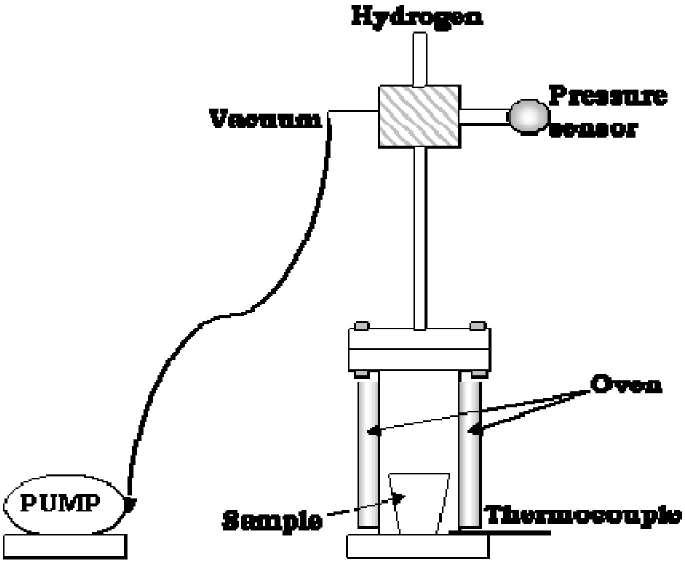

Figure 3.7: Self-made equipment for volumetric investigations.

The first results gained in the new device are shown in figures 3.8-3.9.

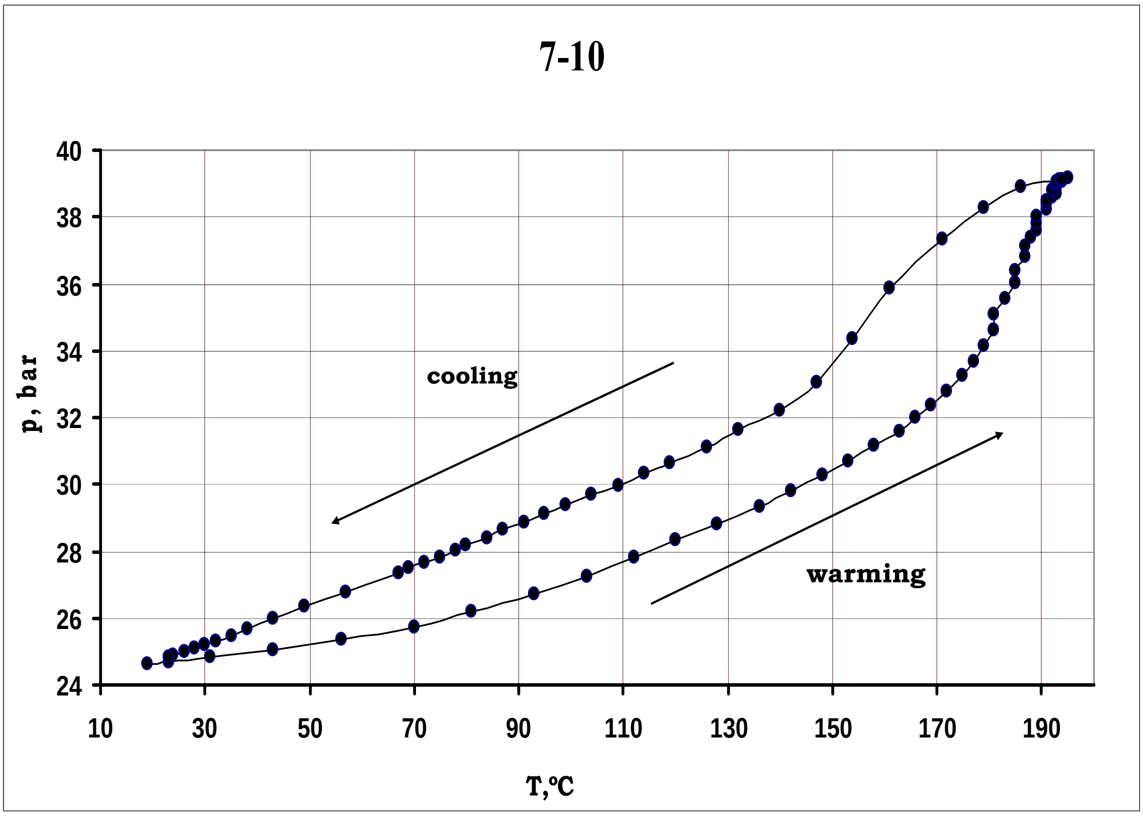

Figure 3.8: Volumetric data for LaMm alloy 7-10

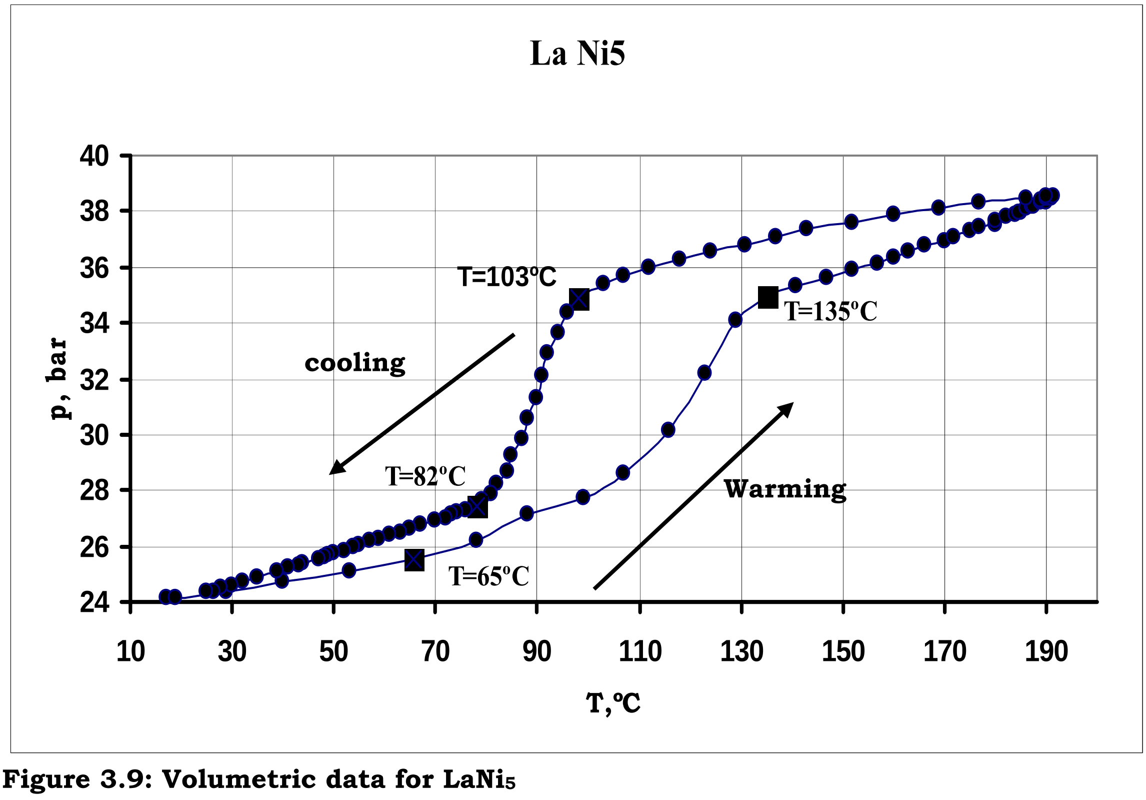

Figure 3.9: Volumetric data for $LaNi_5$

Data gained by volumetric method shows that pressure changes during the hydrogenation of $LaNi_5$ is more noticeable then for pure alloy 7-10. TG analysis for the $LaNi_5$ with glass and for the alloy 7-10 with glass is illustrated in figure 3.10.

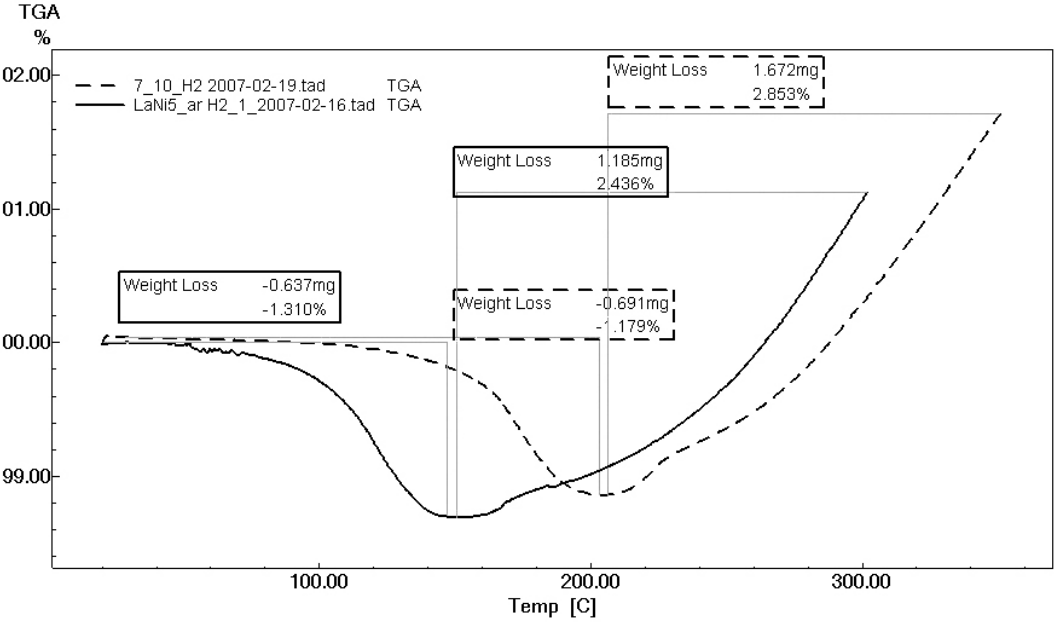

Figure 3.10: TG analysis plot for the $LaNi_5$ with glass phase (interrupted line) and alloy 7-10 with glass phase (solid line).

There is automatically calculated weight loss during the heating of samples that indicates that weight loss for $LaNi_5$ sample is greater that for alloy 7-10 just for 0,13 w%. Impressive increasing of the weight at temperatures more than 180°C could be explained as absorption of the ambient gases, mostly oxidation.

Electrochemical data

The electrochemical properties of different nickel based materials (bulk, porous, foamed tapes) were examined to state the hydrogen adsorption/absorption phenomena and possibility to use them as a negative electrode in hydrogen devices as electrolysers, rechargeable batteries, fuel cells. Surface activation of nickel materials by electroplated palladium, metal hydride alloy and nickel thin films were used to prove the formation of nickel hydride during cathodic charging.

Characteristic hydrogen adsorption/absorption and desorption maxima is observed on palladium electrode at -1,04 V and -0,28 V, respectively. It is less distinctive for nickel substrate (Fig. 3.11) and decreases going from porous and electroplated samples to bulk nickel.

For charge/discharge studies the samples were charged with 1 mA/cm^2 current for 1 minute and discharged with 0,1 mA/cm^2 for 5 minutes.

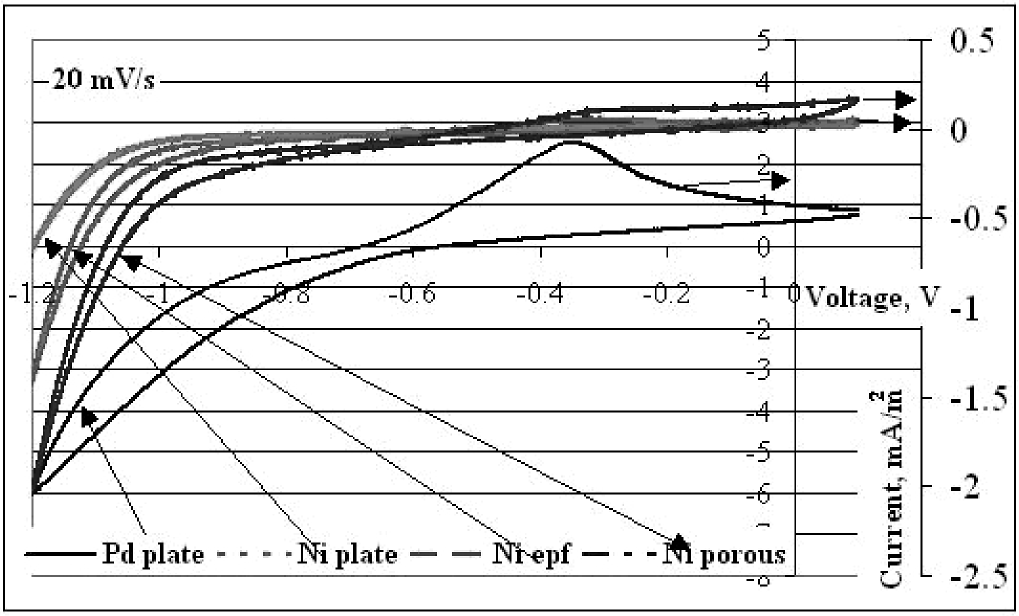

Figure 3.11: Volt-ampere curves of blank Ni and Pd samples. Two different current scales are used to indicate structures of curves from nickel samples.

The discharge curves (Figure 3.12) testify that the amount of accumulated hydrogen is increased about 2-3 times that is much less as in the case of Pd is coating.

The addition of metal hydride powder to nickel during electroplating increased the electrochemical activity of coating and stored charge is also increased (Figure 3.13). The impact of the Ni coating on different nickel substrates is the same – the current values are higher for Ni/Ni samples as compared for both maxima at -1.0 V and at -0.5 V, accordingly.

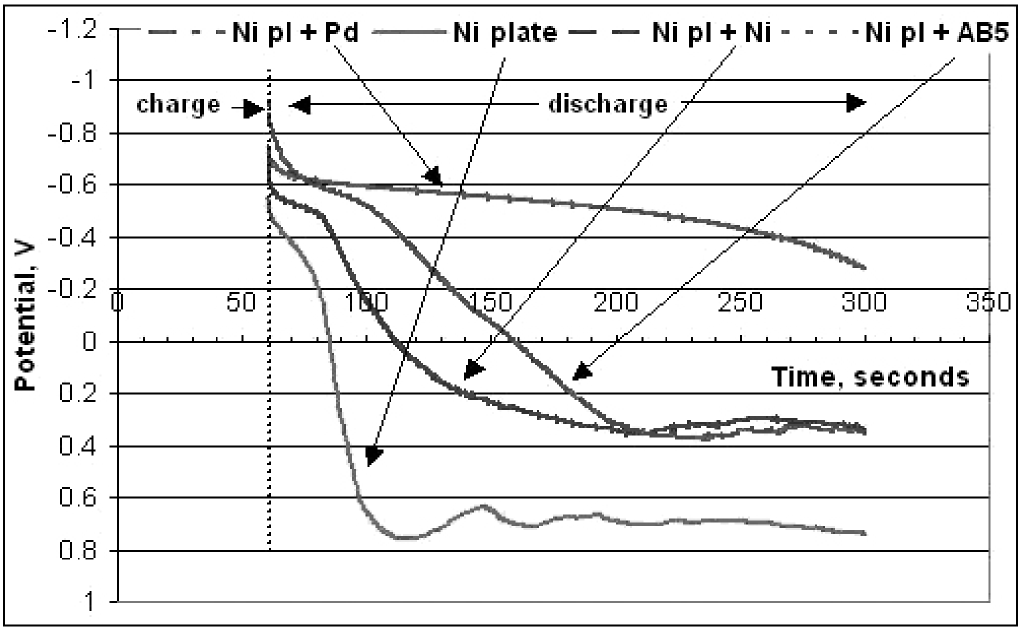

Figure 3.12: Discharge kinetics of Ni plate substrate coated with thin Pd, Ni and composite

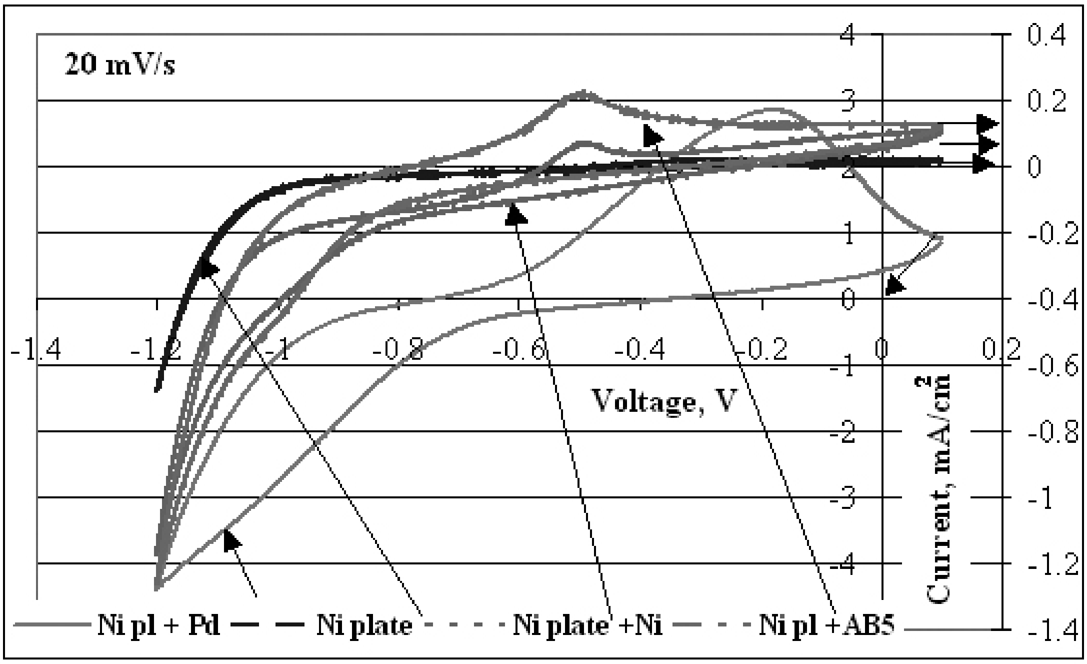

Figure 3.13 Volt-ampere curves of Ni plate substrate coated with thin films of Pd, Ni and composite AB$_5$+Ni film

4. Conclusions

The HPB data treatment and calculations showed that hydrogen uptake in the composite alloy 7-10 with glass exceeds the pure alloy. It could be due to spillover from the AB_5 catalyst. The following mechanism can be deduced: the hydrogen chemisorbs at the surface sites found on the LaMm (mostly Ni sites). Bridges between the catalyst and glass particles allow the chemisorbed hydrogen to migrate onto the glass surface. Desorption occurs directly from the relatively lower energy glass sites without migration back to the catalyst. Hydrogen spillover depends upon the glass-catalyst contact. The contact changes with the quality of the mixing and milling, as well as the position of alloy 7-10 grains in the mixture.

It was observed from the X-ray diffraction patterns, that the beta phase of the ball milled composite sample 7-10+glass occurred faster than in the pure alloy sample and the peak shift to the smaller angles is noticeable larger. Referring to the [99, 125]it is possible to assume, that the gamma hydride phase (γ) is forming, when the alloy 7-10 is mixed in composite with Pyrex glass that isn't observable for pure alloy. In the γ phase the hydrogen atoms prefer the interstitial sites closer to Ni atoms in an elementary cell, producing inhomogeneous distribution and large lattice distortions [99]. Nakamura et al [125] found, that the γ phase contains more hydrogen atoms per unit cell than the β phase.

Results from the TG and volumetric hydrogen uptake measurements in both 7-10 and composite samples showed that for the pure sample it is possible to achieve the maximum predicted amount of absorbed hydrogen, but for the composite sample the necessary activation was not achieved.

Surface activation of nickel materials by electroplated palladium and/or nickel thin films were used to prove the formation of nickel hydride during cathodic charging. Volt-ampere and kinetic measurements showed that not only a palladium, but also the electroplated nickel and the metal hydride alloy additives play an important role in the surface activation of electrode materials and promotion of the hydrogen absorption in the nickel substrate materials. It is proposed that the small nickel clusters in an electroplated nickel film stimulate the enhanced hydrogen absorption in nickel.

The experiments with the metalhydride alloys in the composition with a glass phase will be prolonged in the Institute of Solid State Physics using available DTG-60 and constructed volumetric autoclave devices. The new type of additive for composite as carbon, tungsten oxide or highly porous glass will be considered. The electrochemical experiments will be provided to estimate the new material possible use as an electrode material for hydrogen storage devices.

Surface activation of nickel materials by electroplated palladium and/or nickel thin films were used to prove the formation of nickel hydride during cathodic charging. Volt-amperometric and kinetic measurements showed that not only palladium, but also activated nickel (electroplated) and composite additives (metal hydride alloy) plays important role in the surface activation of electrode materials and promotion of hydrogen absorption in nickel substrate materials. The enhanced hydrogen absorption in nickel is stimulated by small nickel clusters in an electroplated nickel film.

5. Acknowledgements

Author acknowledges the European Union European Social Fund; the Nordic Energy Research Project NORSTORE; the Latvian State Research Program in Material Science VPP-05; Structural Funds of European Community project for financial support

Special thanks to my supervisor Dr. Janis Kleperis, Finn Willy Poulsen, Nikolaos Bonanos, Bjørn Sejr Johansen (RNL); Laimonis Jēkabsons (ISSP UL), Guntars Vaivars, Alexander Nechajev (WCU SA) and Sébastien Huot.

6. References

1. Wunschiers, R. and P. Lindblad, *Hydrogen in education--a biological approach.* International Journal of Hydrogen Energy, 2002. **27**(11-12): p. 1131-1140.
2. *http://dieoff.com/index.html*.
3. *http://www.bp.com/*.
4. *Kyoto Protocol to the UN Framework Convention on Climate Change UNFCCC Third Conference of the Parties.* . 1997(FCCC/CP/1997/L.7/Add.1).
5. Midilli, A., et al., *On hydrogen and hydrogen energy strategies: I: current status and needs.* Renewable and Sustainable Energy Reviews, 2005. **9**(3): p. 255-271.
6. Marban, G. and T. Valdes-Solis, *Towards the hydrogen economy?* International Journal of Hydrogen Energy. **In Press, Corrected Proof**.
7. Ritter, J.A., et al., *Implementing a hydrogen economy.* Materials Today, 2003. **6**(9): p. 18-23.
8. *Renewable energies. Altener Programme Official.* (J L 79).
9. *Renewable energy. White Paper laying down a Community strategy and action plan.* . (COM (97)): p. 599.
10. *Green Paper. Towards a European strategy for the security of energy supply.* 2000: p. 769.
11. *White Paper European transport policy for 2010: time to decide.* 2001(COM 2001): p. 370.
12. *https://www.hfpeurope.org/*.
13. *US DOE. Strategic plan for hydrogen, .* 1998.
14. *US DOE. A national vision of America's transition to a hydrogen economy—to 2030 and beyond.*
15. *http://www.eere.energy.gov/afdc/pdfs/freedomcar_plan.pdf*.
16. *http://www.enaa.or.jp/WE-NET/newinfo/station_taka_e.html*.
17. Drolet, B., et al., *The euro-quebec hydro-hydrogen pilot project [EQHHPP]: demonstration phase.* International Journal of Hydrogen Energy, 1996. **21**(4): p. 305-316.

18. Bahbout, A., G.P. Tartaglia, and U. Bunger, *Hydrogen activities in the European Union work programme.* 21St World Gas Conference, 2000.

19. *European Fuel Cell and Hydrogen Projects 2002-2006, http://ec.europa.eu/research/energy/pdf/hydrogen_synopses_en.pdf.*

20. *http://www.mpr.com/pubs/hydroprod.pdf.*

21. *http://www.iaea.or.at/inis/aws/htgr/fulltext/30027279.05.pdf.*

22. *http://www.getenergysmart.org.*

23. Deutschmann, O. and L.D. Schmidt, *Two-dimensional modeling of partial oxidation of methane on rhodium in a short contact time reactor.* Twenty-Seventh Symposium (International) on Combustion/The Combustion Institute, 1988: p. 2283–2291.

24. *http://www.hyradix.com/index.cfm/AutothermalAdvantages.*

25. *http://www.gasification.org/gasproc.htm.*

26. Babu, S.P., *Biomass gasification for hydrogen production – Process description and research needs.* http://www.ieahia.org.

27. Miller, E. and R. Rocheleau, *Photoelectrochemical production of hydrogen* Proceedings of the 2002 U.S. DOE Hydrogen Program Review NREL/CP-610-32405, 2002.

28. Melis, A. and T. Happe, Plant Physiology, 2001. **127**: p. 740-748.

29. Yıldız, A. and K. Pekmez, eds. *Electrochemical and photoelectrochemical hydrogen production.* NATO ASI Series Hydrogen Energy Systems, Utilization of Hydrogen and Future Aspects, ed. Y. Yürüm. 1995, Kluwer Academic Publishers: London.

30. Imarisio, G., *Progress in water electrolysis at the conclusion of the first hydrogen programme of the European communities.* International Journal of Hydrogen Energy, 1981. **6**(2): p. 153-158.

31. *http://www.humboldt.edu.*

32. Satyapal, S., et al., *The U.S. Department of Energy's National Hydrogen Storage Project: Progress towards meeting hydrogen-powered vehicle requirements.* Catalysis Today, 2007. **120**(3-4): p. 246-256.

33. Grätzel, M., *Photoelectrochemical cells.* NATURE, 2001. **414**(15 NOVEMBER).

34. *High-temperature electrolysis for hydrogen production from nuclear energy.* INL research and development, http://www.inl.gov/.

35. Brown, L.C. and e. al, *Alternative Flowsheets for the Sulfur-Iodine Thermochemical Hydrogen Cycle.* GA-A24266, 2003.

36. *Technical plan-hydrogen production.* http://www1.eere.energy.gov.

37. Züttel, A., *Hydrogen storage methods.* Naturwissenschaften, 2004. **V91**(4): p. 157-172.

38. Blackman, J.M., *High pressure hydrogen storage on carbon materials for mobile applications.* Thesis, University of Nottingham, 2005.

39. *http://en.wikipedia.org/*.

40. *http://www.gm.com/*.

41. Bossel, U., *Energy and the hydrogen economy.* 2003.

42. *http://www.quantumcomposites.com/*.

43. Sherif, S.A., N. Zeytinoglu, and T.N. Veziroglu, *Liquid hydrogen: Potential, problems, and a proposed research program.* International Journal of Hydrogen Energy, 1997. **22**(7): p. 683-688.

44. *http://www.hydrogen.org/index-e.html*.

45. Sandrock, G., *A panoramic overview of hydrogen storage alloys from a gas reaction point of view.* Journal of Alloys and Compounds, 1999. **293-295**: p. 877-888.

46. Zuttel, A., *Materials for hydrogen storage.* Materials Today, 2003. **6**(9): p. 24-33.

47. L.Schlapbach, ed. *Surface properties and activation.* Hydrogen in intermetallic compounds II, ed. L. Schlapbach. Vol. Topics in applied physics 67. 1992, Springer: Berlin Heidelberg New York. 15-95.

48. Schlapbach, L., ed. *Introduction.* Hydrogen in Intermetallic Compounds I, ed. L.Schlapbach. Vol. 63. 1988, Springer-Verlag: Germany. 350.

49. Schlapbach, L., ed. *Surface properties and activation.* Hydrogen in intermetallic compounds II, ed. L. Schlapbach. Vol. Topics in applied physics 67. 1992, Springer: Berlin Heidelberg New York. 328.

50. Kleperis, J., et al., *Electrochemical behavior of metal hydrides.* Journal of Solid State Electrochemistry, 2001. **5**(4): p. 229-249.

51. Lindholm, I., *Allmanna Svenska Elektriska Aktiebolaget (SE) Patent US-3,262,816* 1966.

52. Dilworth, L.R. and W.J. Wunderlin, *Allis-Chalmers manufacturing Company (US) Patent US- 3,405,008.* 1968.

53. Dilworth, L.R., *Allis-Chalmers Manufacturing Company (US) Patent US-3,405,009.* 1968.

54. Sakai, T., et al. in *Proc. Symp. on Hydrogen Storage Materials, Batteries and Electrochemistry.* 1992: Pennington, NJ.

55. Bernd, F., *Product information from Gesellschaft für Elektrometallurgie MBH (GfE).* 1992.

56. Percheron-Guegan, A. and J.-M. Welter, eds. *Preparation of intermetallics and hydrides.* Hydrogen in Intermetallic Compounds I, Topics in Applied Physics, ed. L. Schlapbach. Vol. 63. 1988, Springer Verlag: Berlin-Heidelberg. 11-48.

57. Thona, D. and J. Perepezko, *A geometric analysis of solubility ranges in Laves phases.* Journal of Alloys and Compounds, 1995. **224**: p. 330.

58. Fetcenko, M.A., S.Venkatesan, and S.R. Ovshinsky. *Selection of metal hydride alloys for electrochemical applications.* in *Symp. on Hydrogen Storage Materials, Batteries and Electrochemistry.* 1992: Pennington, NJ.

59. Zoitos, B.K., et al. *Characterization of activated metal hydride alloy.* in *Symp. on Hydrogen Storage Materials, Batteries and Electrochemistry.* 1992: The Electrochemical Society Inc.

60. Sakintuna, B., et al., *Metal hydride materials for solid hydrogen storage: A review.* International Journal of Hydrogen Energy. **In Press, Corrected Proof**.

61. Dornheim, M., et al., *Hydrogen storage in magnesium-based hydrides and hydride composites.* Scripta Materialia, 2007. **56**(10): p. 841-846.

62. Higuchi, K., et al., *Remarkable hydrogen storage properties in three-layered Pd/Mg/Pd thin films.* Journal of Alloys and Compounds, 2002. **330-332**: p. 526-530.

63. Gingl, F., L. Gelato, and K. Yvon, *The hydride fluoride crystal structure database, HFD.* Journal of Alloys and Compounds, 1997. **253-254**: p. 286-290.

64. Yvon, K. and B. Bertheville, *Magnesium based ternary metal hydrides containing alkali and alkaline-earth elements.* Journal of Alloys and Compounds, 2006. **425**(1-2): p. 101-108.

65. Varin, R.A., et al., *The effect of sequential and continuous high-energy impact mode on the mechano-chemical synthesis of nanostructured complex hydride Mg2FeH6.* Journal of Alloys and Compounds, 2005. **390**(1-2): p. 282-296.

66. Stier, W., et al., *Hydrogen storage in magnesium based alloys.* Am. Chem. Soc, Div. Fuel Chem, 2005. **50**(1).

67. Bogdanovic, B., et al., *Metal-doped sodium aluminium hydrides as potential new hydrogen storage materials.* Journal of Alloys and Compounds, 2000. **302**(1-2): p. 36-58.

68. Teitel, J., *Microcavity Hydrogen Storage.* Final Progress Report prepared for U.S. Dept. of Energy and Environment under Contract No. DE-AC02-76CH00016, 1981.

69. Yan, K.L., et al., *Storage of hydrogen by high pressure microencapsulation in glass.* International Journal of Hydrogen Energy, 1985. **10**(7-8): p. 517-522.

70. Eklund, G. and O. Von Krusenstierna, *Storage and transportation of merchant hydrogen.* International Journal of Hydrogen Energy, 1983. **8**(6): p. 463-470.

71. Duret, B. and A. Saudin, *Microspheres for on-board hydrogen storage.* International Journal of Hydrogen Energy, 1994. **19**(9): p. 757-764.

72. Tzimas, E., et al., *Hydrogen Storage: State - Of - The - Art and Future Perspective.* European Commission - Directorate General Joint Research Centre (DG JRC) -Institute for Energy, Petten,The Netherlands, 2003.

73. Lee, S.M., et al., *Hydrogen adsorption and storage in carbon nanotubes.* Synthetic Metals, 2000. **113**(3): p. 209-216.

74. Lee, S.M. and Y.H. Lee, *Hydrogen storage in single-walled carbon nanotubes.* Applied Physics Letters, 2000. **76**(20): p. 2877-2879

75. Cheng, H.-M., Q.-H. Yang, and C. Liu, *Hydrogen storage in carbon nanotubes.* Carbon, 2001. **39**(10): p. 1447-1454.

76. Panella, B., M. Hirscher, and S. Roth, *Hydrogen adsorption in different carbon nanostructures.* Carbon, 2005. **43**(10): p. 2209-2214.

77. Withers, J.C., R.O. Loutfy, and T.P. Lowe, *Fullerene Commercial Vision.* 1997, Taylor & Francis. p. 1 - 31.

78. Peera, A.A., L.B. Alemany, and W.E. Billups, *Hydrogen storage in hydrofullerides.* Applied Physics A: Materials Science & Processing, 2004. **78**(7): p. 995-1000.

79. Loutfy, R.O. and E.M. Wexler, *Feasibility of fullerene hydride as a high capacity hydrogen storage material.* Proceedings of the 2001 DOE Hydrogen Program Review NREL/CP-570-30535.

80. Gutowska, A., et al., *Nanoscaffold Mediates Hydrogen Release and the Reactivity of Ammonia Borane.* 2005. p. 3578-3582.

81. Rowsell, J.L.C. and O.M. Yaghi, *Strategies for Hydrogen Storage in Metal-Organic Frameworks.* 2005. p. 4670-4679.

82. Dmitriev, R.V., et al., *Mechanism of hydrogen spillover and its role in deuterium exchange on PtY zeolite.* Journal of Catalysis, 1980. **65**(1): p. 105-109.

83. Weitkamp, J., M. Fritz, and S. Ernst, *Zeolites as media for hydrogen storage.* International Journal of Hydrogen Energy, 1995. **20**(12): p. 967-970.

84. *http://www.rsc.org/Publishing/Journals/CP/News/2006/arean.asp.*

85. Falconer, J.L. and W.C. Conner, *Second international confernce on spillover : Leipzig, G.D.R., June 13-15, 1989.* Applied Catalysis, 1989. **56**(2): p. N28-N29.

86. Conner, W.C. and J.L. Falconer, *Spillover in Heterogeneous Catalysis.* Chemical Review, 1995. **95**(3): p. 759-788.

87. Levy, R.B. and M. Boudart, *The kinetics and mechanism of spillover.* Journal of Catalysis, 1974. **32**(2): p. 304-314.

88. Keren, E. and A. Soffer, *Simultaneous electronic and ionic surface conduction of catalyst supports: A general mechanism for spillover : The role of water in the Pd-catalyzed hydrogenation of a carbon surface.* Journal of Catalysis, 1977. **50**(1): p. 43-55.

89. Fleisch, T. and R. Abermann, *On the reduction of Ag2S films by hydrogen spillover under ultra high vacuum conditions.* Journal of Catalysis, 1977. **50**(2): p. 268-278.

90. Lenz, D.H., W.C. Conner, and J.P. Fraissard, *Hydrogen spillover on silica : III. Detection of spillover by proton NMR.* Journal of Catalysis, 1989. **117**(1): p. 281-289.

91. Candau, J.F.C. and W.C. Conner, *The spillover of hydrogen onto silica : IV. The use of scanning FTIR to follow spillover from a point source.* Journal of Catalysis, 1987. **106**(2): p. 378-385.

92. Lachawiec, A.J., G. Qi, and R.T. Yang, *Hydrogen Storage in Nanostructured Carbons by Spillover: Bridge-Building Enhancement.* Langmuir, 2005. **21**(24): p. 11418-11424.

93. Li, Y. and R.T. Yang, *Significantly Enhanced Hydrogen Storage in Metal-Organic Frameworks via Spillover.* Journal of the American Chemical Society, 2006. **128**(3): p. 726-727.

94. Sermon, P.A. and G.C. Bond, *Hydrogen Spillover.* Catalysis Reviews, 1974. **8**(1): p. 211.

95. Ares, J.R., F. Cuevas, and A. Percheron-Guégan, J. Mat. Sc. And Eng., B, 2004. **108**: p. 76.

96. Kleperis, J. and A. Lusis, *Hydrogen transfer problems at metal/proton electrolyte interfaces.* Z. fur Physik. Chemie, 1993). **181**: p. 321-328.

97. Zaluski, L., A. Zaluska, and J.O. Strom-Olsen, J. Alloys and Comp., 1997. **253**: p. 70.

98. http://www.retsch.com.

99. Huot, J., et al., *Structural study and hydrogen sorption kinetics of ball-milled magnesium hydride.* Journal of Alloys and Compounds, 1999. **293-295**: p. 495-500.

100. Zaluska, A., L. Zaluski, and J.O. Ström-Olsen, *Structure, catalysis and atomic reactions on the nano-scale: a systematic approach to metal*

hydrides for hydrogen storage. Applied Physics A: Materials Science & Processing, 2001. **72**(2): p. 157-165.

101. Hong, T.-W., S.-K. Kim, and Y.-J. Kim, *Dehydrogenation properties of nano-/amorphous Mg2NiHx by hydrogen induced mechanical alloying.* Journal of Alloys and Compounds, 2000. **312**(1-2): p. 60-67.
102. Ciszewski, A., et al., *Effects of saccharin and quaternary ammonium chlorides on the electrodeposition of nickel from a Watts-type electrolyte.* Surface and Coatings Technology, 2004. **183**(2-3): p. 127-133.
103. Mallory, G.O. and J.B. Hajd, *Electroless Plating: Fundamentals and Applications*. 1990, Orlando, FL: American Electroplaters and Surface Finishers Society.
104. Kleperis, J., et al., *Electrochemical investigation of hydrogen evolution and absorption phenomena in Nickel based electrodes*, in *New Promising Electrochemical Systems for Rechargeable Batteries*, V. Barsukov and F. Beck, Editors. 1996, Kluwer Academic Publishers: Netherlands. p. 285-302.
105. Schlapbach, L. and A. Zuttel, *Hydrogen-storage materials for mobile applications.* Nature, 2001. **414**(6861): p. 353-358.
106. John, G., *Book review: Introduction to X-Ray Powder Diffractometry. RON JENKINS and ROBERT L. SNYDER Volume 138 in <I>Chemical Analysis</I>, J. D. Winefordner, Series Editor. Wiley, New York, 1996, pp. 403+xxiii, £65, ISBN 0471513393*. 1997. p. 245.
107. http://www.eserc.stonybrook.edu/ProjectJava/Bragg/.
108. Hou, Q.-F., et al., *The surface fractal investigation on carbon nanotubes modified by the adsorption of poly(acrylic acid).* Surface and Coatings Technology, 2005. **190**(2-3): p. 394-399.
109. Cottis, R. and S. Turgoose. *Electrochemical Impedance and Noise*. in *NACE International*. Houston, TX.
110. Bard, A.J. and L.R. Faulkner, *Electrochemical Methods; Fundamentals and Applications*. 1980: Wiley Interscience publications.
111. Geenen, F., *Characterization of Organic Coatings with Impedance Measurements; A Study of Coating Structure, Adhesion and Underfilm Corrosion*. 1990, TU-Delft.

112. Atkins, P.W., *Physical Chemistry*. 1990: Oxford University Press.

113. Oppenheim, A.V. and A.S. Willsky, *Signals and Systems*. 1983: Prentice-Hall.

114. Yeager, E., et al., *Electrodics: Experimental Techniques*, in *Comprehensive Treatise of Electrochemistry*, M. Sluyters-Rehbach and J.H. Sluyters, Editors. 1984, Plenum Press.

115. Macdonald, J.R., *Impedance Spectroscopy; Emphasizing Solid Materials and Systems*. 1987: Wiley Interscience publications.

116. Gabrielle, C., *Identification of Electrochemical Processes by Frequency Response Analysis*. 1980: Solartron Instrumentation Group.

117. Mansfeld, F., *Electrochemical Impedance Spectroscopy (EIS) as a New Tool for Investigation Methods of Corrosion Protection.* Electrochimica Acta, 1990. **35**(10): p. 1533-1544.

118. Scully, J.R., D.C. Silverman, and M.W. Kendig, *Electrochemical Impedance: Analysis and Interpretation.* 1993: ASTM.

119. Walter, G.W., *A Review of Impedance Plot Methods Used for Corrosion Performance Analysis of Painted Metals.* Corrosion Science, 1986. **26**(9): p. 681-703.

120. Kendig, M. and J. Scully, *Basic Aspects of Electrochemical Impedance Application for the Life Prediction of Organic Coatings on Metals.* Corrosion, 1990(1): p. 22.

121. Dobbelaar, J.A.L., *The Use of Impedance Measurements in Corrosion Research; The Corrosion Behavior of Chromium and Iron Chromium Alloys*. 1990, TU-Delft.

122. Earles, C., *Fundamental Experiments of solid electrode electrochemistry*: Updated by Jeremy Lessmann.

123. Kittel, C., *Introduction to Solid State Physics*. 1976, Canada: John Willey and Sons.

124. Kleperis, J., et al., *Hydrogen absorption and adsorption characteristics in materials.* Latvian Journal of Physics and Technical Sciences,, 2006(4): p. 39-46.

125. Nakamura, Y., T. Nomiyama, and E. Akiba, *Phase transformation in La(CoxNi5-x)-H systems (x = 2, 3, 5) studied by in situ X-ray diffraction.* Journal of Alloys and Compounds, 2006. **413**(1-2): p. 54-62.

7. Supplement

7.1. List of publications

1. L.Grinberga, J.Kleperis, Toward Hydrogen Energy in Latvia, Riga Technical University Scientific Proceedings, Series 4, 12 (2004) 50-56
2. L.Grinberga, J.Kleperis, The perspectives of Hydrogen energy in Latvia, International conference “Energetics and Environment in Baltics” scientific proceedings, (2005) 21-32
3. L.Grinberga, J.Kleperis, Metal alloys and composites for hydrogen storage: problems and solutions, Scientific proceedings of the 1st Latvian conference on Nanomaterials and Nanotechnologies (2005) 14-19
4. J.Kleperis, L.Grinberga, G.Vaivars, J.Klavins Hydrogen absorption and adsorption characteristics in materials, Latvian Journal of Physics and Technical Sciences, 4 (2006) 39-46
5. J.Kleperis, L.Grinberga, G.Vaivars, J.Klavins Enhancement of hydrogen storage in composite materials by nanostructuring, International Scientific Journal For Alternative Energy and Ecology, 12 (2006) 20-24
6. J.Kleperis, L.Grinberga, G.Vaivars, J.Klavins, Hydrogen storage in materials-dependence from particle composition and dimensions, Riga Technical University Scientific Proceedings, Series 4, 17, (2006) 205-211
7. L.Grinberga, J.Kleperis, Hydrogen absorbing materials in the laboratory work for students, in „The anthology of documents and materials of ‘High-techs, hydrogen energetics and platinum materials’”, MIREA (2006), 60-71
8. L.Grinberga, J.Kleperis, A.Nechajev, G.Vaivars, F.W.Poulsen, A.S.Pedersen Investigations of the Influence of Different Additives to the Lanthanum Rich Mischmetal, “NATO Security through Science Series A: Chemistry and Biology”, ‘Hydrogen Materials Science and Chemistry of Carbon, SPRINGER (2007) 279-286

9. Ndungu P., Onyegubule N., Necajevs A., Linkovs V., Grinberga L., A simple route for synthesis of carbon nanotubes using LPG as carbon source, Latvian Journal of Physics and Technical Sciences, 1 (2007) 3-9

7.2. List of conference abstracts

1. L.Grīnberga, J.Kleperis, Materiālu struktūras ietekme uz ūdeņraža izdalīšanos dažādu metālu elektrodiem, 20th Scientific conference of Institute of Solid State Physics (ISSP), Riga, Latvia, February16-18, 2004
2. L.Grinberga, Preliminary Results on New Composite Materials for Hydrogen Evolution/Storage, NORSTORE conference/workshop, Stavern, Norway, June 3-6, 2004, http://www.norstore.ife.no
3. L.Grinberga, J. Kleperis, Advanced media for hydrogen storage, International conference „Metal-Hydrogen Systems", Krakow, Poland, September 6-9, 2004
4. J.Kleperis, L.Grinberga, G.Vaivars Hydrogen evolution and absorption researches in Latvia, JRC-IE workshop „Mapping European knowledge on Hydrogen Storage, Petten, The Netherlands, October 28– 29, 2004, http://www.jrc.nl/
5. L.Grīnberga, J. Kleperis, Ūdeņraža Absorbcijas un Desorbcijas Pētījumi Metālhidrīdos, 21st Scientific conference of ISSP, Riga, Latvia, February 7-9, 2005
6. L.Grinberga, J. Kleperis, Metal alloys and composites for hydrogen storage: problems and solutions, 1st Latvian conference on Nanomaterials and Nanotechnologies, Riga, Latvia, March 30-31, 2005
7. L.Grinberga, J. Kleperis, L. Ribickis, Why the hydrogen energy is necessary for Latvia, International conference EcoBalt'2005, Riga, Latvia, May 26-27, 2005
8. L.Grinberga, Electrochemical and physical properties of LaMm and LaMm composites, NORSTORE conference/workshop, Hveragerði, Iceland, June 1-3, 2005, http://www.norstore.ife.no

9. J.Kleperis, L.Grinberga, G.Vaivars, Researches of electrodes for hydrogen evolution/absorption, Theodor Grotthus electrochemistry conference, Vilnius, Lithuania, June 5-8, 2005
10. L.Grinberga, J.Kleperis, A.S. Pedersen, F.W. Puolsen, Investigations of the Influence of Different Additives to the Lanthanum Rich Mischmetal, IX International conference "Hydrogen materials science & Chemistry of Carbon nanomaterials", Sevastopol, Ukraine, September 5-11, 2005
11. L.Grinberga, J.Kleperis, A.S. Pedersen, F.W. Puolsen, Investigations of the Influence of Glass Phase to the Lanthanum Rich Mischmetal, 3rd annual conference/workshop „Copenhagen Graduate School for Nanoscience and Nanotechnology", RISØ, Denmark, December 8, 2005, http://www.cont.dk/
12. L.Grinberga, J.Kleperis, G.Vaivars, J.Klavins, Hydrogen sorption and sorbtion characteristics in materials, 2nd Latvia's conference „Functional materials and nanotechnologies", Riga, Latvia, March 27-28, 2006
13. P. Ndungu, N. Onyegubule, A. Nechaev, V. Linkov, L.Grinberga, A Simple Route For The Synthesis Of Carbon Nanotubes Using Lpg As A Carbon Source, 2nd Latvia's conference „Functional materials and nanotechnologies", Riga, Latvia, March 27-28, 2006
14. X. Wang, S.Naidoo, G. Vaivars, L.Grinberga, V. Linkov, Optimization Of The Synthesis Of Pt-Ru/C Fuel Cell Anode Catalyst, 2nd Latvia's conference „Functional materials and nanotechnologies", Riga, Latvia, March 27-28, 2006
15. L.Grīnberga, J.Kleperis Lantāna Mišmetāla Termogravimetrisko Īpašību Izmaiņas Atkarība no Stikla Fāzes, 22nd Scientific conference of ISSP, Riga, Latvia, March 29-30, 2006
16. L.Grinberga, Studies of Sorption Properties of Metal Hydride Electrodes, NORSTORE conference/workshop Jyllinge, Denmark, May 29-31, 2006, http://www.norstore.ife.no/
17. L.Grinberga, J. Hodakovska, J. Kleperis, G. Vaivars, J. Klavins, Electrochemical hydrogen – storage and usage aspects, VIII Meeting

"Fundamental problems of Solid State Ionics", Chernogolovka, Russia, June 13-16, 2006

18. J.Kleperis, L.Grinberga, G.Vaivars, J.Klavins, Enhancement of hydrogen storage in composite materials by nanostructuring, First World Congress "Alternative Energy and Ecology" WACEE-2006, abstract in "International Scientific Journal for Alternative Energy and Ecology" 5, (37), on river Volga, August 21-25, 2006
19. L.Grīnberga, J. Kleperis, Absorbētā ūdeņraža daudzums materiālā atkarībā no daļiņu izmēra un vides, 23rd Scientific conference of ISSP, Riga, Latvia, February 13-15, 2007
20. J.Hodakovska, L.Grīnberga, J.Kleperis, Elektrodi degvielas šūnām – iespējas un rezultāti, 23rd Scientific conference of ISSP, Riga, Latvia, February 13-15, 2007
21. J. Kleperis, L. Grinberga, M. Ergle, G. Chikvaidze, Thermogravimetric research of hydrogen storage materials, International Baltic Sea region conference Functional materials and nanotechnologies, April 2-4, 2007
22. L. Grinberga, J. Kleperis, Development of new composite materials for hydrogen storage, International Baltic Sea region conference Functional materials and nanotechnologies, April 2-4, 2007